
ADVANCED POLYMERIC MATERIALS FOR TENDON REPAIR

Renjie Liu

07/09/2018

Submitted in partial fulfillment of the requirements of
the

Degree of Doctor of Philosophy



SUPERVISORS:

DR. C.REMZI BECER


PROF. HAZEL R.C SCREEN

Statement of Originality

I, Renjie Liu, confirm that the research included within this thesis is my own work or that where it has been carried out in collaboration with, or supported by others, that this is duly acknowledged below and my contribution indicated. Previously published material is also acknowledged below. I attest that I have exercised reasonable care to ensure that the work is original, and does not to the best of my knowledge break any UK law, infringe any third party's copyright or other Intellectual Property Right, or contain any confidential material. I accept that the College has the right to use plagiarism detection software to check the electronic version of the thesis.

I confirm that this thesis has not been previously submitted for the award of a degree by this or any other university. The copyright of this thesis rests with the author and no quotation from it or information derived from it may be published without the prior written consent of the author.

Signature:

Handwritten signature in Chinese characters: 刘仁杰 (Liu Renjie)

Date: 07/09/2018

Details of collaboration and publications:

Parts of this thesis have been published in:

Liu R, Patel D, Screen H R C, Becer CR. *Bioconjugate Chem.*, 2017, 28(7): 1955-1964.

Liu R, Becer C R, Screen H R C. *Macromolecular bioscience*, 2018, 1800293.

Acknowledgments

It's really an honor to express my appreciation to the people who helped me so much during my PhD study.

Firstly, I would like to say a big thank you to both of my supervisors: Dr. Remzi Becer and Professor Hazel Screen. Without their guidance and patience, none of these can ever happen. Words can not describe how lucky it is that I have had the chance to work in both groups and met so many great scientists. You really showed me the road to a good scientist.

Secondly, I would like to thank both Chinese Scholarship Council and Donghua University, who gave me the chance to pursue my PhD degree here at Queen Mary, University of London.

I would also like to thank all the group members from both groups, who made this journey really enjoyable and pleasant. I still remember the time when Ed showed me how to set up the first polymerization and the moment I laughed at his \bar{M}_n 1.5 polymer while I didn't have even a polymer yet, # still the best PhD; Also our 'old and new' Ben showed and explained to me the cool freeze-pump-thaw tricks and all the comforts after the first lab pub when I was very sad (Well, now it all changed); Also Gokhan, who is the candy of the group, of course with all the Turkish dances and the very good memory with all the lyrics; Then it comes to our Richard, oh no, Resat! Who is like my old brother and helped me so much in terms of almost everything; Also Tian for the days we spent in the lab working on our polycaprolactone; Then Manuel came with all the spirits towards chemistry and brought so many wonderful trips; Followed on him, probably the happiest man in the world came to our lab: Vali. Who organized lots of parties and of course the most important one: Annual Hotpot Festival! Of course, I

would like to thank another Asian spirit in our group, Tieshuai, who I had known for years and thanks for all the time we spend together; Also our new members, Ale and Ben, who is always helpful whenever you need them. I would also like to thank Dr. Dharmesh Patel, who spent lots of time on discussing projects with me and teaching me lab skills; Also Marta who help me when I am running my mechanical testing; And the new group members, Tony and Gamal, who offered me a lots of help during my last months of my PhD; Also other groups members, Chavanunne, Daniel, Martin, Dominic, Norlaily, Elham, Yamin, Cigdem, Frederico, Martina, Connor and my only student Jing, I would like to thank you guys for all the support! It's really a great pleasure to work with you!

Wait, did I forget someone? Of course, I would like to say a special thank you to my best friend Suzan, who helped me so so so much! Our friendship is definitely one of the most important treasures I found in my life!

I would like to thank my friends from SEMS who I have had so many good memories with. Also all the technicians and administrative staff from SEMS, Nano force and Nano vision, who provided so many support during my study.

I would give a special thanks to my friends from high school, for all the help before I came here and also the time you spend with my family when I am here. I could not imagine anything better than that. I am so lucky to have you guys behind my back!

Lastly, I would like to thank my father, Liu Tao, and girlfriend, Ma Zhiyan, the two most important persons in my life, for all your patience, kindness and of course all the love you shared with me. Without any of you, I will never reach this day.

Abstract

Tendons transfer forces from muscle to bone and allow the locomotion of the body. However, tendons, especially for tendons in the hand, get lacerated commonly in different injuries and the healing of tendon within the narrow channel in the hand will normally lead to tendon adhesion and sacrificed tendon mechanics. Researches have been focused on addressing tendon adhesion prevention but neglecting healed tendon mechanics.

This thesis discusses the principles and challenges in the design of biomaterials regarding flexor tendon repair with advanced polymer chemistry and materials science. A rational platform, not only focusing on the prevention of tendon adhesion, but devoting more efforts on final healed properties of tendons via implementing glycopolymer-based materials to guide tendon cells attachment, was designed, fabricated and characterized.

Controlled ring opening polymerizations and atom transfer radical polymerizations were combined for the synthesis of miktoarm well-defined block copolymers. Para-fluorine click reactions were then implemented to afford glycopolymers with glucose units.

Obtained copolymers were transformed into 3D membranes constituting a porous fibrous structure utilizing electrospinning. The aligned structure was then fabricated to optimize the mechanics of these materials for practical application as well as reconstruct normal tendon physiological structure.

Lastly, the toxicity, cell affinity and cell activity of obtained materials were evaluated *in vitro* employing tendon cells as a cell line to confirm the suitability of obtained platforms for flexor tendon repair.

Table of contents

Statement of Originality	ii
Acknowledgments	iii
Abstract.....	v
Table of contents.....	vi
List of Figures.....	xi
List of Tables.....	xxiv
List of Abbreviations.....	xxv
Chapter 1 Introduction.....	1
1.1 Polymer synthesis, post-polymerization modification and macromolecular structure design	1
1.1.1 Living chain growth polymerization.....	2
1.1.1.1 Living ionic polymerization	2
1.1.1.2 Living ring opening polymerization.....	4
1.1.1.2.1 Living ring opening polymerization of cyclic esters.....	4
1.1.1.3 Living ring opening metathesis polymerization	7
1.1.1.4 Living radical polymerization	8
1.1.1.4.1 Nitroxide mediated polymerization	9
1.1.1.4.2 Atom transfer radical polymerization	10
1.1.1.4.3 Reversible Addition-Fragmentation chain Transfer polymerization.....	12
1.1.1.4.4 Single electron transfer living radical polymerization	13
1.1.2 Post-polymerization modification reactions	15

1.1.2.1	Thiol addition	16
1.1.2.2	Para-fluorine click reaction	16
1.1.2.3	Azide-Alkyne Huisgen Cycloaddition reaction	18
1.1.3	Polymer structure, design and miktoarm polymers	18
1.2	Electrospinning	20
1.2.1	Electrospinning setup and process	20
1.2.2	Electrospinning parameters	22
1.2.3	Structure control in electrospinning	23
1.2.4	Electrospinning applications	25
1.3	Tendon structure and function.....	26
1.3.1	Tendon injuries.....	29
1.3.2	Tendon healing mechanism and challenges	31
1.3.2.1	Treatment to tendon adhesion prevention	35
1.4	Aims and objectives	41
Chapter 2. Polymer synthesis.....		43
2.1	Introduction.....	43
2.1.1	Synthetic biocompatible polymers.....	43
2.1.1.1	Polyesters	43
2.1.1.2	Polystyrene derivatives	44
2.1.1.3	Glycopolymers	46
2.2	Experimental overview and hypothesis	48
2.3	Materials and methods	48
2.3.1	Materials.....	48
2.3.2	Measurements and characterization	49
2.3.3	General synthesis procedures.....	50

2.3.3.1 ROP of ϵ -CL.....	50
2.3.3.2 ATRP of Styrene or PFS.....	51
2.3.3.3 Synthesis heterofunctional initiator	52
2.3.3.4 Synthesis of miktoarm block copolymers	54
2.3.3.5 Para-fluorine click reaction using 1-thio- β -D-glucose.....	55
2.3.3.6 Synthesis of thermo-responsive block copolymers.....	56
2.4 Results and discussion	57
2.4.1 Optimization of ROP of ϵ -CL	57
2.4.2 Optimization of ATRP of styrene and 2,3,4,5,6- pentafluorostyrene.....	61
2.4.3 Synthesis of heterofunctional initiator	63
2.4.4 Synthesis of miktoarm block copolymers using the heterofunctional initiator	64
2.4.5 Synthesis of miktoarm glycopolymer	68
2.4.6 Synthesis of thermo-responsive miktoarm block copolymers ..	71
2.5 Conclusion	74
Chapter 3. Materials development and optimization	75
3.1 Introduction.....	75
3.2 Experiments overview and hypotheses	76
3.3 Methods.....	76
3.3.1 Preparation of polymer electrospinning solutions	76
3.3.2 Electrospinning	77
3.3.3 Characterization of polymer membranes	78
3.3.4 The uniaxial tensile tests	79
3.3.5 Cyclic loading tests	80

3.3.6 Cyclic recovery tests	81
3.3.7 Statistical Analyses	81
3.4 Results and discussion	82
3.4.1 Optimization of electrospinning condition	82
3.4.2 Characterization of final polymer membranes	87
3.4.3 Mechanical properties of electrospun membranes	89
3.6 Conclusion	99

Chapter 4. *In vitro* biological characterization using tendon cells .101

4.1 Introduction	101
4.2 Experiment overview and hypotheses.....	101
4.3 Methods.....	102
4.3.1 Isolation of tendon cells from bovine joint	102
4.3.2 Polymer membrane and cell preparation for <i>in vitro</i> tests	102
4.3.3 Preliminary cell viability and affinity on membranes	103
4.3.4 <i>In vitro</i> preliminary cell adhesion and morphology assay	105
4.3.5 Preliminary cell viability and morphology on aligned membranes	106
4.3.6 Preliminary cell activity with the existence of different polymer-based membrane	107
4.3.7 Statistical Analyses	107
4.4 Results and discussion	108
4.4.1 Results of preliminary cell viability and affinity on membranes....	108
4.4.2 <i>In vitro</i> preliminary cell adhesion and morphology	112
4.2.3 Results of preliminary cell viability and morphology on aligned membranes	114
4.4.4 Influence of polymeric membranes over initial cell activity	119

4.5 Conclusion	121
Chapter 5 General discussion, conclusion and future work	123
5.1 General discussion	123
5.1.1 Synthesis of star shaped polymers	124
5.1.2 Materials design and optimization	126
5.1.3 <i>In vitro</i> preliminary cell biocompatible, cell attachment and cell activity tests.....	129
5.1.4 Limitations	131
5.2 Conclusion	132
5.3 Future work	134
References	136
Appendix	169

List of Figures

- Figure 1.1** (a) Anionic polymerization of styrene with butyl lithium as initiator and (b) cationic polymerization of styrene with etherate boron trifluoride/alcohol co-initiator in the presence of water, polymer chains were formed through the propagation of anionic and cationic species in each case.....3
- Figure 1.2** Polymerization mechanism for ring opening of ϵ -CL using $\text{Sn}(\text{Oct})_2$ as a catalyst and benzyl alcohol as an initiator; initiation step involves the formation of complex between benzyl alcohol and $\text{Sn}(\text{Oct})_2$ catalyst, followed by activation of cyclic monomer and ring opening process. Polymer chains were subsequently formed via monomers insertion and normally terminated through chain-transfer reactions....6
- Figure 1.3** (a) Intermolecular transesterification and (b) intramolecular transesterification reactions during ring opening polymerization of ϵ -CL. Both mechanisms will lead to the broadening of polymer dispersity.7
- Figure 1.4** General mechanism for ring opening metathesis polymerization. The initiation step involves the activation of monomer vinyl group by catalyst, followed by formation of 2 plus 2 addition and ring opening process. Then monomers were added in the same manner to form longer polymer chains. The reaction are normally terminated via the addition of termination reagent($\text{X}=\text{Y}$) to deactivate the transition metal and provide specific functional end group.8
- Figure 1.5** Scheme representation of nitroxide mediated polymerization process using MAMA-SG1 and styrene. Initiation involves the generation of radical species within the system and activation of styrene monomer; then monomers were added to the radical center and radical concentration was controlled through the reversible activation and deactivation equilibrium with nitroxide to suppress the termination reactions.10

Figure 1.6 Equilibrium of atom transfer radical polymerization (ATRP). Radical formation involves the homolytic halogen transfer from alkyl halide to Cu halide ligand complex in lower oxidation state and active radical concentration was controlled by the redox reaction of higher oxidation state transition metal halide ligand complex. 11

Figure 1.7 General mechanism of RAFT. Initiation step normally involves the formation of radicals from radical source and activation of monomers. Then the propagating process allow the addition of monomers to radical centers, which go through reversible equilibrium mediated by CTA to achieve uniform chain length. . 13

Figure 1.8 General mechanism of SET-LRP. Radical formation involves the single electron transfer from the Cu(0) electron donor to the electron acceptor alkyl halide and active radical concentration was controlled by the redox reaction of higher oxidation state transition metal halide ligand complex. 15

Figure 1.9 Radical thiol addition to poly (1,2-butadiene). Radicals are generated from radical source and then react with thiol to afford thiyl radical species. Then the reaction propagates via thiyl radicals react with alkyne group to form a carbon center radical and follows by a chain transfer step to abstract the hydrogen from thiol to achieve multiple propagation. 16

Figure 1.10 Para-fluorine click reaction using (a) hydroxyl, (b) amine and (c) thiol terminated compound. 17

Figure 1.11 General representation of azide-alkyne cycloaddition reaction. 18

Figure 1.12 Representative process of miktoarm polymer synthesis via the arm-first and core-first methodology. Miktoarm polymers represent a category of polymers with at least two different polymer arms emanated from the same center. 19

Figure 1.13 Schematic representation of electron spinning setup. The main

components of electrospinning including a syringe pump, a high voltage supply, a spinneret and a ground collector.21

Figure 1.14 Scanning electron micrographs of electrospun PS sub-micron fibres showing morphology at varying magnifications. A–C are non-aligned, D–F are moderately aligned, and G–I are highly aligned sub-micron fibres. The images indicate effective control over fibre alignment can be achieved using electrospinning.24

Figure 1.15 (a) TEM and (b) SEM images of the co-axially electrospun fibres. Evident core shell fibril structure can be observed under electron microscopy and afford fibres with more complicated structure.25

Figure 1.16 Scheme representation of the hierarchal structure of tendon. The hierarchal structure of tendon accounts for the unique mechanical responses and function of tendons.27

Figure 1.17 Collagen fibril organization and morphology in mature rat tendon and ligament, white arrow indicate the existence of crimp on tendon tissue. From the images, it can be observed that in mature tendon tissue, collagen fibres are primarily aligned along the longitude of the tendon with crimps existing along the fibres (white arrow).27

Figure 1.18 Typical normal tendon stress-strain curve. This figure shows the mechanics of normal tendon tissue. The crimp on tendon tissue leads to the toe region of the curve and followed by the elastic mechanical behaviour until the physiological limit of tendon tissue. Further extension will lead to the appearance of microscopic failure and lastly, the rupture of tendon tissue, termed here as macroscopic failure. 28

Figure 1.19 SEM of rat Achilles tendon sheath. Different from the fibre arrangement in tendon tissue, tendon sheath appears to be a randomly fibril connecting tissue which helps the gliding of tendon against other tissue.29

Figure 1.20 Representative histologic sections of healthy and repaired canine flexor tendons at 9 days postoperatively. The sections were stained with Hematoxylin and eosin stain (H&E) and viewed under bright field for cell identification. The upper row shows the aligned fibre structure and arranged cell orientation in normal tendon tissue while the bottom row shows the disorganized fibre bundles and cell orientation.31

Figure 1.21 Schematic representation of (A) intrinsic and (B) extrinsic pathways of tendon healing. The intrinsic healing only involves the cells within tendons and the formation of connecting tissue was mostly located within tendons. In contrast, extrinsic healing leads to the formation of connecting tissue surrounding tendon, which subsequently leads to scar and adhesion formation.....32

Figure 1.22 Cellular phases of tendon healing. A: Inflammatory stage; B: Proliferative stage; C: Remodelling stage. Images show the three main stages during tendon healing. Inflammatory stage involves the inflammation reaction of human body and the initial migration of cells to the injured place; during migration stage, cells continue to proliferate and start to deposit disorganized immature collagen fibres; the remodelling stage is in charge of the reorganization and maturation of fibre bundles.33

Figure 1.23 Basic histology of adhesion development in mouse flexor tendon. T: tendon, ST: subcutaneous tissue, SS: sheath space, and B: bone. From image A, it can be observed there is a clear space between tendon and bone as well as tendon and subcutaneous tissue. Image B shows the invasion of cells into the injured place (black arrow). Image C shows the swelling of tendon and adherence with subcutaneous tissue (black arrow). Image D indicate the formation of adhesion after tendon healed (black arrow).35

Figure 1.24 Examples of tendon suture techniques; (a) Bunnell method; (b) Double modified Kessler method; (c) Savage method. Image a, b and c correspond to a two

strand, four strand and six strand suture method, respectively.37

Figure 1.25 Histology staining of Adhesion prevention combine (A) tenolysis and Sperafilm[®]; (B) Non treated group. Image A shows the sheath space formed after tendon healed and proved the efficiency in prevention of tendon adhesion compared with significant less sheath space in Image B, which has no treatment during the healing. Red arrow shows the sheath space formed during tendon healing.....39

Figure 1.26 Histology staining of (A) Control group; (B) PELA membranes; (C) 6% Ibuprofen PELG membranes. White arrow shows the adhesion tissue formed surrounding tendon while black arrow shows the sheath space. T stands for tendon tissue while A stands for adhesion tissue. It can be observed that there are several adhesion tissue from in control group (Image A). While some adhesion formed in the PELA treated group (Image B) and no adhesion formed in ibuprofen loaded PELA group (Image C).40

Figure 1.27 Schematic representation of bilayer biocompatible copolymers membrane for tendon adhesion prevention and tendon repair promotion. The outer hydrophobic layer will behave as an anti-adhesive layer while the inner glycopolymer-based layer will allow cell attachment and provide biological cues through the incorporation of sugar moieties.....42

Figure 2.1 Phase-contrast light microscopic images of adhering cell populations on PS treated with glow discharge for (A) 5 s; (B) 10 s; (C) 30 s; (D) 60 s and (E) TCPS; Cells were incubated for 48 h. Notable higher number of cells were observed on PS treated with longer glow discharge which has higher oxygen content.45

Figure 2.2 (a) Experimental design of gp120 functionalized surface for competitive binding studies; (b) Competition experiments on gp120 functionalized surface

between dendritic cell-specific intercellular adhesion molecule-3-grabbing non-integrin (DC-SIGN) and homo poly(D-mannose methacrylate) at a concentration range of 0-400 nM for the glycopolymers and 4 nM DC-SIGN.....	47
Figure 2.3 ROP of ϵ -CL using benzyl alcohol as an initiator.....	51
Figure 2.4 ATRP of PFS using EB <i>i</i> B as an initiator.....	52
Figure 2.5 Synthesis of the heterofunctional initiator (2).	53
Figure 2.6 ROP of ϵ -CL and then ATRP of PFS.	54
Figure 2.7 Para-fluorine click reaction using 1-thio- β -D-glucose.	55
Figure 2.8 SET-LRP of NIPAM and then ROP of ϵ -CL.....	57
Figure 2.9 GPC trace of PCL polymerized from non-distilled ϵ -CL.	58
Figure 2.10 GPC traces of polymers from the optimization reactions for ROP of ϵ -CL.	60
Figure 2.11 ^1H NMR of homo PCL. The result confirms the formation of polymers and complete removal of solvent and left-over monomers.....	61
Figure 2.12 GPC traces obtained from ATRP of (a) styrene and (b) PFS at different time points. GPC traces show the growth of the polymers after the chain extension step. Additionally, chain-chain coupling reactions, which leads to increase of polymer dispersity, were observed in the polymers after longer reaction time.....	62
Figure 2.13. ^1H NMR of homo (a) PS and (b) PPFS. The result confirms the formation of polymers and complete removal of solvent and left-over monomers.....	63
Figure 2.14 ^1H NMR of the heterofunctional initiator (2). NMR Spectrum confirms the chemical structure and the purity of the structure in the final product.	64
Figure 2.15 GPC traces of (a) PS first and then PCL and (b) PCL first then PS. The GPC traces show the growth of polymer chains after chain extension reactions. However, lower molecular weight polymers were formed when using PS as the macro	

initiator while only block copolymers were synthesized utilizing PCL as the macro initiator.65

Figure 2.16 GPC traces of (a) PCL-*mikto*-PS and (b) PCL-*mikto*-PPFS at different time points using the PCL macroinitiator; (c) styrene and (d) PFS monomer conversion by ¹H NMR with time; (e) and (f) molecular weight and Đ of block copolymers. The GPC traces (a) and (b) show the complete growth of the macro initiator during the chain extension reactions. Images (c), (d), (e) and (f) shows the linear relationship between molecular weight with time and conversion. The Đ of polymers also maintains low during the polymerization which shows the successful control over polymerization.....67

Figure 2.17 ¹H NMR of purified (a) PCL-*mikto*-PS and (b) PCL-*mikto*-PPFS. The result confirms the formation of block polymers and complete removal of solvent and left-over monomers.68

Figure 2.18 (a) GPC traces and (b) ¹⁹F NMR of PCL-*mikto*-PPFS and PCL-*mikto*-PTFSGlc. The GPC traces (a) shows the growth of polymer chains and (b) ¹⁹F NMR shows the complete consumption of *para*-fluorine in the polymers.....69

Figure 2.19 ¹H NMR of purified PCL-*mikto*-PTFSGlc. The result confirms the formation of glycopolymers after the *para*-fluorine click reactions.70

Figure 2.20 Reaction mixture using (a) 3: 1, (b) 2: 1 and (c) 1: 1 water: THF volume ratio. Image (a) shows the formation of polymer precipitates in 3:1 water: THF mixture. Dispersion solution without large aggregation (Image b) was observed with the increase in water: THF ratio to 2:1 and clear soluble reaction mixture was formed with further increase in THF amount to 50 %.....72

Figure 2.21 GPC traces of PCL-*mikto*-PNIPAM in (a) 2:1 and (b) 1:1 water/THF volume. All the GPC traces show the growth of polymer chains after chain extension

reactions. However, significant lower amount of uninitiated macro initiator was left in the system with higher THF ratio.....73

Figure 2.22 ¹H NMR of purified PCL-*mikto*-PNIPAM. The result confirms the formation of PCL-*mikto*-PNIPAM after the chain extension reactions.73

Figure 3.1 Schematic representation of electrospun solution preparation and electrospinning setup for membranes with different fibre orientation. The fibres alignment was adjusted by changing the collector type and utilized the dragging force to align the fibre bundles.....78

Figure 3.2 A typical SEM image of PCL electrospun fibres in (A) 1:1; (B) 1:3 and (C) 1:5; weight ratio CHCl₃: DMF solutions; Images show the influence of solvent volatility and dielectric constant on fibre form; Scale bar represents 10 μm in all pictures.82

Figure 3.3 A typical SEM image of electrospun fibres of (A) 15 wt. %; (B) 20 wt. % and (C) 25 % wt. % PCL in CHCl₃ and DMF mixture; Low concentration led to non-uniformed fibres while high concentration led to beaded fibres; Scale bar represents 10 μm in all pictures.....83

Figure 3.4 Typical SEM images of electrospun fibres at (A) 20 KV; (B) 25 KV and (C) 30 KV using 20% wt. % PCL solution; Higher voltage generated thinner fibres bundles; Scale bar represents 10 μm in all pictures.84

Figure 3.5 A typical SEM image of (A) random and (B) aligned PCL electrospun fibres with corresponding angle plot below; Fibre alignment has been controlled via adjusting collector type; Scale bar represents 10 μm in all pictures.....85

Figure 3.6 Scheme of polymer synthesis route and detailed chemical structures of each polymer.....86

Figure 3.7 A typical SEM image of both random and aligned polymer membranes, with inset showing a matched typical water contact angle result. Mean fibre diameter and water contact angle across all analyzed samples are presented with fibre diameter distribution graph combining all analyzed fibres. Scale bar represents 10 μm in all pictures. All fibres possess a smooth surface with slightly thinner fibres within aligned fibres systems.88

Figure 3.8 (a) Fibres diameters and (b) water contact angle of different membranes. Changes in chemical composition did not alter fibre diameter significantly, but dramatically affected the surface hydrophobicity.89

Figure 3.9 Representative pull to failure curves for both random (a-b) and aligned polymer membranes (P1-P4; with (c-d) and against the fibre (e-f)). All the samples were pulled to failure at 1 % strain/s. Note the substantial variation of scale on the Y-axis denoted the substantially improved failure properties for aligned fibre systems.91

Figure 3.10 Comparison of mean (a) force, (b) stress and (c) strain between all random and aligned polymer membranes groups. Significantly higher failure properties and slightly decreased strain were observed when samples were loaded with the fibre direction.....92

Figure 3.11 Comparison graphs of maximum modulus between all random and aligned polymer membranes groups. Significant higher stiffness was witnessed when loaded with fibre direction compared with the rest groups.....92

Figure 3.12 Representative cyclic loading curves for both random and aligned polymer membranes (P1-P4). (a) Random fibre samples and (b) aligned fibre samples (loaded with the fibre direction). Note the substantial variation of scale on the Y-axis indicated the considerably higher failure properties of aligned fibre systems.....93

Figure 3.13 Comparison graphs of the maximum modulus (a) with cycle 1 and (b) without cycle 1 between all random and aligned polymer membranes groups. Notable higher stiffness was observed when loaded with fibre direction compared with the rest groups and a higher maximum modulus evident after the first loading cycle.94

Figure 3.14 (a) Representative stress-strain curves showing cyclic loading followed by a pull to failure for aligned P4 materials. Samples were pulled to 10 %, 20 % or 30 % strain cycles and then returned to 0% strain for 30 minutes before repeating the 10 loading cycles and then pulling failure at 1 % strain s⁻¹. (b) Extracted stress-strain curves of the first and last ten cycles; (c) A direct comparison of the extracted stress-strain curve (30 % strain) of the last cycle from first loading batch and the first cycle from the second loading batch. Samples show slightly recovery of mechanical properties after 30 minutes of holding at the original position.96

Figure 3.15 Cyclic loading curves for aligned P4 membranes, subjected to two batches of ten loading cycles, with a 24 hours recovery period between batches. Curved show stress-strain data for the first two cycles before and after recovery for two individual samples.97

Figure 3.16 A SEM image of both a random and aligned polymer membrane, before and after being stretched to 30 % strain; A frequency distributions of fibre diameter and angle plot of fibre alignment is shown for each image. Scale bar represents 10 µm in all pictures, no notable change in fibre orientation was observed after the loading cycles.98

Figure 4.1 Schematic representation of samples preparation for *in vitro* cell tests using live-dead assay, cytoskeleton assay and Alamar blue assay. 103

Figure 4.2 Typical images of the live-dead assay with tendon cells on random P1-P4

polymer membranes, PEG and positive and negative control surfaces after (a) 24 hours and (b) 48 hours. Viable cells are shown in green and dead cells in red. Scale bar represents 200 μm in all pictures. Significant higher number of cells could be observed on P4 membrane compared with P1-P3 groups. 109

Figure 4.3 Comparison of cell viability on P1-P4 membranes and the tissue plastic controls at 24 hour and 48 hour time points. All the membranes maintain higher than 60 % cell viability after 48 hours incubation without significant different between membranes. 110

Figure 4.4 Comparison of cell number on different membranes and the tissue plastic controls at 24 hour and 48 hour time points; * represent significant the indicate group different from all other groups of data. Significant higher number of viable cells were observed on P4 membrane compared with P1-P3..... 110

Figure 4.5 Comparison of viable cell coverage between different membranes and tissue culture plastic controls at the (a) 24 hour and (b) 48 hour time points. Significant higher of cell coverage was observed on P4 membrane compared with P1-P3..... 111

Figure 4.6 Typical images of tendon cells seeded onto each of the polymer membranes (P1 to P4) and on tissue culture plastic (control). Green staining represents the cytoskeleton while blue represents the nucleus of cells. Images show cells after 24 hours (left columns), and 48 hours (right columns). Two different magnifications are shown for each condition: the white scale bar represents 100 μm ; the grey scale bar represents 25 μm . Greater cytoskeleton tension was observed on the P4-R membrane relative to the rounder cells on P1-P3-R membranes during the first 48 hours. 113

Figure 4.7 Live/dead assay of tendon cells on random and aligned P1-P4 polymer membranes after (a) 24 hours and (b) 48 hours. Viable cells are shown in green and dead cells in red. Scale bar represents 200 μm in all pictures. Significant higher

number of cells could be observed on P4 membrane with different cell attach pattern on random and aligned fibres.....	115
Figure 4.8 Live tendon cells on (a) random and (b) aligned P4 membranes at 2.5 magnification. Scale bar represents 1 mm in all pictures. Different initial cell attachment pattern was observed at low magnification.	116
Figure 4.9 Comparison of preliminary cell viability across aligned P1-P4 membranes, at 24 hour and 48 hour time points. All the membranes maintain higher than 60 % cell viability after 48 hours incubation without significant different between membranes.	116
Figure 4.10 Typical images of tendon cells seeded onto both random and aligned polymer membranes (P1 to P4). Green staining represents the cytoskeleton while blue represents the nucleus of cells. Images show cells after (a) 24 hours and (b) 48 hours. Two different magnifications are shown for each condition: the white scale bar represents 100 μm ; the grey scale bar represents 25 μm	118
Figure 4.11 Confocal images of tendon cells on (a) random and (b) aligned P4 membranes at 10 magnification. Scale bar represents 400 μm in all pictures.	119
Figure 4.12 Histograms of cell actin and nucleus distribution in both random and aligned fibre systems. A significant difference was witnessed between groups. Aligned fibre systems resulted in clear cell alignment in the fibre direction.	119
Figure 4.13 Comparison of cell activity in control cells on tissue culture plastic plates. Data compares activity at different time points. The normality of the data was characterized using Shapiro-Wilk normality tests, indicating a non-normal distribution of the data. Results are expressed as box-whisker plots. Statistical significance was calculated using Kruskal-Wallis tests followed by Dunn's tests.....	120
Figure 4.14 Comparison of cell activity between different membranes at different time	

points. Values represent the mean \pm SD normalized to the activity of control cells at the same time (Set as 1.0) (n = 3). Statistical significance was calculated using the Kruskal-Wallis tests followed by Dunn's tests. 121

List of Tables

Table 2.1 Summary of the results obtained from the optimization reactions for ROP of ϵ -CL	60
Table 2.2 Summary of the results of PCL, PCL- <i>mikto</i> -PS, PCL- <i>mikto</i> -PPFS and PCL- <i>mikto</i> -PTFSGlc.....	70
Table 3.1 Composition of solutions for electrospun membranes.	86

List of Abbreviations

AAc	Azide-Alkyne Huisgen Cycloaddition
ATRP	Atom transfer radical polymerization
bFGF	Basic fibroblast growth factor
Bibb	α -Bromoisobutyryl bromide
BSA	Bovine serum albumin
CDCl ₃	Chloroform-d
CEL	Cellulose
CTA	Chain transfer agent
Cu(I)Br	Copper(I) bromide
DAPI	4',6-diamidino-2-phenylindole
DBU	1,8-Diazabicyclo[5.4.0]undec-7-ene
Dm	Dead cells on materials
DMEM	Dulbecco's Modified Eagle Medium
DMF	Dimethylformamide
Dw	Dead cells in well
EBiB	Ethyl α -bromoisobutyrate
FDA	Food and Drug Administration
FDP	Flexor digitorum profundus
FDS	Flexor digitorum superficialis
FFT	Fast Fourier Transform
GPC	Gel Permeation Chromatography
HA	Hyaluronic acid
HA-CMC	Hyaluronate-carboxymethylcellulose

HCl	Hydrochloric acid
HEPES	<i>N</i> -2-hydroxyethylpiperazine- <i>N</i> -2-ethane sulfonic acid
LCST	Lower critical solution temperature
Lm	Live cells on materials
Lw	Live cells in well
NFM	Nano fibrous membrane
NIPAM	<i>N</i> -Isopropylacrylamide
NMP	Nitroxide-mediated polymerization
NMR	Nuclear Magnetic Resonance
NSAIDs	Non-steroidal anti-inflammatory drugs
PBS	Phosphate-buffered saline
PCL	Poly (ϵ -caprolactone)
PCL- <i>g</i> -CS	Chitosan-grafted poly(ϵ -caprolactone)
PDCF	Platelet-derived growth factor
\mathcal{D}	Dispersity
PELA	Poly(lactic acid)-poly(ethylene glycol)
PET	Polyethylene terephthalate
PFS	2,3,4,5,6-Pentafluorostyrene
PGA	Poly(glycolic acid)
PLA	Poly(lactic acid)
PMDETA	<i>N,N,N',N'',N''</i> -Pentamethyldiethylenetriamine
PMMA	Poly(methyl methacrylate)
Poly (AN- <i>co</i> -TMI)	Poly(acrylonitrile- <i>c</i> - α,α -dimethyl meta-isopropenylbenzyl isocyanate)
PTFE	Poly(tetrafluoroethylene)

RAFT	Reversible addition-fragmentation chain transfer
RT	Room temperature
SAARDs	Slow acting anti-rheumatic drugs
SET-LRP	Single electron transfer-living radical polymerization
TEA	Triethylamine
TGF- β	Transforming growth factor- β
THF	Tetrahydrofuran
TMS	Tetramethylsilane
UV	Ultraviolet
VEGF	Vascular endothelial growth factor
WCA	Water contact angle

Chapter 1 Introduction

As one of the biggest challenges across the world, more than 30 million humans suffer from tendon related surgeries annually worldwide and more than £1 billion was spent on tendon related injuries in 2013¹. Tendon healing could take up to four years to fully finish² and commonly comes with complications such as tendon adhesion and loss of mechanics³ caused by the complicate tendon healing mechanisms. Researches have been focused on prevention of tendon adhesion utilizing chemical agents⁴, early mobilization⁵, and physical barrier⁶. Most effective treatment over adhesion was observed using polymeric materials and two commercial products, Septrafilm® and DegraPol®, are available on market to reduce the adhesion formation⁷⁻⁸. However, the mechanics and function of healed tendons are commonly sacrificed which potentially could make tendons liable to re-rupture. With the advancement of polymer chemistry and material science, polymers with more sophisticated structures and materials with more functionalities could be designed and achieved nowadays. These developments should be combined for optimal tendon treatments and to achieve better tendon healing results.

1.1 Polymer synthesis, post-polymerization modification and macromolecular structure design

Macromolecules, defined as molecules of relatively high molecular mass, comprise multiple repetitions of units derived, actually or conceptually, from molecules with relatively low molar mass⁹. Polymers are substances composed of macromolecules, have been widely involved in daily life, ranging from biopolymers including proteins and DNA, to synthetic polymers such as polystyrene, poly(ethylene terephthalate) (PET), and poly(methyl methacrylate) (PMMA).

The majority of polymers are commonly synthesized through step-growth polymerizations, chain-growth polymerizations or multistep-growth¹⁰. This chapter will mainly focus on the introduction of living chain growth polymerization techniques, post-polymerization modification reactions, and related macromolecular structure design as well as their utilization in various applications.

1.1.1 Living chain growth polymerization

Generally, chain growth polymerization can be categorized as conventional chain growth polymerization and living chain growth polymerization¹⁰. Conventional chain growth polymerization represents reactions, which contain early termination reactions and these normally lead to the loss of chain livingness and the ability for further chain extension.

The emergence of living chain growth polymerization allows a precise control over polymer properties, such as chemical compositions, topology and tacticity, which enable the synthesis of polymers with sophisticated structures. Living polymerizations can be categorized into living ionic polymerization¹¹, living ring opening polymerization¹², living ring opening metathesis polymerization¹³ and living radical polymerization¹⁴⁻¹⁸. Compared to conventional polymerization techniques, the living polymerization represents reactions with minimized termination with the ability to synthesize block copolymers. Generally, these techniques allow the design and fabrication of materials with tailored properties.

1.1.1.1 Living ionic polymerization

The first living anionic polymerization was introduced by Szwarc in 1956, during which polymerization of styrene was initiated by aromatic anions and propagated via

anionic species¹¹. First living cationic polymerization was reported in 1984 by Sawamoto and Higashimura¹³. These mechanisms both involve the formation and propagation of ionic species during the polymerization and can be categorized into either anionic polymerization (

Figure 1.1 (a)) or cationic polymerization (

Figure 1.1 (b))¹⁹ depends on the ion species at the propagating chain end. Bimolecular termination was eliminated in these systems due to the electrostatic repulsion of similar charges. However, the selectivity of ionic polymerizations over monomer type and the strict purification steps, restrict the applications of ionic polymerizations compared with living radical systems.

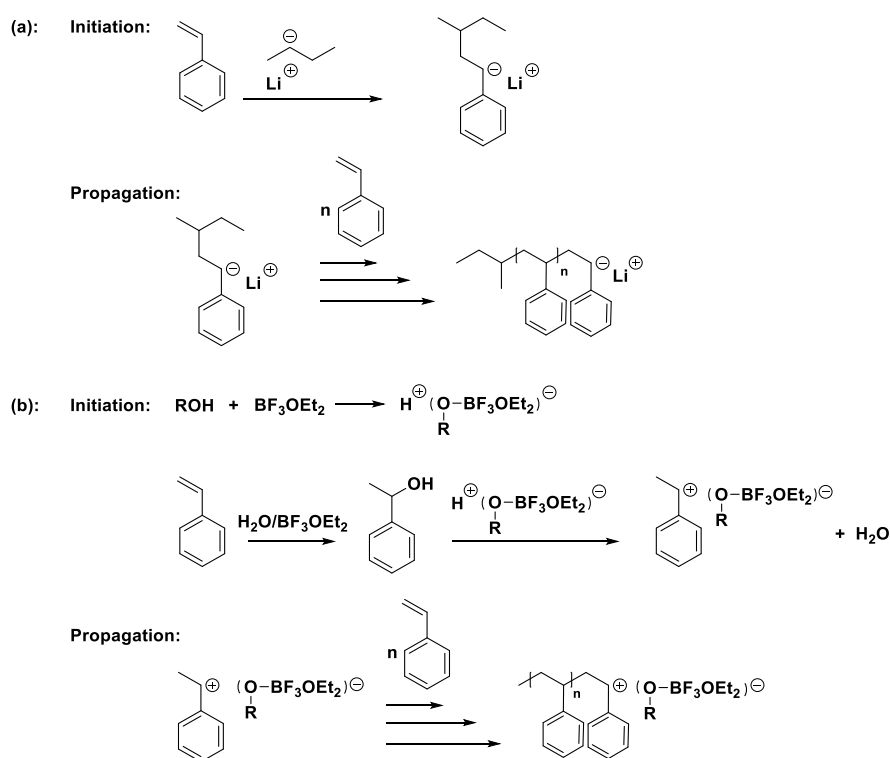


Figure 1.1 (a) Anionic polymerization of styrene with butyl lithium as initiator and (b) cationic polymerization of styrene with etherate boron trifluoride/alcohol co-initiator in the presence of water, polymer chains were formed through the propagation of

anionic and cationic species in each case.

1.1.1.2 Living ring opening polymerization

Ring opening polymerization, which represents polymerization in which cyclic monomers generate monomeric units with acyclic or fewer cycles than the original molecules⁹, was first introduced by Leuchs in the beginning of 1900s for the synthesis of polypeptides¹². As one of the families that have been applied in different biomedical fields, the synthesis of polyesters was used here as examples to introduce ROP in more details.

1.1.1.2.1 Living ring opening polymerization of cyclic esters

For the synthesis of polyesters, living ring opening polymerization provides several advantages when compared to polycondensation. This technique requires milder reaction conditions and there are fewer possibilities for side reactions, which lead to a better control over the characteristics of resulting polymers. Ring opening polymerization of a cyclic ester can be achieved by means of different mechanisms, including cationic ROP²⁰, anionic ROP²¹ and insertion-coordination ROP²² by implementing different catalytic system, such as organic, metal-based and enzymes catalyst²²⁻²³.

Poly (ϵ -caprolactone) (PCL) has been one of the most widely employed polyesters as it was approved by the FDA for human clinical applications and has been utilized in biomedical applications for a long time. Polymerization mechanisms will be discussed in more details, with the main focus on ROP of ϵ -CL.

ϵ -CL can be polymerized via cationic, anionic, monomer-activated, or coordination insertion mechanisms²². However, anionic ROP and insertion-coordination ROP were

normally utilized to afford PCL with high molecular²². A strong base is normally used to catalyze the anionic polymerization of ϵ -CL, which generally affords faster reaction rates but also instability of the propagating species. Coordination-insertion is another widely used mechanism to obtain well-defined molecular properties and complicated structures (Figure 1.2). Normally, metal alkoxides or carboxylates, **1**, within this system perform as coordination initiators rather than anionic initiators. With the addition of initiator **2** (like alcohol or amine), the polymerization initiates via acyloxygen cleavage of the monomer followed by the insertion of the monomer into the metal-oxygen bond. This coordination between the exocyclic oxygen and the metal results in the polarization and makes the carbonyl carbon of the monomer, **3**, more susceptible for nucleophilic attack, which leads to the formation of polymers **4**. One type of termination reaction under this mechanism caused the reaction between active polymer chain and non-initiating alcohol species, **5**, normally water. Thus, in the case of the ring-opening polymerization, ensuring the absence of water within the system is one of the crucial steps during the reaction setup.

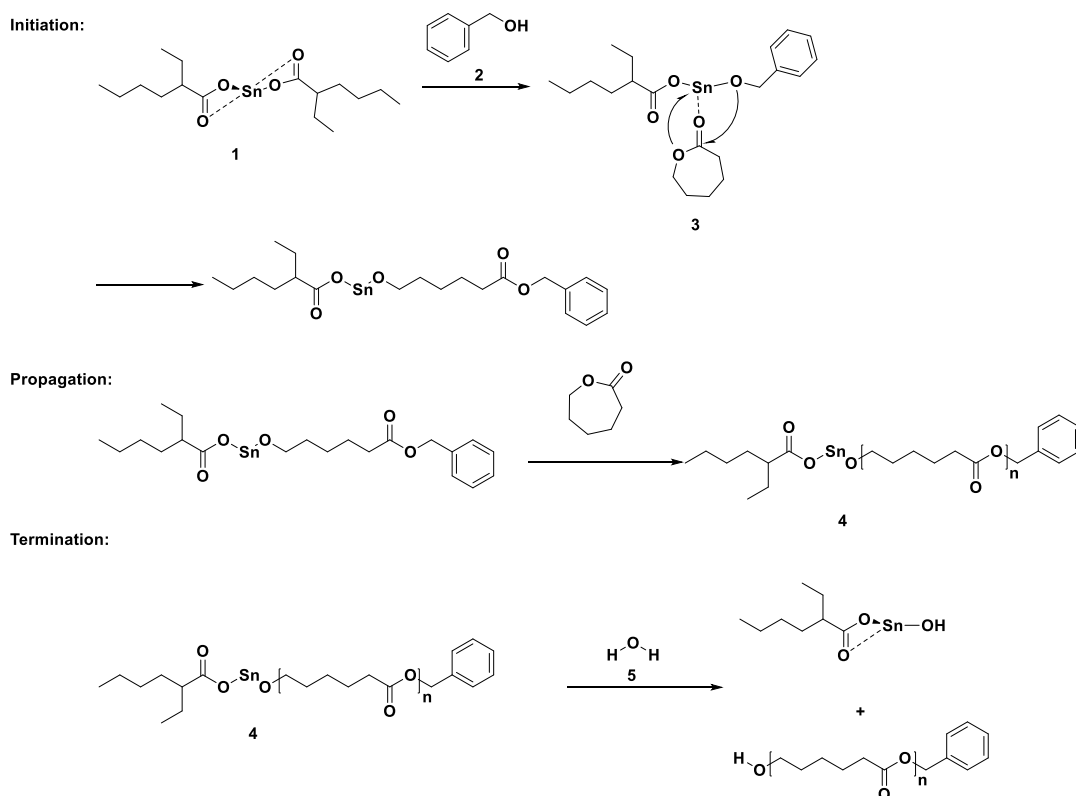


Figure 1.2 Polymerization mechanism for ring opening of ϵ -CL using $\text{Sn}(\text{Oct})_2$ as a catalyst and benzyl alcohol as an initiator; initiation step involves the formation of a complex between benzyl alcohol and $\text{Sn}(\text{Oct})_2$ catalyst, followed by activation of cyclic monomer and ring opening process. Polymer chains were subsequently formed via monomers insertion and normally terminated through chain-transfer reactions.

Most commonly observed side reactions during the polymerization under this mechanism, defined as intermolecular and intramolecular transesterifications, were attributed to the high reaction temperature and long reaction time²². These type of side reactions mostly happen at the late stages of polymerization and normally leads to a broad polydispersity of final polymers²² (Figure 1.3).

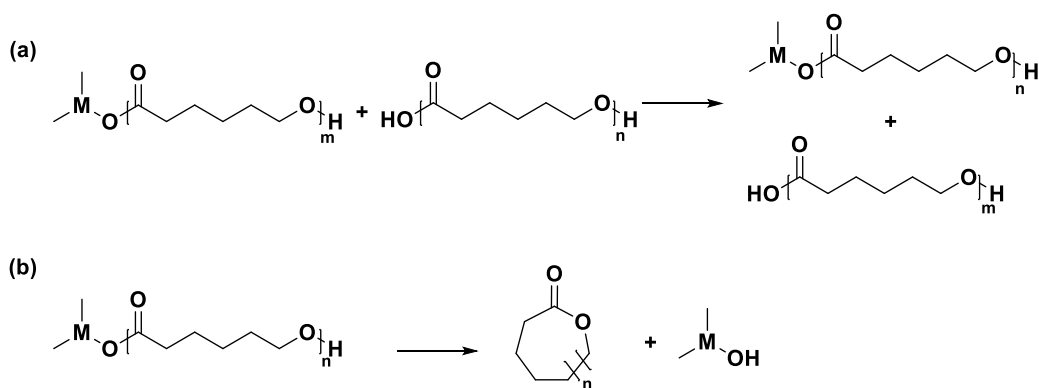


Figure 1.3 (a) Intermolecular transesterification and (b) intramolecular transesterification reactions during ring opening polymerization of ϵ -CL. Both mechanisms will lead to the broadening of polymer dispersity.

Although PCL was widely applied in the biomedical fields, it still has a number of limitations, namely its hydrophobic nature and lack of functional groups or biological cues on its backbone, restricting its applications in biological systems or ability to interact with cells. Aiding to improve this, ring-opening polymerization was normally combined with radical polymerization techniques to integrate functional groups onto PCL backbone²⁴⁻²⁵.

1.1.1.3 Living ring opening metathesis polymerization

Living ring opening metathesis polymerization was first introduced by Grubbs and Gilliom in 1986²⁶, which indicates a category of reaction in where a mixture of cyclic olefins is transformed into a polymer chain²⁷. The proposed general mechanism for living ring opening metathesis polymerization can be found in Figure 1.4²⁷. The initiation step involves the coordination process between a transition metal alkylidene complex **1** and a cyclic olefin **2**, followed by a [2+2] cycloaddition and transformed into a growing chain **3**. Then the monomer was subsequently added to the growing chain until the full consumption of the monomer and formation of polymers **4**. The

termination reaction normally involves adding deactivation species into the system. It has been applied for the fabrication of copolymers with well-defined topologies and utilized in biological and electronic fields²⁷.

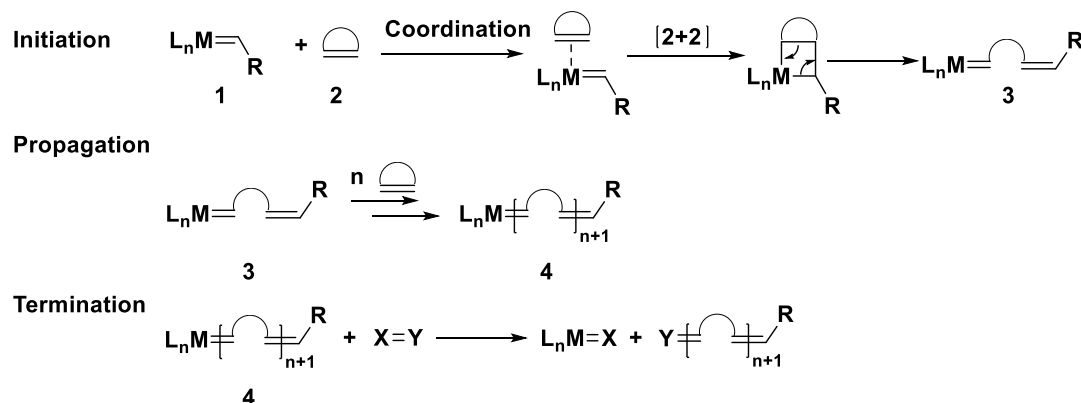


Figure 1.4 General mechanism for ring opening metathesis polymerization. The initiation step involves the activation of the monomer vinyl group by a catalyst, followed by the formation of 2 plus 2 addition and ring opening process. Then monomers were added in the same manner to form longer polymer chains. The reaction is normally terminated via the addition of termination reagent(X=Y) to deactivate the transition metal and provide specific functional end group.

1.1.1.4 Living radical polymerization

Inspired by living ionic system and aiming at designed polymers with a defined structure, living radical polymerization, also known as controlled radical polymerization, was discovered in the 1990s with splendid advancements over the last few decades¹⁰. Living radical polymerization represents the radical polymerization with minimized termination reaction, which is normally achieved by having an equilibrium between the radical species and dormant chains to maintain a constant concentration of radical species within the systems, until the full consumption of monomers²⁸. Other than these, monomer conversion follows a linear correlation with reaction time, which means the polymerization process can be easily monitored and the polymeric properties can be predetermined or adjusted throughout the process. The obtained polymers generally possess a desired molecular weight and low molecular

weight dispersity (\bar{M}_w/\bar{M}_n). Among these systems, polymer chains with a radical at the end normally have longer ‘living’ time, which offers the opportunity to design multi-block copolymers with sophisticated structures.

Different polymerization techniques were introduced since then to adapt different monomer types, temperature range and solvent systems, which allows the generation of materials with defined properties for different applications. According to the equilibrium within the system, controlled radical polymerization can be divided mainly into four main techniques, namely nitroxide-mediated polymerization (NMP)¹⁶ atom transfer radical polymerization (ATRP)¹⁴⁻¹⁵, reversible addition-fragmentation chain transfer (RAFT) polymerization¹⁷ and single electron transfer-living radical polymerization (SET-LRP)¹⁸.

1.1.1.4.1 Nitroxide mediated polymerization

The first successful living radical polymerization using a nitroxide group as an intermediate was developed and published by Solomon in 1986¹⁶. Back then, both acrylates and styrene derivatives were polymerized using nitroxide and alkoxyamines, to achieve control over final polymer structure. NMP based on a reversible equilibrium between propagating radicals and stable alkoxyamines, which present as predominant species (Figure 1.5), to prevent termination reaction²⁹. NMP can go through either a mono-component³⁰ or bicomponent systems³¹ which allow the combination of NMP with traditional free radical initiators. The cleavage of nitroxide and formation of radicals were normally governed by the temperature which allows the easy control over polymerization²⁹. The reversible activation and deactivation process also provides the possibility of chain extension using the macro-nitroxide to design multiblock copolymers. Nitroxides are normally synthesized via the oxidation of

amine or hydroxyl amine³²⁻³³. The stability of nitroxides mainly depends on the side group of nitrogen and slightly influenced by side groups on oxygen³⁴. It was also proved that steric hindrance can attribute to the stability of nitroxide which allows the easy storage of most commercial nitroxides³⁵. However, the synthesis of nitroxides and compatibility with monomer types restrict the applications of this technique.

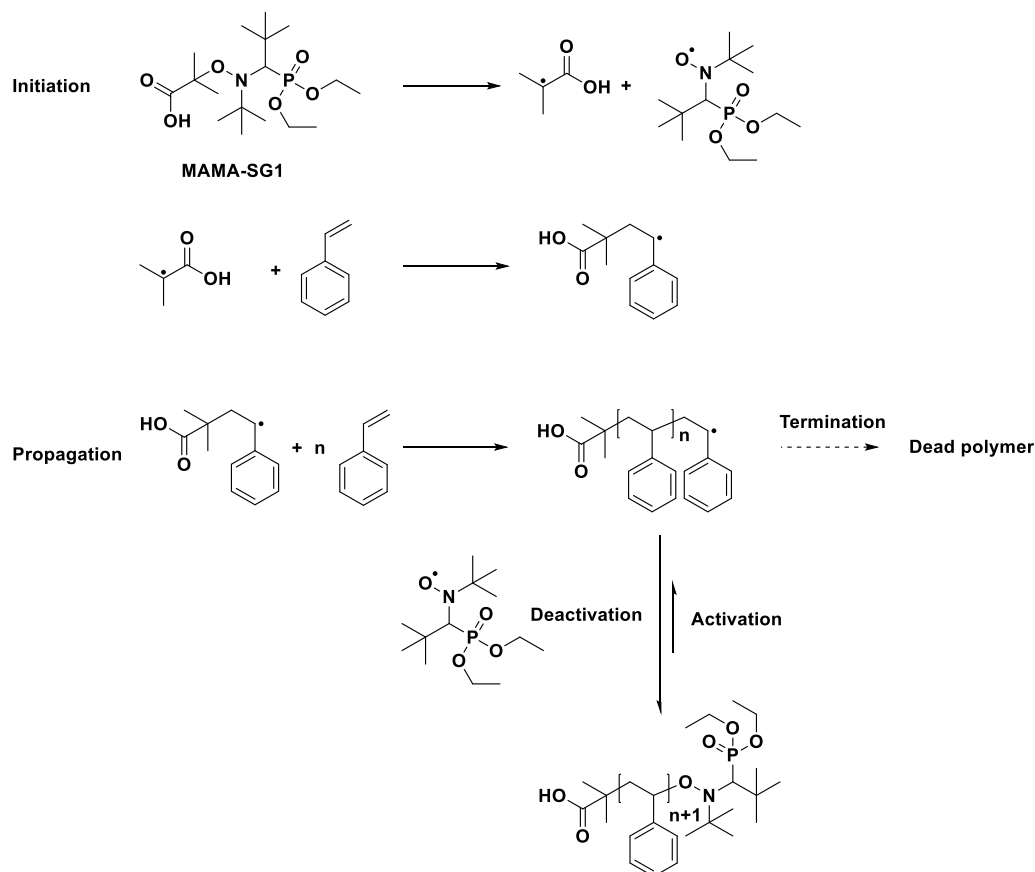


Figure 1.5 Scheme representation of nitroxide mediated polymerization process using MAMA-SG1 and styrene. Initiation involves the generation of radical species within the system and activation of styrene monomer; then monomers were added to the radical center and radical concentration was controlled through the reversible activation and deactivation equilibrium with nitroxide to suppress the termination reactions.

1.1.1.4.2 Atom transfer radical polymerization

Atom transfer radical polymerization was discovered independently by Sawamoto¹⁴ and Matyjaszewski¹⁵ in 1995. ATRP is mainly based on establishing a rapid dynamic

equilibrium between a minute amount of growing active radicals and a large majority of the dormant species³⁶. The overall mechanism of Cu catalyzed ATRP can be seen in Figure 1.6³⁷. The deactivation process is more prominent in the equilibration to maintain a low radical concentration and minimize the rate of termination reaction. Alkyl halides, **1**, are typical initiators for ATRP, where X usually defines bromine or chlorine, which lead to a better control on the molecular weight and Đ of final polymers out of the suitable rate between activated and deactivated species. To initiate the reaction, lower oxidation copper ligand complexes, **2**, will activate the initiator and generate radical species. However, the significant higher deactivation rate originates from Cu(II) halides, **3**, maintains a lower radical concentration within the system and successfully suppress the termination reactions.

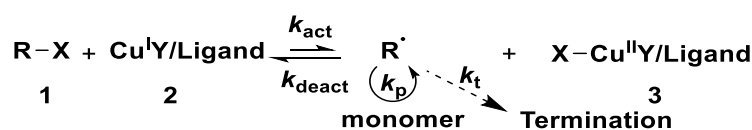


Figure 1.6 Equilibrium of atom transfer radical polymerization (ATRP). Radical formation involves the homolytic halogen transfer from alkyl halide to Cu halide ligand complex in lower oxidation state and active radical concentration was controlled by the redox reaction of higher oxidation state transition metal halide ligand complex.

Since this technique is benefiting from its wide ranging monomer compatibility and simple design of initiators, well-defined polymers with numerous properties and applications have been synthesized using ATRP³⁶. Meanwhile, benefit from the simple structure of the initiator, ATRP can be easily combined with other polymerization techniques. For example, Atzet et al. have synthesized poly(2-hydroxyethyl methacrylate)-*co*-(ϵ -caprolactone) hydrogels combining ATRP and ROP for tissue engineering scaffolds³⁸.

During the last century, different transition metal compounds, ligands and solvents

have been investigated extensively in order to optimize the polymerization conditions. It was evidenced that the amount of metal and ligand have an enormous influence on the control over the polymers, mostly through balancing the activation and deactivation equilibrium³⁷. It was proved that both the initiator and ligand structure will lead to different initiation rate and also the polymerization speed will be varied³⁹⁻⁴⁰. Other parameters, such as the polarity of the solvent, will also impact the polymerization process by driving the equilibrium towards one direction⁴¹.

1.1.1.4.3 Reversible Addition-Fragmentation chain Transfer polymerization

RAFT polymerization was initially introduced in 1998 by Moad, Rizzardo and Thang et al¹⁷ as a living radical polymerization technique. The mechanism is shown in Figure 1.7. The system normally requires the addition of initiator, **1**, into the system to generate the first radical species, followed by monomer addition and radical equilibration between growing chain end and the chain transfer agent (CTA) **2**. Similar to NMP, this provides the possibility to tailor polymers by combining with the traditional free radical initiator. Similar to other radical polymerization techniques, the active radical concentration stays constant during the activation-deactivation equilibrium, which was controlled by the CTA **2**⁴². The fast exchange rate between the active species and dormant chain compares to the propagating rate allows the control over the uniformity of polymer chain length.

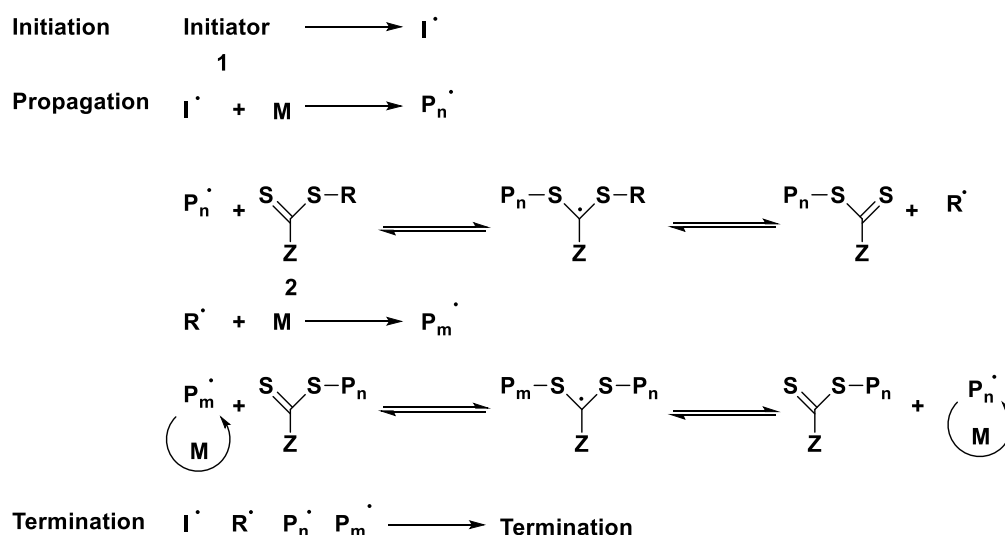


Figure 1.7 General mechanism of RAFT. Initiation step normally involves the formation of radicals from radical source and activation of monomers. Then the propagating process allows the addition of monomers to radical centers, which go through reversible equilibrium mediated by CTA to achieve uniform chain length.

Since the introduction of this technique, RAFT has been adopted to different monomer types⁴³⁻⁴⁵, yielding polymers with chemically diverse structures.⁴⁶⁻⁴⁷ It has also been applied to generate sequence-controlled block copolymers⁴⁸⁻⁴⁹. However, the synthesis of the RAFT agent and the removal of the RAFT agent-derived end group after polymerization limit the applications of this technique.

1.1.1.4.4 Single electron transfer living radical polymerization

Single electron transfer living radical polymerization was first introduced by Percec's group in 2006 using DMSO as the reaction medium¹⁸. The ultrafast reaction rate while obtaining ultrahigh molecular weight polymers with defined structures at room temperature or even lower showed the tremendous advantages of using this technique. It is believed that the main difference of SET-LRP, when compared to ATRP, is the activating species in the equilibrium was changed from Cu(I) halide to more reactive species, Cu(0)¹⁸. The schematic representation of the SET-LRP is shown in Figure 1.8.

Cu(0), **1**, is acting as initiating species to generate the radical species by reacting with the initiator **3** and Cu(II)X₂, **2**, is the deactivating species, which adjust the concentration of radicals within the system. In polar solvents, such as alcohols and DMSO, Cu(I)Br **4** can disproportionate into **1** and **2** in the presence of *N*-containing ligand, which is one of the crucial steps that enables the ultrafast polymerization rate within this system¹⁸. In 2013, Haddleton *et al.* expanded the scope of solvent for this polymerization technique by the most environmentally friendly solvent water. Aqueous systems successfully disproportionate Cu(I)Br in situ, which lead to another increase of reactivity of the Cu(0) powder⁵⁰. The reaction time was further lowered to minutes rather than hours while maintaining the chain-end fidelity. This has also overcome the reactivity issue that acrylamides have in organic SET-LRP and thus, expanded the monomer compatibility. Based thereupon, mixed solvent systems⁵¹ and different copper source⁵² were also applied in SET-LRP, which indicate the robustness of this mechanism. However, the necessity to remove the residual metal catalyst from the system as well as the compatibility of the mechanism with non-polar solvents limit the applications of this technique.

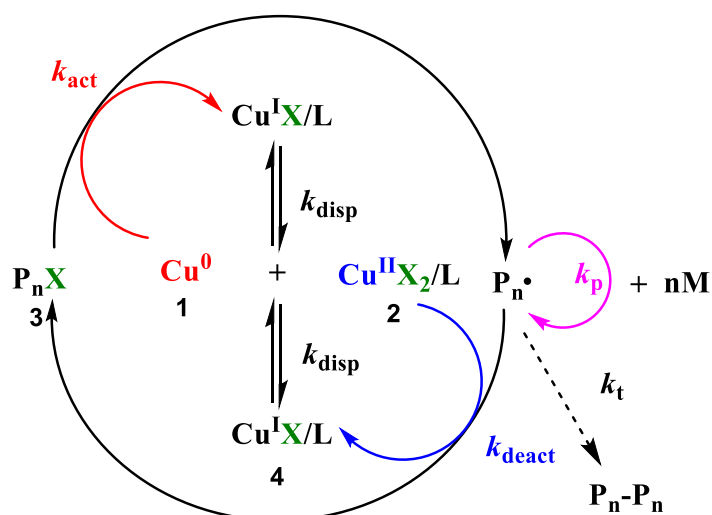


Figure 1.8 General mechanism of SET-LRP. Radical formation involves the single electron transfer from the Cu(0) electron donor to the electron acceptor alkyl halide and active radical concentration was controlled by the redox reaction of higher oxidation state transition metal halide ligand complex.

1.1.2 Post-polymerization modification reactions

The development of living polymerization techniques allowed the synthesis of polymers with precisely controlled molecular weight, polydispersity and compositions¹⁰. However, tolerance of living polymerization towards functional groups are limited while also sometimes the direct polymerization of functional monomers requires the application of a protected monomer and an extra deprotection step⁵³. Thus post-polymerization modification appears as an attractive approach for the synthesis of functional polymers that can overcome the limited tolerance of many controlled polymerization techniques⁵⁴. Hereby, the generated polymer is chemically reacted in order to tailor or tune the respective properties. This bears the advantages range from mild reaction condition, offer quantitative yield and compatible with majority functional groups⁵³. Thiol addition, para-fluorine click reaction and Azide-Alkyne Huisgen Cycloaddition reaction were selected here to introduce the applications of post-polymerization modification in details.

1.1.2.1 Thiol addition

General concepts about reactions between thiol and carbon-carbon double bond were established during early 1900s⁵⁵ with the mechanism revealed in 1938⁵⁶. Thiol addition represents the radical addition of thiol groups to alkene (or alkyne) groups (Figure 1.9). The tolerance over functional groups and application of UV light as a source for radical generation allowed quantitative functionalization of polymer backbones, which is employed to afford glycopolymers⁵⁷, polymer-peptide conjugates⁵⁸ and functional hydrogel⁵⁹.

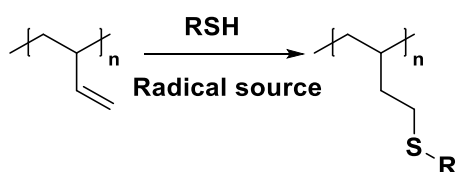


Figure 1.9 Radical thiol addition to poly (1,2-butadiene). Radicals are generated from radical source and then react with a thiol to afford thiyl radical species. Then the reaction propagates via thiyl radicals react with alkyne group to form a carbon center radical and follows by a chain transfer step to abstract the hydrogen from thiol to achieve multiple propagations.

1.1.2.2 Para-fluorine click reaction

The para-fluorine reaction, which utilizes the reaction between fluoro-substituted benzene analogs and nucleophilic compounds, first reported in the 1950s⁶⁰⁻⁶¹ and optimized in early 2000s⁶²⁻⁶³ to reach quantitative yield under mild conditions, is a popular method enabling post-polymerization modification techniques. The reaction relies on the substitution of the activated fluoro in para position by nucleophilic attack of the para-carbon. Wooley and co-workers demonstrated the efficient ligation reaction between fluorinated aromatic groups on polymer chains using hydroxyl group containing compound (Figure 1.10 (a))⁶⁴. Later on, the reaction was extended using both amines (Figure 1.10 (b))⁶⁵ and thiols (Figure 1.10 (c))⁶², leading to a higher degree of

functionalization with quantitative yield. Among all these compounds, thiol-containing compounds were more widely used for post-modification of polymers for para-fluorine click reaction.

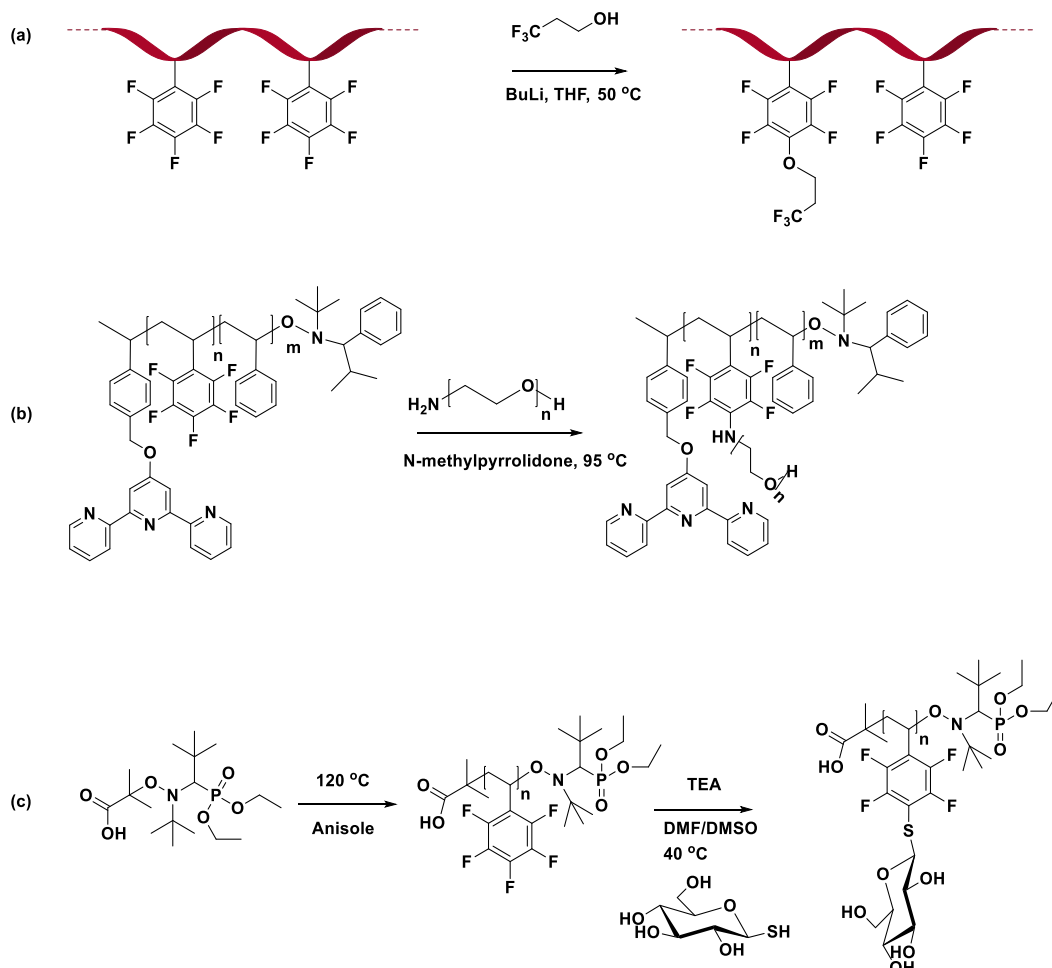


Figure 1.10 Para-fluorine click reaction using (a) hydroxyl, (b) amine and (c) thiol terminated compound.

Base compounds such as trimethylamine (TEA)⁶², 1,8-diazabicyclo[5.4.0]undec-7-ene (DBU)⁶⁶, potassium carbonate (K_2CO_3)⁶⁷ have been used as base during the reaction. The reaction can happen in most polar solvents under mild conditions. The advantages of para-fluorine click reaction are mainly the absence of metal species in the system. By using this post-modification method, glycopolymers^{62, 68}, responsive polymers⁶⁶, as well as polymers with sophisticated structure⁶², can be easily designed

and synthesized.

1.1.2.3 Azide-Alkyne Huisgen Cycloaddition reaction

The Azide-Alkyne Huisgen Cycloaddition reaction was firstly introduced by Rolf Huisgen in 1961⁶⁹ and represent a 1,3-dipolar [3+2] cycloaddition between an azide and a terminal or internal alkynes, manufacturing 1,2,3-triazoles (Figure 1.11). The introduction of copper-based catalytic systems, termed Copper-Catalyzed Azide-Alkyne Cycloaddition (CuAAC) by Sharpless and Meldal in 2001⁷⁰⁻⁷¹ significantly advanced this field, allowing the connection of two molecular building blocks in a facile, selective, high-yielding and mild reaction conditions with no byproducts. The system was further optimized to achieve the reaction without the addition of metal species by Bertozzi and co-workers in 2004⁷². Nowadays, this reaction has been widely employed to synthesize polymer-polymer or polymer-protein conjugates⁷³⁻⁷⁴.

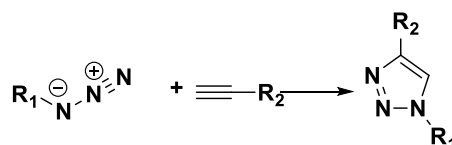


Figure 1.11 General representation of azide-alkyne cycloaddition reaction.

1.1.3 Polymer structure, design and miktoarm polymers

The appearance and the development of synthetic polymer chemistry and post-modification provide the possibility to design functionalized macromolecules and fabricate materials with desired properties. As a result, researches have been focused on the interface of biology, biochemistry and material science, which in turn, promote the progress of synthetic polymers. Numerous polymers with sophisticated structures, for instance, block copolymers, sequence-controlled polymers and miktoarm polymers, have been designed and synthesized. Among different structures, block copolymers

were normally utilized to fabricate nanoparticles⁷⁵⁻⁷⁶ through their self-assembly property, sequence-controlled polymers were extensively employed for information storage⁷⁷ or specific recognition of biomolecules⁷⁸, while miktoarm polymers combine the merits of different polymerization techniques and provide materials with advanced properties, such as targeting and loading properties⁷⁹⁻⁸⁰.

Taking the design of miktoarm polymers as examples, generally, this category of polymers is synthesized uniting different polymerization techniques and click chemistry. Two of the most widely used methodologies are a core-first method and an arm-first method (Figure 1.12)⁷⁹. The arm first methodology involves the synthesis of linear polymer arms first and then followed by linking to a multi-function core (Figure 1.12 (a)). Inversely, the core first method entails the growth of polymer chains directly from a multifunctional core (Figure 1.12 (b)). The main difference lies in the role of the core part, which either performs as a crosslinking point or as an initiator for subsequent polymerization.

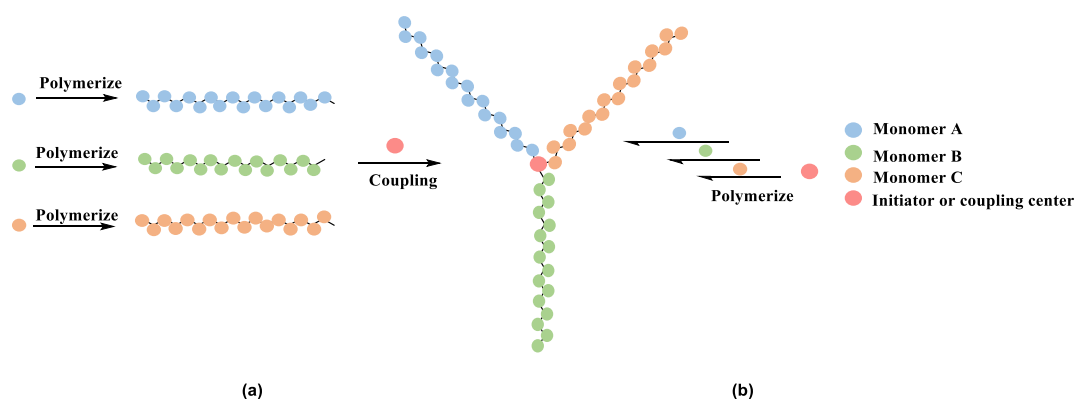


Figure 1.12 Representative process of miktoarm polymer synthesis via the arm-first and core-first methodology. Miktoarm polymers represent a category of polymers with at least two different polymer arms emanated from the same center.

The difference between miktoarm polymers and other polymers like dendrimers or polymer brushes is that all polymer arms are emanated from the same core⁷⁹ and there are at least two different polymer arm types. For instance, ring-opening polymerization

of ϵ -Cl was combined with ATRP, which resulted in mikto arm block copolymers with jellyfish shape⁸¹. A similar approach can be used to incorporate sugar moieties⁶⁸ into a miktoarm polymer that showed advanced properties in biological systems. Liu and coworkers⁸² showed that miktoarm PDMAEMA could provide better stability of the polymer-DNA complex and the transfection efficiency into cells were also improved. In conclusion, miktoarm polymers have shown it advantageous properties over the linear counterpart although the synthesis normally requires more polymerization and purification steps.

One crucial contribution of polymer chemistry is the emergence of new materials ranging from industrial plastic, biological devices to responsive materials. Towards effective translation of polymers into real practical materials, different methods have been established to fabricate well-defined 2D and 3D materials. 2D materials, mostly nanoparticles, can be prepared via various techniques such as solvent evaporation⁸³, nano precipitation⁸⁴, dialysis,⁸⁴ magnetic and emulsion-induced self-assembly⁸⁵⁻⁸⁶. However, due to the limited dimension of these 2D materials, they are mainly applied and restricted to targeting drugs delivery to certain diseases such as cancer. For tissue regeneration and related diseases, which normally involve a reformation of tissue, 3D porous scaffolds were required and could be fabricated using electrospinning⁸⁷, phase separation⁸⁸, self-assembly,⁸⁹ 3D and 4D printing⁹⁰⁻⁹¹. Among those methods, electrospinning is the most widely used approach owing to its simple, straightforward process and the formation of well-organized 3D porous structures⁹².

1.2 Electrospinning

1.2.1 Electrospinning setup and process

Since the invention of electrospinning in 1934 by Formaldas⁹³ this technique has been

widely used for fabrication of 3D scaffolds made up by ultrafine filaments with a defined structure derived from both natural and synthetic compounds. Different from other spinning techniques, the electric force was utilized to elongate compound and obtain fibres in nano or micro range. The classic setup of electrospinning can be found in Figure 1.13⁹⁴. The apparatus requires three main components: high voltage supplier, a tubular connector with small diameter electric conducting end, and a collecting device. During the electrospinning process, a high voltage was applied between the ejector and collector, which induces charge onto the compound solution surface. Increasing the electric field will lead to the rise of the repulsion force caused by the mutual charge. When it reaches the surface tension, the hemispherical solution at the tip will be ejected, elongated and start to form fibre bundles. This point was normally called Taylor cone. Then the discharge of the solution will cause an instability and allow the fibre to elongate into thin and long fibres⁸⁷.

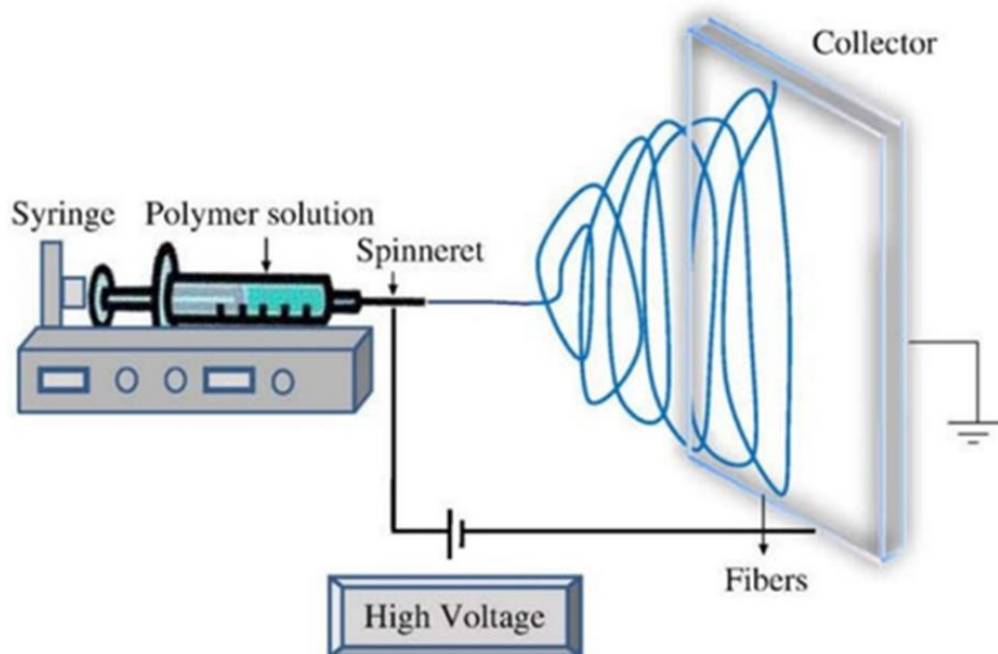


Figure 1.13 Schematic representation of electron spinning setup. The main components of electrospinning including a syringe pump, a high voltage supply, a spinneret and a ground collector.

1.2.2 Electrospinning parameters

Final fibre properties are correlated to the compound solution properties, applied voltage, and influenced significantly by environmental parameters⁹⁵. The fabrication of uniform fibre structure and smooth fibres surface will require regulation of these parameters into a suitable range. Low concentration and molecular weight of polymers will lead to a mixture of fibre and droplet, initiated by the lack of chain-chain entanglement within the solution, while the concentrated polymer solution will prohibit fibres formation, triggered by an inability to process polymer solution⁹⁶. The solvent selection also determines the fibre morphologies through viscosity, conductivity, evaporation speed, the dielectric constant of solvent and extensibility of solution in electric field⁹⁷. For example, Edirisinghe and co-workers elucidated the relationship of the solvents dielectric constant with fibre diameter during the electrospinning of poly(methylsilsesquioxane), which high dielectric constant solvent normally led to thinner fibres⁹⁸. Meanwhile, parameters in electrospinning, like voltage and nozzle collector distance, will also produce fibres with different morphologies and diameters. Similarly, applied voltage and nozzle collector distance mainly influence solvent evaporation, fibre extension and whipping or instability interval during electrospinning⁹⁷. Sufficient voltage (same as shorter nozzle collector distance) should be supplied to generate electric repellent forces that can overcome the forces associated with the surface tension for fibre formation, whilst overload results in oscillation and asymmetry of the Taylor cone, observed by bead formation⁹⁹. Environmental parameters, like temperature and humidity, were also proved to be involved in the determination of final fibre structure¹⁰⁰. During the electrospinning of PCL, porous fibres were formed with the increase in humidity and decrease of temperature¹⁰¹. In conclusion, in order to fabricate uniform fibre structures,

optimization of the conditions needs to be performed for each specific polymer.

1.2.3 Structure control in electrospinning

With the development of electrospinning, more than 50 different compounds, both naturally derived compounds like collagen or chitosan and synthetic polymers with variable properties, were fabricated into 3D membranes¹⁰¹. The easy control over fibre orientation, fibre structure, the wide compound compatibility and the obtained ultrafine fibres dimension all facilitate the applications of electrospun membranes into tissue engineering¹⁰², drug delivery¹⁰³ and related biomedical applications¹⁰⁴.

Aiming at improving the performance of the electrospun systems, manipulation over fibre orientation and structure has been carried out and investigated during the last decades. To exemplify, one of the most widely used methods to obtain aligned fibre orientation was the implementation of high speed rotating fibre collector rather than the stationary counterpart. The fibre orientation can be efficiently controlled into the same direction with a controlled extent (Figure 1.14)¹⁰⁵ and provide distinct biological response compared to random fibre systems. Zhang and co-workers¹⁰⁶ proved that the mechanical properties can be optimized while orientating fibres into the same direction and a difference in cell attachment pattern has also been witnessed. Later on, Xia's group¹⁰⁷ revealed the influence of fibre density, surface coating and supporting substrate on neurites attachment and outgrowth on electrospun films. Results showed cell behavior could be efficiently controlled utilizing electrospinning.

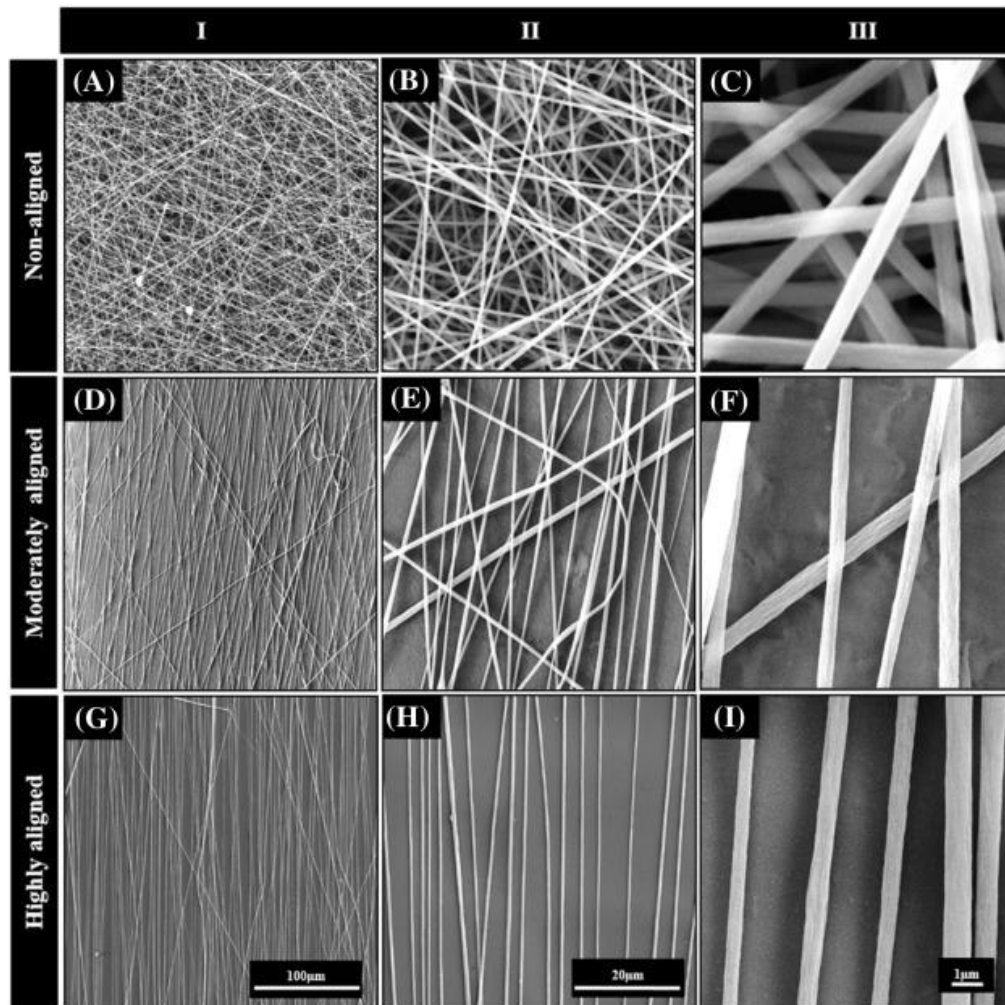


Figure 1.14 Scanning electron micrographs of electrospun PS sub-micron fibres showing morphology at varying magnifications. A–C are non-aligned, D–F are moderately aligned, and G–I are highly aligned sub-micron fibres. The images indicate effective control over fibre alignment can be achieved using electrospinning.

Other than the manipulation over fibre orientation, attributed to the high surface-to-volume ratio, introduced by Kenawy¹⁰⁸ in 2002, this system has shown the potential in drug loading and drug delivery. However, the efficient drug delivery into humans not only requires high loading efficiency and promoted cell interaction with the systems, but also normally a sustained release pattern *in vivo* is preferred¹⁰⁹. Taking advantages of the easy setup of electron spinning apparatus and aiming at the sustained release of drugs from the scaffolds, co-axial electrospinning was invented in 2002 by Loscertales and co-workers¹¹⁰ (Figure 1.15). Using this technique, core-shell fibres

can be easily fabricated with drugs¹¹¹ or proteins¹¹² located at the inner core of the fibre, which led to a sustained release using the protection of the outer layer.

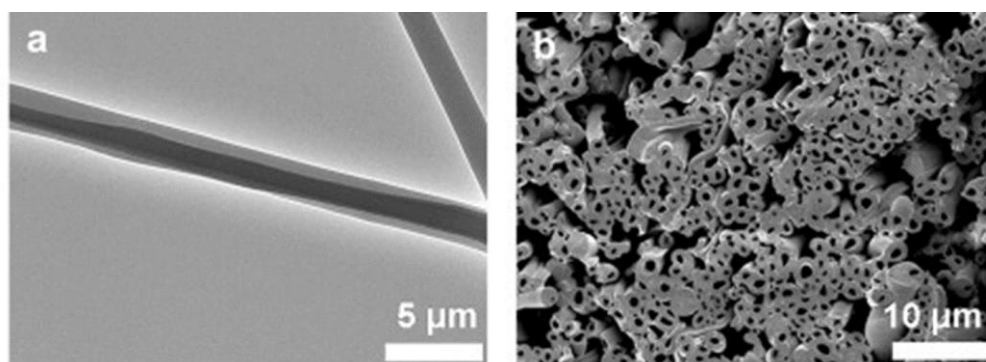


Figure 1.15 (a) TEM and (b) SEM images of the co-axially electrospun fibres. Evident core-shell fibril structure can be observed under electron microscopy and afford fibres with more complicated structure.

1.2.4 Electrospinning applications

The effective control over fibre structure and obtained materials properties precede the applications of electrospinning over other methodologies. Ranging from biomedical devices¹⁰³ to electrochemistry apparatus¹¹³, electrospinning showed its capacities in diverse subjects and research domains. Ramakrishna's group¹¹⁴ created guided a bone regeneration platform using bi-layer PCL/calcium carbonate composite, with sufficient mechanical strength and a promoted proliferation of osteoblast along the surface. Menciloglu and co-workers¹¹⁵ built a super-hydrophobic surface via electrospinning, with a finely tuned microscale texture, using poly(acrylonitrile-*c*- α , α -dimethyl meta-isopropenylbenzyl isocyanate) (poly (AN-*co*-TMI)). More recently, Cui's research group¹¹⁶ even utilized electrospinning to generate filter membrane for air pollution, which shows the versatility of this methods. In summary, the straightforward process to obtain ultrafine fibres, with high surface-volume ratio and comparable dimensions to native tissue, offers electrospun materials exceptional properties among the broad landscape of materials fabrication methodologies.

However, there are still some challenges remaining in this field. For example, the requirement of high voltage during the process, the sensitivity of fibre properties towards environmental parameters and most importantly, it can only be applied with the existence of high chain entanglement in order to produce continuous spinout jet¹¹⁷⁻¹¹⁸.

1.3 Tendon structure and function

Tendons facilitate the motion of muscles and normally connect while transferring the strain from muscles to the bone, thus allowing muscles to withstand higher stress. Consequently, tendons are constantly used cyclically in our daily movements. The hierarchal structure of tendon tissue derived from their specialized cell environment permits tendons to work under high strength for a long time.

Tendons are comprised of collagen, cells, proteoglycans and water, with collagen contributes more than 60% of dry weight in a tendon tissue¹¹⁹. Collagen type I, which accounts for more than 95% of collagen in normal human tendons¹²⁰, possess great flexibility and durability¹²¹. Aggregation of a triple helix of three polypeptide chains leads to the formation of collagen molecules. Subsequently, collagen molecules pack closely via chemical crosslink into fibre bundles¹²². This hierarchal structure of tendon is envisioned in Figure 1.16¹¹⁹, which leads to the complex response towards loading.

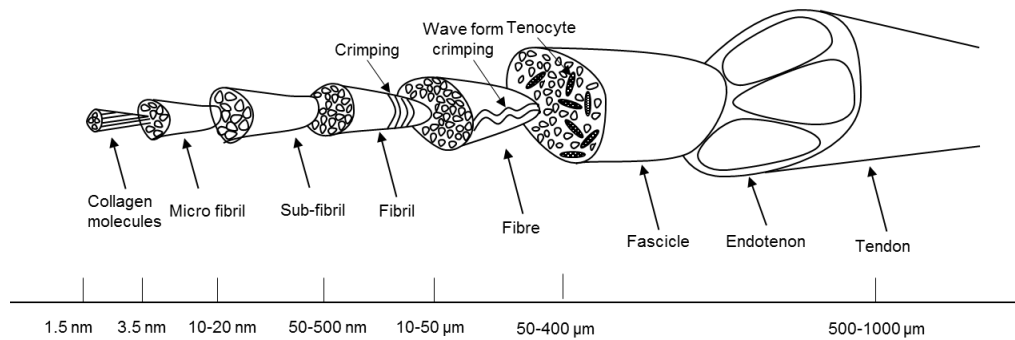


Figure 1.16 Scheme representation of the hierarchal structure of tendon. The hierarchal structure of tendon accounts for the unique mechanical responses and function of tendons.

Most of the collagen fibres bundles in normal tendon tissue are well arranged along the long axis of the tendon¹²³ (Figure 1.17), allowing the efficient transmission of high force. There are also crimp on relaxed tendon structure derived from elastin in tendon tissue, which allows tendon possess some extent of elasticity¹²⁴.

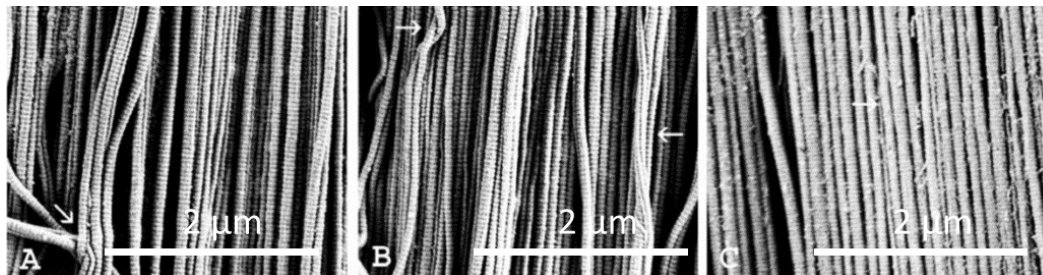


Figure 1.17 Collagen fibril organization and morphology in mature rat tendon and ligament, white arrow indicate the existence of crimp on tendon tissue. From the images, it can be observed that in mature tendon tissue, collagen fibres are primarily aligned along the longitude of the tendon with crimps existing along the fibres (white arrow).

Figure 1.18 shows a typical stress-strain curve of normal tendon upon load is applied. Crimp in tendon leads to a toe-region up to 2 % strain until reach smooth state and it varies from tendon types, the age of tendon and tendon locations¹²⁵. Tendon mechanics follow a linear region after the removal of all the crimp, during which involves the extension of collagen fibres¹²⁶, sliding between fibres¹²⁷ and fascicles¹²⁸ until reaches

the limit of tendon extensibility, which results in microscopic failure following by rupture of the tendon.

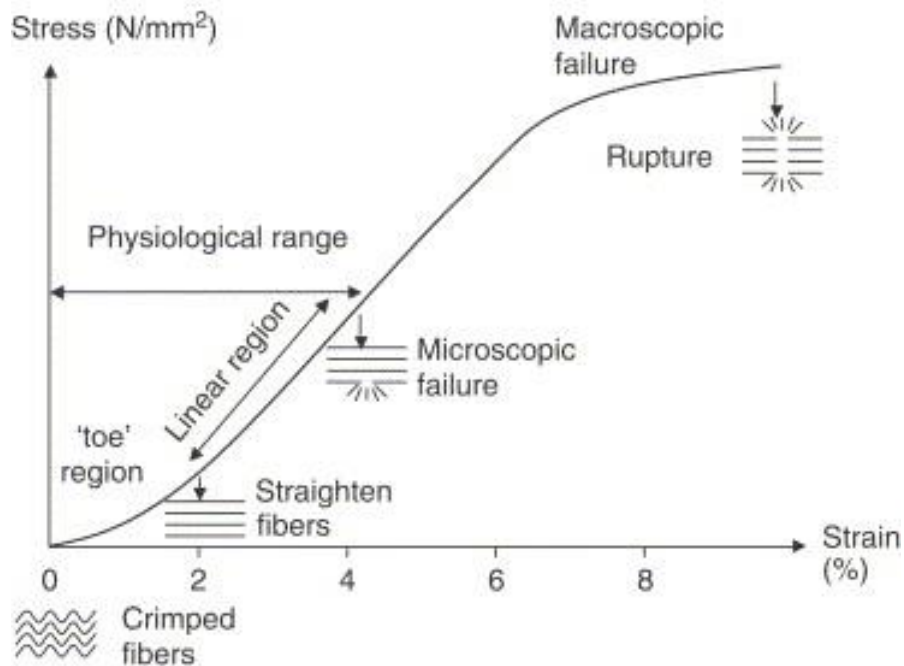


Figure 1.18 Typical normal tendon stress-strain curve. This figure shows the mechanics of normal tendon tissue. The crimp on tendon tissue leads to the toe region of the curve and followed by the elastic mechanical behaviour until the physiological limit of tendon tissue. Further extension will lead to the appearance of microscopic failure and lastly, the rupture of tendon tissue, termed here as macroscopic failure.

Tendon mechanic mainly depends on the collagen fibres which is mediated by the cells function. As the main cell line within the tendon, tenocytes control the tendon performance by adjusting collagen synthesis, and protein secretion¹²⁹. Meanwhile, the tendon is normally surrounded by a synovial sheath (Figure 1.19), which prevents the adhesion of tendon¹³⁰ and allows tendon gliding freely against surrounding tissue¹³¹.

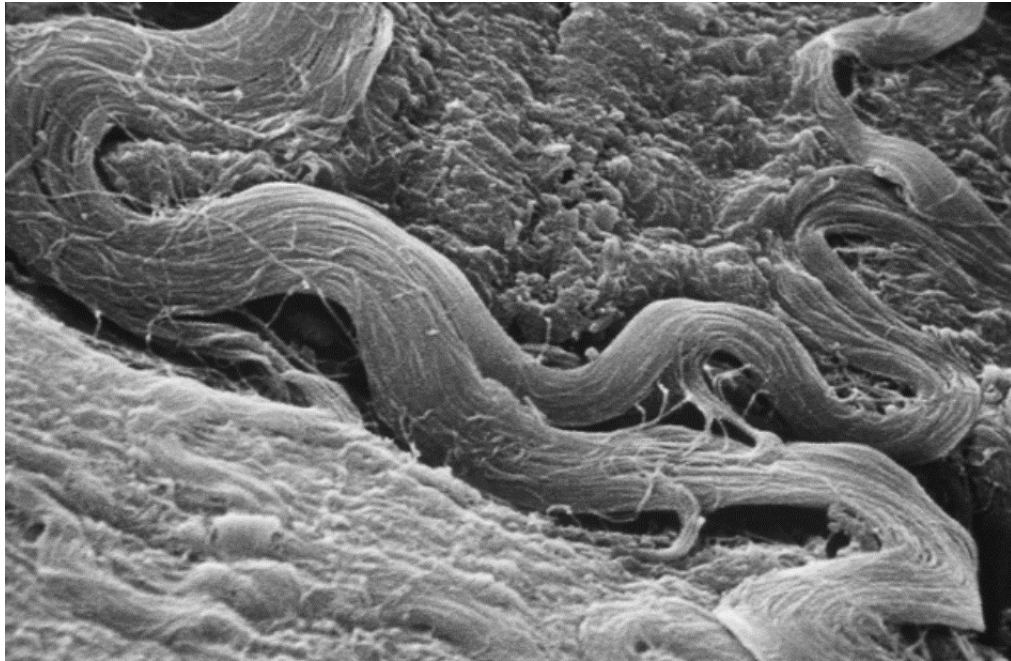


Figure 1.19 SEM of rat Achilles tendon sheath. Different from the fibre arrangement in tendon tissue, tendon sheath appears to be a randomly fibril connecting tissue which helps the gliding of tendon against other tissue.

Although tendons are one of the well-organized tissues in the human body, complications in tendon injuries make the healing of tendon remains one of the biggest challenges across the world.

1.3.1 Tendon injuries

Tendon injuries can be categorized into acute or chronic injuries according to the initiation of the injuries¹³². Acute tendon injuries are normally derived from either penetrating or laceration by sharps¹³³. These normally lead to partially or completely rupture of tendon followed by a tedious healing process. However, chronic tendon injuries are normally caused by repetitive tendon loads¹³⁴, overuse, or aging of tendon¹³⁵. It has been proved that tendons degenerate by increase age¹³⁶ which leads to altered responses towards mechanical stimulation¹³⁷ As the population and life expectancy is increasing steadily, it is estimated that 25% of adults will suffer from

tendon related problems, putting a further pressure on healthcare system¹³⁸.

As the major cause for tendon related injuries, tendon laceration possesses the highest incidence among 20–29 years population and a higher possibility in males than females¹³⁹. It normally refers to a deep cut which leads to partial or complete tear of connective tendon tissue with discontinuity and disorganization of collagen fibrous bundles in biological view (Figure 1.20)¹⁴⁰. Inflammatory cells were observed to migrate to the injured place and compared with normal tendon (top column), disorganized fibres were deposited during the tendon healing process after it gets injured at day 9 (Figure 1.20). Meanwhile, as mentioned before, tendons are surrounded by tendon sheath, a membrane-like structure. However, in tendon injuries like laceration, the integration of the tendon sheath is frequently damaged, which potentially leads to several further problems with further implication in restricting the functionality and movement of tendon observed by a reduction in tendon performance¹⁴¹.

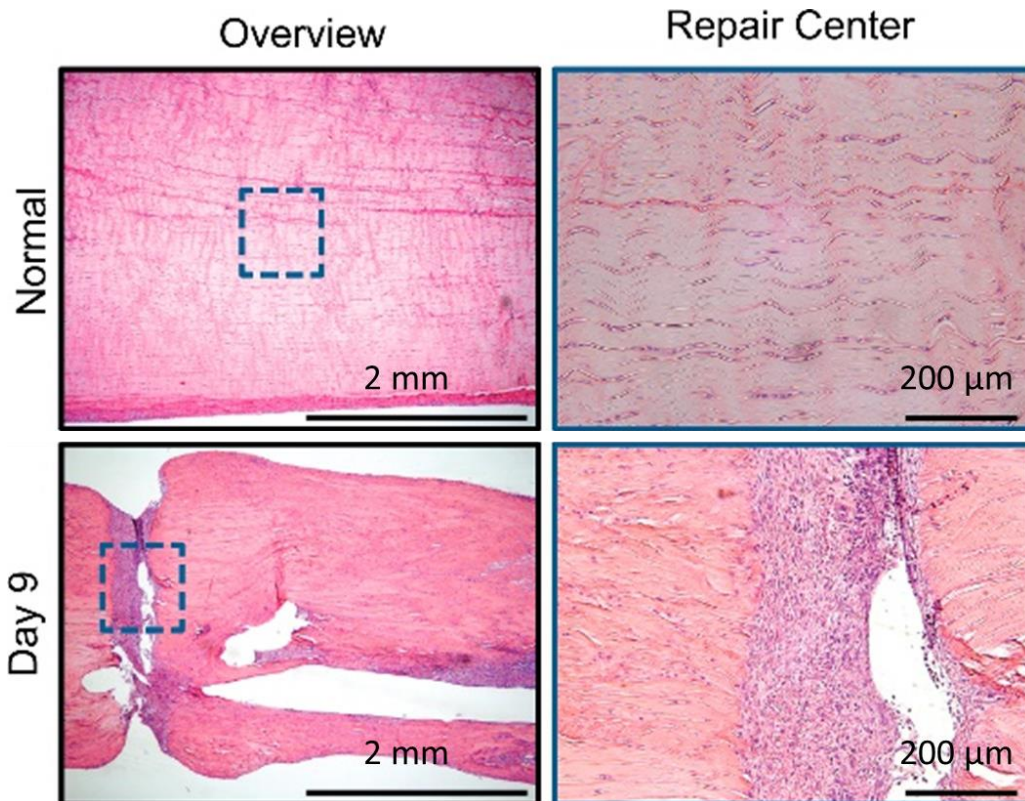


Figure 1.20 Representative histologic sections of healthy and repaired canine flexor tendons at 9 days postoperatively. The sections were stained with Hematoxylin and eosin stain (H&E) and viewed under bright field for cell identification. The upper row shows the aligned fibre structure and arranged cell orientation in normal tendon tissue while the bottom row shows the disorganized fibre bundles and cell orientation.

Normally, clinic strategies for tendon healing involve surgery, followed by rehabilitation exercises which could last for years until tendon fully healed¹⁴². The detailed tendon healing mechanism and existing challenges will be discussed in the next section.

1.3.2 Tendon healing mechanism and challenges

Due to the importance of tendons, tendon injuries have gained numerous attention. There are mainly two mechanisms for tendon healing: intrinsic and extrinsic healing, based on the cell populations involved in the healing process¹⁴³. Intrinsic healing refers to tendon healing whereby only tenocytes, fibroblasts and inflammatory cells within

the tendon and epitenon invade the healing site and fulfill the healing process (Figure 1.21 (A))¹⁴⁴, which formed connected tissue within the injured tendon. Tenocytes from epitenon were normally stimulated by nourishments diffused from the synovial fluid¹⁴⁵ and then initiate the healing process through proliferation and migration¹³⁰. Instead, extrinsic healing requires invasion of cells from the surrounding sheath and synovium, which generally formed scar-like tissue to help with the healing process (Figure 1.21 (B))¹⁴³. Clinic results showed that tenocytes from epitenon synthesized larger and more mature collagen fibres¹⁴⁶ and could lead to scar-free healing¹⁴⁵, which represents better biomechanical properties of the healed tendon by intrinsic healing only. However, real tendon healing normally involves both mechanisms due to the sophisticated responsive triggering systems of human bodies¹⁴⁷.

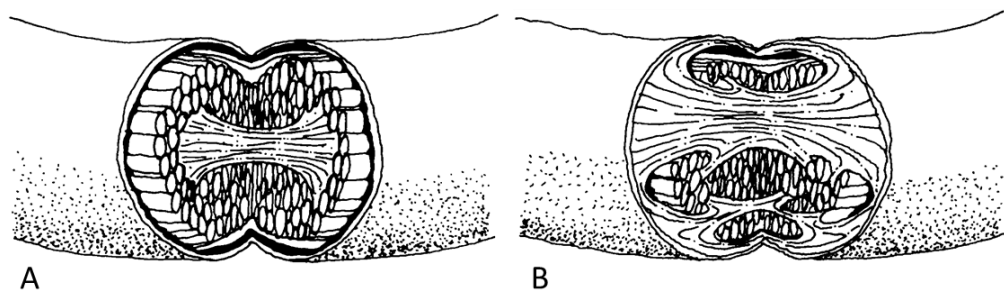


Figure 1.21 Schematic representation of (A) intrinsic and (B) extrinsic pathways of tendon healing. The intrinsic healing only involves the cells within tendons and the formation of connecting tissue was mostly located within tendons. In contrast, extrinsic healing leads to the formation of connecting tissue surrounding tendon, which subsequently leads to scar and adhesion formation.

Regardless of the difference in tendon healing mechanisms, tendon repair normally involves three overlapping stages: the inflammatory stage, the proliferative stage and the remodeling stage (Figure 1.22)². The inflammatory stage normally starts straight after the injury and witnessed by clot formation, inflammatory responses and initiation of cellular migration². This stage provides injured tendons with initial migration of cells from the surrounding tissue and various chemotactic factors expressed to help

the reconstruction of tendon tissue (Figure 1.22(A)). After three weeks, Proliferative stages will observe by the proliferation of cells with the appearance of synthetic collagen bundles and further secretion of growth factors. The collagen fibres synthesized during this stage are mainly collagen type III in a disorganized and immature manner (Figure 1.22 (B))¹⁴⁸. Lastly, the remodeling stage will happen in 6-7 weeks after injuries and during which, mainly collagen I will be synthesized. Meanwhile, collagen fibres bundles will start to reorganize along the axis of the tendon, while reform crosslinked interaction between fascicles (Figure 1.22 (C)). This normally provides the tendon with better strength and the whole process could last for years¹⁴⁹⁻¹⁵⁰.

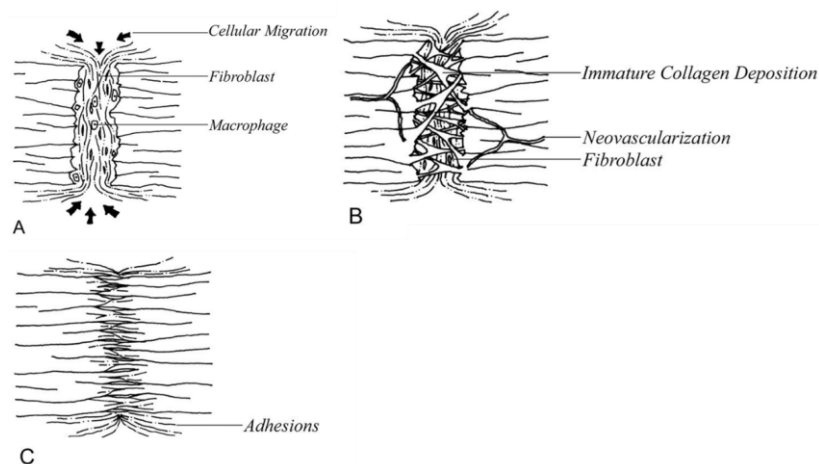


Figure 1.22 Cellular phases of tendon healing. A: Inflammatory stage; B: Proliferative stage; C: Remodelling stage. Images show the three main stages during tendon healing. Inflammatory stage involves the inflammation reaction of human body and the initial migration of cells to the injured place; during migration stage, cells continue to proliferate and start to deposit disorganized immature collagen fibres; the remodelling stage is in charge of the reorganization and maturation of fibre bundles.

Although the tendon healing process has been understood for years, unfortunately, up to now tendon repair still faces some challenges. Firstly, tendon injuries normally involve disruption of nutrition system. Poor blood supply, the release of synovial fluid and decrease of pressure are normally witnessed after breakage of tendon sheath,

which all lead to starve of cells within the injured place and slow down the healing process¹⁴⁷. Especially for flexor tendon healing, surgical trauma, like sutures between two ends, was normally required to promote the healing process. The intervention of surgical operation will further interfere with the nutrition system. Meanwhile, followed by surgical treatment, a fixation apparatus will normally be applied to prohibit load over the injury place, but it also comes with an increase in tendon stiffness, scar formation and tendon adhesion formation¹⁴⁷.

The tendon adhesion formation was first introduced in the 1920s by Bunneel¹⁵¹ and Garlock¹⁵². It is normally caused by the disruption of the synovial sheath (Figure 1.23 (A)) and invasion of cells afterwards (Figure 1.23 (B))¹⁵³ which result in swelling and adherence of tendons with surrounding tissue (Figure 1.23 (C)). Subsequently, connective tissue will form between the injured tendon and peritendinous tissue (Figure 1.23 (D)), normally termed tendon adhesion. Tendon adhesion will restrict the gliding properties of healed tendon and it requires secondary surgeries to be separated, which is essential for promoting the range of motion of healed tendons. In order to minimize tendon adhesion formation and allow the restoration of tendon gliding ability, different methods have been introduced.

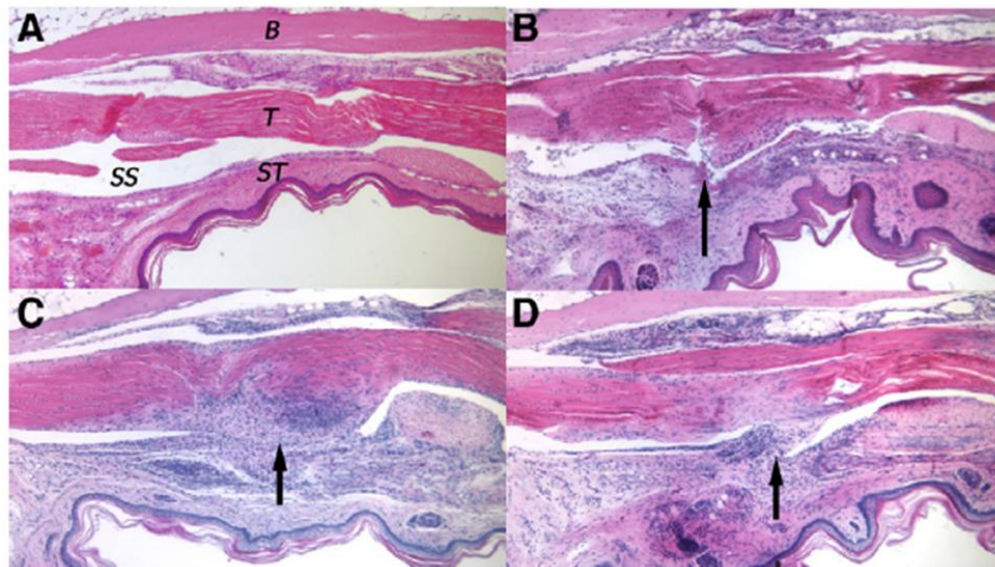


Figure 1.23 Basic histology of adhesion development in mouse flexor tendon. T: tendon, ST: subcutaneous tissue, SS: sheath space, and B: bone. From image A, it can be observed there is a clear space between tendon and bone as well as tendon and subcutaneous tissue. Image B shows the invasion of cells into the injured place (black arrow). Image C shows the swelling of tendon and adherence with subcutaneous tissue (black arrow). Image D indicate the formation of adhesion after tendon healed (black arrow).

1.3.2.1 Treatment to tendon adhesion prevention

The methods used for tendon adhesion prevention mainly focused in three fields: surgical techniques, chemical agents, and physical barriers¹⁵⁴.

One method to help reducing tendon adhesion is controlled early mobilisation⁵. However, the risk of re-rupture and poor strength during the early stage requires a long time immobilization. Thus surgical techniques employing non-absorbable sutures were applied to bridge the gap of the ruptured tendon to enable enough mechanical property during the early stage of tendon healing¹⁵⁵. To date, numerous suture techniques have been developed for tendon repair, for example, Bunnell, Mason-Allen and modified Kessler, which are all widely used suture methodologies¹⁵⁶ Figure 1.24 shows some of the suture methods that are widely utilized in the clinic. According to the number of suture strings, the methods can be categorized into a single string,

double string or multiple string methods. A suture has been estimated to withstand up to 20 N using a single strain method, or 70 N using a 6 string method¹⁵⁷⁻¹⁵⁸. However, it is proved suture techniques have a significant influence on the amount and extent of adhesion formation¹⁵⁹. Increase in the number of sutures will provide injured tendon with better mechanical properties during the early healing stage whilst also causes more damage to the site, introduces more external foreign materials and leads to higher tendon volume, subsequently result in severely adhesion formation¹⁵⁹⁻¹⁶¹. After the tendon healed with adhesions, they normally require secondary surgeries to be separated, which is essential for promoting the range of motion of healed tendons.

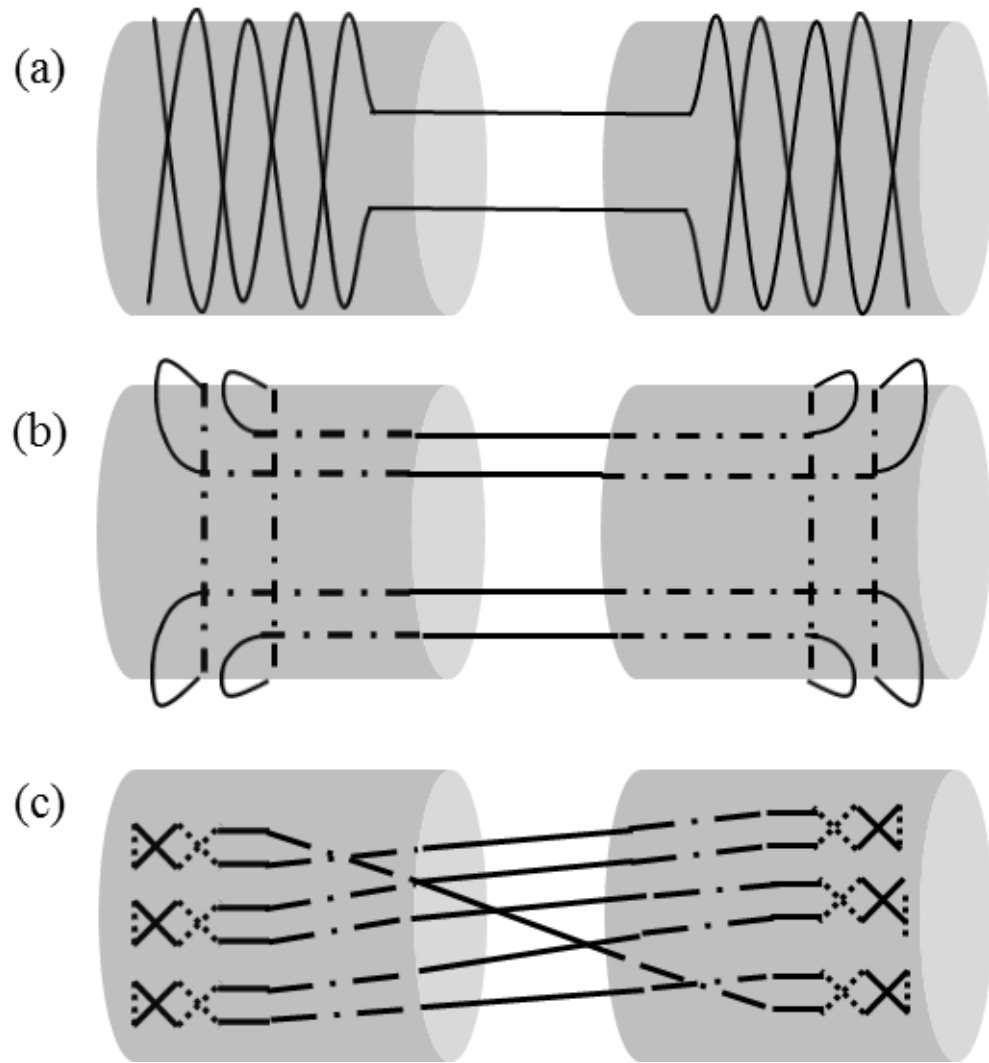


Figure 1.24 Examples of tendon suture techniques; (a) Bunnell method; (b) Double modified Kessler method; (c) Savage method. Image a, b and c correspond to a two strand, four strand and six strand suture method, respectively.

Another method of tendon adhesion prevention is using chemical agents. The inflammatory reaction of the body has been reckoned as the main reason for adhesion formation¹⁶². Based on this theory, several anti-inflammatory molecules like slow-acting antirheumatic drugs (SAARDs) or non-steroidal anti-inflammatory drugs (NSAIDs) are extensively used in tendon repair to prohibit or relieve inflammatory reaction, subsequently decreasing the number of cells participating in the tendon healing process and finally reducing the amount of collagen that is produced by cells¹⁶³.

However, the side effects of these drugs and the fast degradation rate restrict the applications of pharmaceutical agents. Later on, other biological cues involved in tendon healing, such as vascular endothelial growth factor (VEGF),¹⁶⁴ platelet-derived growth factor (PDGF),¹⁶⁵ basic fibroblast growth factor (bFGF)¹⁶⁶ and transforming growth factor- β (TGF- β)⁴, were widely studied to prevent adhesion. Among the growth factors family, TGF- β is the most well-researched molecule due to the close relationship with the synthesis of collagen molecules¹⁶⁷. The suppression of TGF- β 1 has shown significantly lower tendon adhesion following a dose-dependent manner¹⁶⁸. However, since the complicated effects of growth factors on tendon healing and the controversial results¹⁶⁹⁻¹⁷⁰, the applications of growth factors are not commercialized yet.

A physical barrier is another alternate method by using biocompatible membranes to mimic the properties of a natural tendon sheath, which hinder or block the invasion of surrounding cells to injured tendon. In theory, extrinsic healing is mostly accounting for the adhesion formation because it requires the invasion of numerous cells³. Due to the excellent biocompatibility, naturally derived materials such as hyaluronic acid (HA)¹⁷¹ and oxidized cellulose (CEL)¹⁷² based materials were firstly tested for tendon adhesion prevention. The sodium hyaluronate–carboxymethylcellulose (HA–CMC) barrier (Septrafilm[®]) is one of the commercial representative materials for tendon adhesion prevention⁷. The applications of Septrafilm resulted in much better adhesion prevention evident by a gap between the tendon and surrounding tissue (Figure 1.25 (A)) compared with extensive connective tissue witnessed in the controlled group (Figure 1.25 (B)).

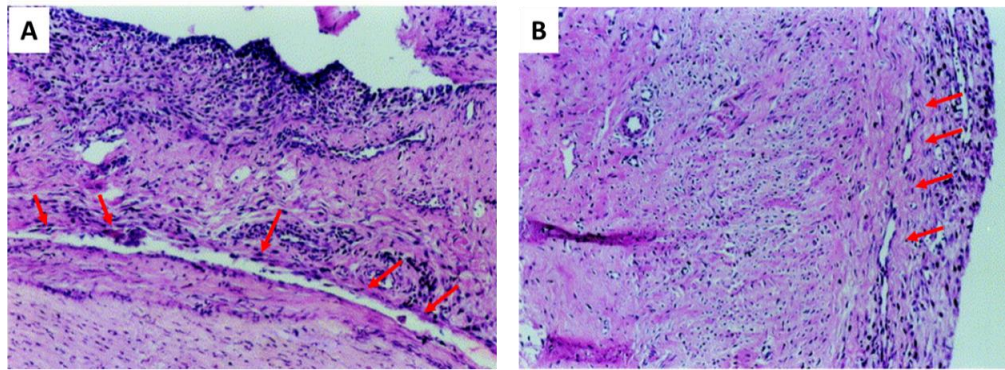


Figure 1.25 Histology staining of Adhesion prevention combine (A) tenolysis and Sperafilm®; (B) Non treated group. Image A shows the sheath space formed after tendon healed and proved the efficiency in prevention of tendon adhesion compared with significant less sheath space in Image B, which has no treatment during the healing. Red arrow shows the sheath space formed during tendon healing.

With the development of polymer synthesis and functionalization, synthetic polymers have gained increasing research interests for biomedical applications⁶. Among the biocompatible polymers, polyesters are most widely researched and used. For instance, poly(lactic acid) (PLA)¹⁷³, poly(glycolic acid) (PGA)¹⁷⁴, poly(ϵ -caprolactone) (PCL)¹⁷⁵ and their copolymers¹⁷⁶ have been used extensively in the clinic applications such as surgery sutures,¹⁷⁷ fixation devices¹⁷⁸ and tissue scaffolds¹⁷⁹⁻¹⁸⁰ for a long history. Not only because of their great biocompatibility and biodegradability, but also because these polymers are some of the few synthetic polymers which were approved by the U.S. FDA for human clinical applications.

More specifically, there are already biodegradable polymers which can be used in the prevention of tendon adhesion formation such as DegraPol®¹⁸¹ chitosan-grafted poly(ϵ -caprolactone) (PCL-g-CS) nanofibrous membrane (NFM)¹⁸², and some anti-adhesive agent containing membranes¹⁸³. DegraPol® is made up of poly-hydroxybutyrate as a crystalline segment and ϵ -caprolactone as the soft segment⁸. Membranes were fabricated via electrospinning and the adhesion prevention property of this materials was tested on female New Zealand white rabbits model with reduced

adhesion formation in the experimental group¹⁸¹. It was further modified by Buschmann¹⁸¹ by changing the ratio of the block copolymer to optimal anti-adhesive properties as well as lower the inflammation reaction.

The appearance of physical barrier system also allows the combination with chemical compound therapies. One example is using ibuprofen-loaded poly(lactic acid)-poly(ethylene glycol) (PELA) copolymer based fibrous membranes to prevent the adhesion formation of tendon¹⁸⁴. The fibrous membrane was made by ibuprofen-loaded PELA fibres via co-axial electrospinning. Results showed a sustained release of ibuprofen, which lowers the inflammatory reaction, while maintains the anti-adhesive properties (Figure 1.26 (C)) compared with control group (Figure 1.26 (A)) as well as PELA only group (Figure 1.26 (B)). However, due to the release of ibuprofen, the tendon healing process was significantly suppressed and as a result, the strength of the repaired tendon was significantly lower than the control group. Although there are already some commercial products for tendon adhesion prevention like Sefrafilm[®] and DegraPol[®], the results of these products are not ideal when comes to the mechanical properties of healed tendon.

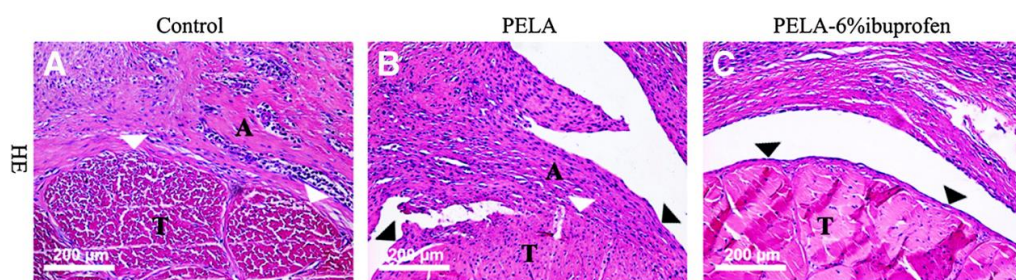


Figure 1.26 Histology staining of (A) Control group; (B) PELA membranes; (C) 6% Ibuprofen PELG membranes. White arrow shows the adhesion tissue formed surrounding tendon while black arrow shows the sheath space. T stands for tendon tissue while A stands for adhesion tissue. It can be observed that there are several adhesion tissue from in control group (Image A). While some adhesion formed in the PELA treated group (Image B) and no adhesion formed in ibuprofen loaded PELA group (Image C).

1.4 Aims and objectives

To date, numerous biodegradable polymers have been assessed for the efficiency of tendon repair with various experimental or clinic results. However, considering the healed results of tendon and developments of polymer chemistry, more contribution still needs to be devoted to accomplishing better healing results. PCL showed great potential in the prevention of tendon adhesion, not only derived from the hydrophobic characteristic of PCL backbone which affords PCL cell repellent properties, but also a relatively slower degradation rate which can be adjusted to cover whole tendon healing process. However, it is crucially important that such a scaffold can also provide appropriate cellular cues, which requires the incorporation of bio-active polymers, to activate cell behavior and achieve optimal healing mechanics. Moreover, to fulfill a further improvement upon recent systems, membranes that encourage the recapitulation of native tissue behavior should be fabricated by orientating fibres, which should come along with additional mechanical strength and guidance to cell attachment.

Figure 1.27 shows the schematic representation of the final aiming bilayer membranes for this project. It mainly constitutes by two different layers with different purposes. The outer layer will be made up by hydrophobic polymers which allow the repellent of proteins and cells to achieve the anti-adhesive purpose. However, the inner layer will incorporate glycopolymers with pendant glucose moieties to provide biological cues for cell attachment. Meanwhile, aligned fibres will be designed within the inner layer to potentially facilitate the creation of normal tendon physiological structure and guidance over cell attaching pattern.

In brief, not only an ideal platform for tendon healing, but a general substrate for tissue engineering and other related biomedical applications will be obtained at the end of

the project.

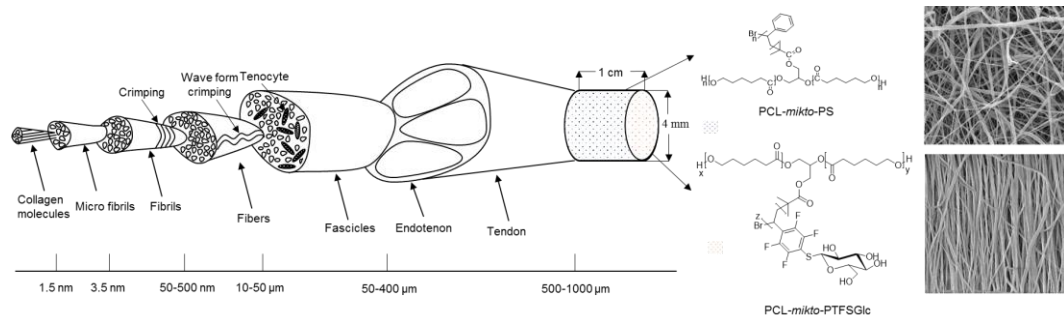


Figure 1.27 Schematic representation of bilayer biocompatible copolymers membrane for tendon adhesion prevention and tendon repair promotion. The outer hydrophobic layer will behave as an anti-adhesive layer while the inner glycopolymer-based layer will allow cell attachment and provide biological cues through the incorporation of sugar moieties.

Chapter 2. Polymer synthesis

2.1 Introduction

2.1.1 Synthetic biocompatible polymers

As the main component of cell matrix, collagen has been used directly to fabricate scaffolds¹⁸⁵⁻¹⁸⁶. However, whilst cell attachment is excellent in collagen scaffolds, their poor structural stability limits their practical application¹⁸⁷. Previous studies have also shown that by aligning fibres in naturally derived materials such as cellulose¹⁸⁸⁻¹⁸⁹ or chitosan¹⁹⁰ based materials, cell adhesion and alignment can be controlled to recapitulate the direction of fibre alignment, whilst providing structural stability also. However, the high stiffness and low flexibility of these materials have limited their adoption for biomedical applications. Fortunately, with the development of polymer chemistry, numerous researches have been focused on the fabrication of polymers that display compatibility within living organisms and shows the potential to be used in biomedical applications such as tissue engineering¹⁹¹⁻¹⁹². Generally, these are termed as synthetic biocompatible polymers and are made to replace or substitute naturally derived (macro) molecules. Synthetic biocompatible polymers range from polyesters, polyamides, poly (amino acids), polystyrene derivatives to the relatively new field of glycopolymers, that only started to emerge in the last two decades¹⁹³.

2.1.1.1 Polyesters

Among all synthetic biocompatible polymers, polyesters are the most widely investigated and used family, which typifies a category of polymers that possess ester linkage along the backbone. Taking as examples, poly(lactic acid) (PLA)¹⁷³, poly(glycolic acid) (PGA)¹⁷⁴, poly(ϵ -caprolactone) (PCL)¹⁷⁵ and their copolymers¹⁷⁶ have been used in clinic applications, such as surgical sutures,¹⁷⁷ fixation device¹⁷⁸ and

tissue scaffolds¹⁷⁹⁻¹⁸⁰. The numerous applications benefit not only from their great biocompatibility and biodegradability, but also these polymers are some of the few synthetic polymers, which were approved by the U.S. Food and Drug Administration (FDA) for human clinical applications.

Relative to other polyesters, due to the better reactivity, crystallization ability, relatively long degradation time and mechanical stability,¹⁷⁵ PCL shows the potential to be used for long-term tissue regeneration platforms²². For example, Zhang *et al.*¹⁹⁴ utilized drug-loaded PCL/gelatin membranes in wound healing, prevention of postsurgical adhesions for up to 8 months. The membranes maintained the mechanical properties with gradual degradation and anti-bacterial properties achieved by sustained drug release. Moreover, MacLellan and co-workers¹⁹⁵ also blended PCL with ECM components like elastin, collagen and gelatin for cardiovascular regeneration. It was observed that PCL possessed broad miscibility with all other compounds and formed fibres with smooth, uniform morphology. Furthermore, the introduction of PCL into this scaffold significantly increased the mechanical stability of the platform and obviating the need for further cross-linking. Consequently, PCL proved the appropriateness to be applied in tissue regeneration and has achieved tremendous success¹⁹⁶⁻¹⁹⁷ in biomedical fields.

2.1.1.2 Polystyrene derivatives

Since the first introduction in 1839 by Eduard Simon¹⁹⁸, polystyrene and its derivatives were used in plastic industry¹⁹⁹ as well as biomedical materials, such as tissue culture Petri dishes²⁰⁰. The mechanical properties, processability durability and biocompatibility all benefit the application of polystyrene derivatives in commercial

products such as tissue culture plate²⁰¹. Nowadays, polystyrene is mostly synthesized via conventional polymerization and obtained polymers are post-processed into materials with different shapes by taking advantage of the low glass transition temperature of polystyrene²⁰².

The limitations of polystyrene derived materials include the hydrophobicity and low surface energy of the material which restrict the attachment and proliferation of cells²⁰³. Researches have utilized surface plasma²⁰⁴, chemical vapor deposition²⁰⁵, ultraviolet (UV)²⁰⁵ and other surface treatments²⁰⁶⁻²⁰⁷ to address these problems. For example, Busscher and coworkers²⁰⁴ employed a glow discharge treatment to modify polystyrene surface with oxygen incorporation. Cell adhesion studies confirmed cell adhesion, which is proportional to oxygen percentage and hydrophilicity (Figure 2.1). As discussed before, the polyester family has been widely used in biomedical applications for a long-term and possesses decent biocompatibility *in vivo*. Based on this background, we combined PCL with PS to fabricate miktoarm block copolymers for the anti-adhesive purpose.

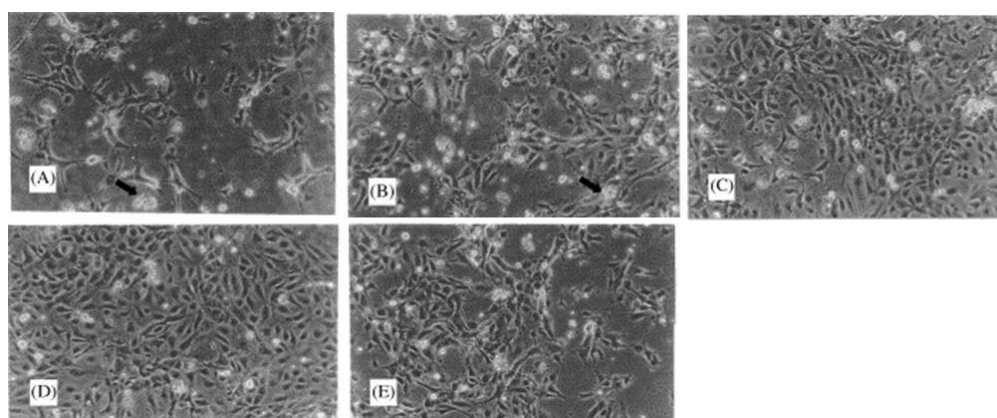


Figure 2.1 Phase-contrast light microscopic images of adhering cell populations on PS treated with glow discharge for (A) 5 s; (B) 10 s; (C) 30 s; (D) 60 s and (E) TCPS; Cells were incubated for 48 h. Notable higher number of cells were observed on PS treated with longer glow discharge which has higher oxygen content.

2.1.1.3 Glycopolymers

Glycopolymers represent both natural and synthetic polymers with carbohydrate units²⁰⁸. In this section, glycopolymers will be discussed in depth with mainly focusing on synthetic glycopolymers and their respective applications. Glycopolymers are mainly synthesized either via glycomonomer approach²⁰⁹ or post-modification approach¹⁸⁰. In the last couple of decades, they have obtained increasing attention, which is attributable to the abundant existence and importance of polymeric carbohydrates in living organisms²¹⁰⁻²¹¹.

Indeed, the discovery and investigation of multivalent interactions of carbohydrate units and human lectins²¹²⁻²¹³, have boosted the field of glycopolymers drastically and resulted in platforms for specific cell isolation from a heterogeneous population²¹⁴⁻²¹⁵ and enzyme delivery purpose²¹⁶.

Lectins signify a category of proteins with carbohydrate-binding domains²¹⁷. Lectins carbohydrate interactions are significantly enhanced due to the multivalence of repeating sugar moieties along glycopolymers, which is termed as *glycocluster effect*²¹⁸. The strong and specific interaction between glycopolymers and lectins was reported by Haddleton *et al.*²¹² and Becer *et al.*²¹³, describing that the specific interaction between mannose and DC-SIGN could efficiently inhibit the binding of HIV envelop protein, gp120 to DC-SIGN at nanomolar concentrations (Figure 2.2).

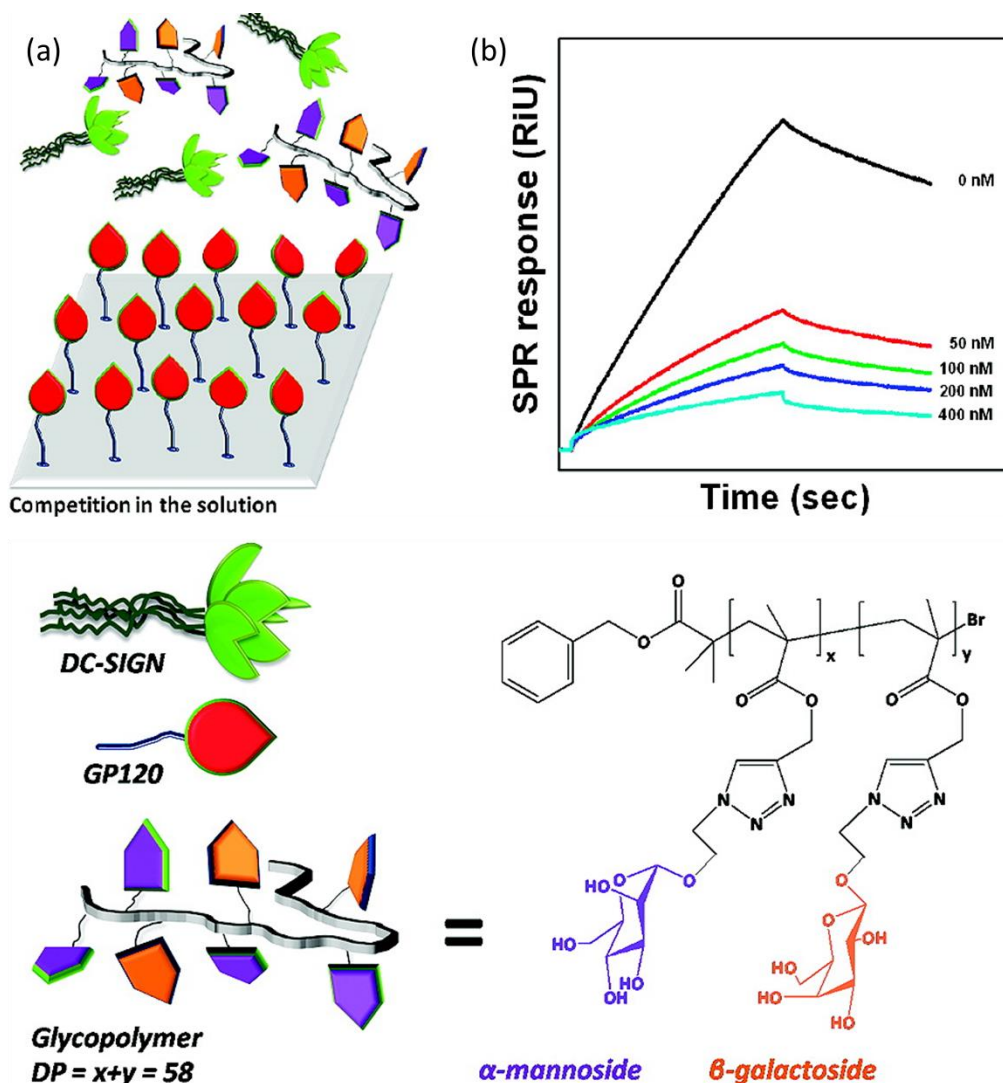


Figure 2.2 (a) Experimental design of gp120 functionalized surface for competitive binding studies; (b) Competition experiments on gp120 functionalized surface between dendritic cell-specific intercellular adhesion molecule-3-grabbing non-integrin (DC-SIGN) and homo poly(D-mannose methacrylate) at a concentration range of 0-400 nM for the glycopolymers and 4 nM DC-SIGN.

Meanwhile, the incorporation of glycopolymers also showed promoted interaction with cells and minimizing effects in toxicity of materials applied in biological systems. For instance, Park and co-workers²¹⁹ showed by adjusting the ratio of glycopolymer and anti-bacterial polymer chains, optimal anti-bacterial efficiency as well as biocompatibility could be achieved. In conclusion, pronounced interests of glycopolymer combinations with polyesters for the biomedical applications have been

revealed.

2.2 Experimental overview and hypothesis

In this chapter, to afford well-defined block copolymers, homopolymerization conditions of ϵ -CL, styrene and 2,3,4,5,6-pentafluorostyrene (PFS) were optimized, respectively. Then polymerization sequence was also optimized to minimize the number of dead polymer chains for subsequent reactions. Synthesis of PCL-*mikto*-PS and PCL-*mikto*-PPFS block copolymers were subsequently performed by combining ring opening polymerization (ROP) and atom transfer radical polymerization (ATRP) to afford hydrophobic polymers employing a heterofunctional initiator. Thiol-para-fluorine click reaction was utilized here to functionalized PCL-*mikto*-PPFS into glucose-containing glycopolymers. Lastly, trials on the synthesis of thermo-responsive block copolymers were implemented uniting ROP of ϵ -CL and SET-LRP of *N*-isopropylacrylamide (NIPAM).

ROP of ϵ -CL polymerization was optimized in the aspect of water existence influence, solvent influence, catalyst amount and reaction temperature while ATRP of styrene and PFS were mainly investigated on reaction time to suppress chain-chain coupling. Meanwhile, it was assumed that for the block copolymer synthesis, ROP of ϵ -CL should be carried out first due to the sensitivity of chain ends towards water molecules.

2.3 Materials and methods

2.3.1 Materials

Tin(II) 2-ethyl hexanoate ($\text{Sn}(\text{Oct})_2$, 92.5%-100 %), benzyl alcohol (99.8 %), DL-1,2-isopropylidenglycerol (98 %), α -bromoisobutyryl bromide (Bibb, 98 %), ethyl α -

bromoisobutyrate (EBiB, 98 %), trimethylamine (TEA, BioUltra, ≥ 99.5 %) 1-thio- β -D-glucose sodium salt, aluminium oxide (Al_2O_3), and anhydrous toluene were purchased from Sigma Aldrich and used as received.

N,N,N',N'',N'''-Pentamethyldiethylenetriamine (PMDETA) was purchased from Acros Organics and used as received.

ϵ -CL (97 %) was purchased from Sigma Aldrich, distilled over calcium hydride and stored over molecular sieves under Ar atmosphere before further use.

Styrene (99.5 %, stab. with 4-tert-butylcatechol) was purchased from Alfa Aesar and PFS (99 %, stab. with 0.1 % p-tert-butyl catechol) was purchased from Sigma Aldrich. Both monomers were passed over a basic aluminum oxide column to remove inhibitors prior to use.

NIPAM (97 %) was recrystallized from n-hexane and stored at 4°C before further use.

Copper(I) bromide (Cu(I)Br) was stirred in glacial acetic acid for 4 hours, then filtered and washed with ethanol and dried in vacuum prior to use.

All other reagents and solvents were purchased from Fisher Scientific at the highest purity available and used without further purification.

2.3.2 Measurements and characterization

^1H NMR spectra were recorded on a Bruker AV 400 using CDCl_3 or DMSO-d_6 unless stated otherwise at 303 K. Data was analyzed using ACD/NMR (12.0, ACD Labs, Toronto, Canada) and spectra were reconstructed in Origin 9.0 (OriginLab, Northampton, MA).

SEC measurements were conducted on two different systems. An Agilent 1260 infinity system operating in DMF with 5mM NH_4BF_4 at 40 °C and equipped with refractive

index detector and variable wavelength detector, 2 PLgel 5 μm mixed-C columns (300 \times 7.5 mm), a PLgel 5 mm guard column (50 \times 7.5 mm) and an auto sampler. The instrument was calibrated with linear narrow polystyrene standards in the range of 575 to 281,700 g/mol. Samples with copper catalyst were passed through neutral aluminum oxide while all the samples were filtered using 0.2 μm Nylon filter before analysis.

Some measurements were conducted on a Varian PL-220 infinity system operating in THF with TEA (2 % v/v) and equipped with refractive index detector, 2 PLgel 5 μm mixed-D columns (300 \times 7.5 mm), a PLgel 5 mm guard column (50 \times 7.5 mm) and an auto sampler. The instrument was calibrated with linear narrow polystyrene standards in the range of 575 to 281,700 g/mol. Some samples were passed through the basic aluminum oxide and 0.22 μm PTFE filter before analysis.

All reactions were carried out using standard Schlenk techniques under an inert atmosphere of Argon or Nitrogen.

2.3.3 General synthesis procedures

2.3.3.1 ROP of ϵ -CL

PCL homopolymer was prepared by ring-opening polymerization of ϵ -CL initiated by benzyl alcohol using stannous octoate as catalyst following the procedure reported elsewhere (Figure 2.3)²²⁰. Briefly, monomer, initiator, catalyst and solvent were mixed and transferred into a pre-dried glass Schlenk tube via a degassed syringe, previously vacuumed and Ar purged for 3 times, Then the reaction was sealed under Ar atmosphere and initiated by dipping into a pre-heated oil bath. During the

polymerization, samples were isolated from the reaction mixture employing a degassed syringe for ^1H NMR and GPC to determine monomer conversions and polymer properties. The final polymer solution was diluted with 10 mL of Tetrahydrofuran (THF), precipitated twice in cold methanol, filtered and the final polymer was dried in vacuum at 40 °C overnight, from which a white powder was obtained.

^1H -NMR of PCL (400 MHz, CDCl_3 , ppm, TMS): 1.38 (m, $2\text{H} \times n$, $-\text{CH}_2\text{CH}_2\text{CH}_2\text{CH}_2\text{CH}_2-$), 1.65 (m, $2\text{H} \times n$, $-\text{CH}_2\text{CH}_2\text{CH}_2\text{O}$), 1.65 (m, $2\text{H} \times n$, $-\text{COCH}_2\text{CH}_2\text{CH}_2-$), 2.31 (t, $2\text{H} \times n$, $-\text{OCOCH}_2\text{CH}_2-$), 3.65 (t, $2\text{H} \times n$, $-\text{CH}_2\text{CH}_2\text{O}-$), 4.06 (t, $2\text{H} \times n$, $-\text{CH}_2\text{CH}_2\text{O}-$), 5.2 (s, 2H, $-\text{C}_6\text{H}_5\text{CH}_2-$), 7.3 (s, 5H, $-\text{C}_6\text{H}_5\text{CH}_2-$).

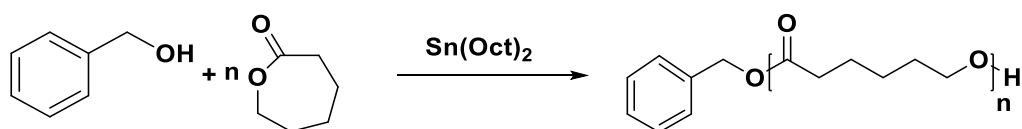


Figure 2.3 ROP of ϵ -CL using benzyl alcohol as an initiator.

2.3.3.2 ATRP of Styrene or PFS

PS or PPFS homopolymers were prepared by ATRP of styrene or PFS initiated by EB*i*B using Cu(I)Br/PMDETA as a catalyst in anisole following the procedure reported elsewhere (Figure 2.4)⁸¹. Monomer: initiator: Cu(I)Br/PMDETA ratio was maintained at 80:1:1 for styrene polymerization and 40:1:1 for PFS polymerization. The typical procedure for the synthesis of PS or PPFS started with degassing the ligand and 50% of the total amount of anisole for 10 minutes. After degassing, the solution was transferred with a degassed syringe to a Schlenk tube containing Cu(I)Br in an inert atmosphere. Cu and the ligand mixture in anisole were degassed for a further 15 minutes. In parallel, styrene or PFS was purged by nitrogen for 15 minutes and then

transferred with a degassed syringe to the mixture. Finally, the degassed macroinitiator and solvent mixture was transferred with a degassed syringe to the Schlenk tube, and the mixture was purged for another 15 minutes before initiating the reaction. The reaction was started by placing the Schlenk tube into an oil bath preheated at 110 °C and stopped by bubbling the solution for 3 minutes with air. Then the solution was further diluted with 10 mL THF. The final block copolymer was purified by passing the dilute solution through the basic Al₂O₃ column to remove the Cu⁰ formed during reactions. The polymer was then precipitated in cold methanol (pH ≈ 3) and then filtered. The final block copolymer was dried in vacuum at 40 °C overnight, from which a white powder was obtained.

¹H-NMR of PS (400 MHz, CDCl₃, ppm, TMS): 1.2-2.2 (b, 3H × n, -CH-CH₂-) 6.3-7.25 (b, 5H × n, C₆H₅).

¹H-NMR of PPFS (400 MHz, CDCl₃, ppm, TMS): 2.0-2.8 (b, 3H × n, -CH-CH₂-).

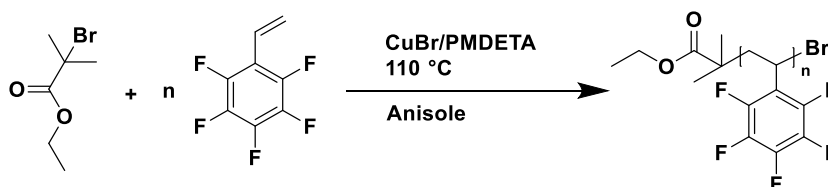


Figure 2.4 ATRP of PFS using EBiB as an initiator.

2.3.3.3 Synthesis heterofunctional initiator

In order to synthesize multi-arm block copolymers combining ROP and ATRP, a hydroxyl and alkyl halides terminated heterofunctional initiator (2, 3-dihydroxypropyl 2-bromo-2-methylpropanoate) was synthesized following a procedure reported before (Figure 2.5)²²¹.

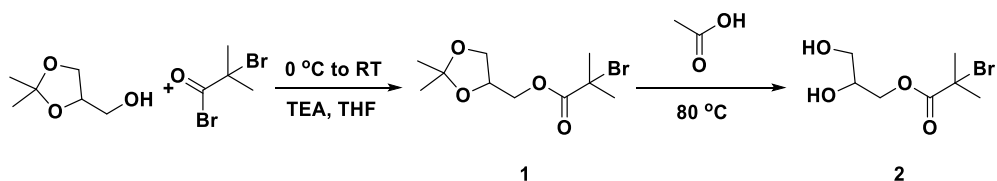


Figure 2.5 Synthesis of the heterofunctional initiator (2).

In the first step, 10 g (0.075 mol) of DL-1,2-isopropylidene-glycerol and 15.3 g (0.15 mol) of TEA were stirred into 38 mL of THF in a 500 mL round-bottom flask and cooled down to 0 °C. A mixture of 19 g (0.083 mol) of BiBB and 100 mL of anhydrous THF was prepared and added dropwise under N₂ atmosphere over a period of 2 hours under constant stirring and stirred for 45 minutes while allowing to heat up to room temperature. The mixture was then poured into an excess of deionized water and the product was extracted by 50 mL diethyl ether. The organic layer was washed two times with aq. HCl (pH ≈ 4.5) and saturated sodium carbonate (3x) respectively. The organic layer was then dried over MgSO₄, filtered and removed by rotary evaporation to yield a yellow oil **1**.

Subsequently, 17.1 g of **1**, 58 mL of glacial acetic acid and 144 mL of water mixture were stirred for 30 minutes at 80 °C to give a homogeneous mixture. The solution was then allowed to cool down to room temperature before 100 mL of diethyl ether was added. The aqueous layer was saturated by portion wise addition of NaHCO₃. The organic layer was separated and the aqueous layer extracted twice with 100 mL of diethyl ether. After combining the organic layers the mixture was concentrated and allowed to crystallize overnight at ambient temperature. The crude yellowish solid was recrystallized from toluene (≈ 1g in 25 mL) to yield crystals as the final heterofunctional initiator **2**.

¹H-NMR of the initiator (400 MHz, CDCl₃, ppm, TMS): 1.95 (s, 6H, -C(CH₃)₂Br),

2.75 (s, 1H, -CH-OH), 2.33 (s, -CH₂-OH), 3.68 (d, 1H, -CH_aH_bOH), 3.74 (d, 1H, -CH_aH_bOH), 4.00 (m, 1H, -CHOH), 4.28 (m, 2H, -CH₂OCO-).

2.3.3.4 Synthesis of miktoarm block copolymers

PCL-*mikto*-PS and PCL-*mikto*-PPFS block copolymers were synthesized by either ROP of ϵ -CL and then ATRP of styrene/PFS or the other way around (Figure 2.6). The first polymerization was initiated by the synthesized heterofunctional initiator and the obtained polymer was purified by precipitation. Then the polymer was used as a macroinitiator to initiate the chain extension reaction to afford miktoarm copolymers. The obtained PCL-*mikto*-PS and PCL-*mikto*-PPFS copolymers were precipitated into cold methanol (pH \approx 3) and dried in an oven at 40 °C overnight to yield a white powder.

¹H NMR of PCL-*mikto*-PS (400 MHz, CDCl₃, ppm, TMS): 1.20-2.20 (b, 3H \times m, CH₂CH(C₆H₅)), 1.39 (m, 2H \times n, -COCH₂CH₂CH₂CH₂CH₂O-), 1.66 (m, 4H \times n, -COCH₂CH₂CH₂CH₂CH₂O-), 2.32 (t, 2H \times n, -COCH₂CH₂CH₂CH₂CH₂O-), 4.07 (t, 2H \times (n-1), -COCH₂CH₂CH₂CH₂CH₂O-), 6.3-7.25 (b, 5H \times m, C₆H₅).

¹H NMR of PCL-*mikto*-PPFS (400 MHz, CDCl₃, ppm, TMS): 1.75-2.90 (b, 3H \times m, CH₂CH(C₆F₅)), 1.39 (m, 2H \times n, -COCH₂CH₂CH₂CH₂CH₂O-), 1.66 (m, 4H \times n, -COCH₂CH₂CH₂CH₂CH₂O-), 2.32 (t, 2H \times n, -COCH₂CH₂CH₂CH₂CH₂O-), 4.07 (t, 2H \times (n-1), -COCH₂CH₂CH₂CH₂CH₂O-).

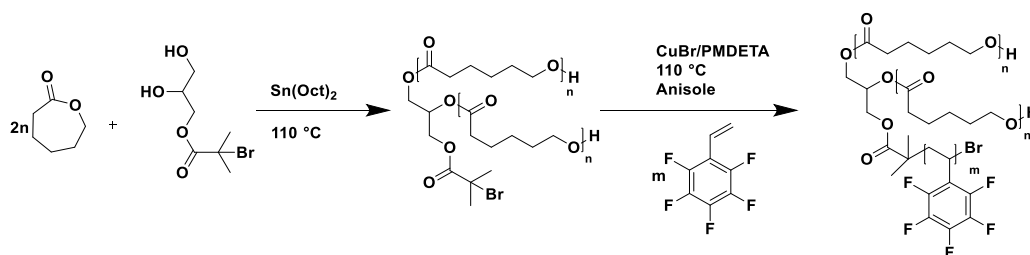


Figure 2.6 ROP of ϵ -CL and then ATRP of PFS.

2.3.3.5 Para-fluorine click reaction using 1-thio-β-D-glucose

The general method for performing the click reaction has been reported elsewhere and was adopted here, with a modification to the reaction time (Figure 2.7)¹⁸⁰. In brief, the click reaction was performed by mixing PCL-*mikto*-PPFS copolymer (1.00 g, 2.37 mmol) with the unprotected thio-glucose (510 mg, 2.37 mmol) and all chemicals were dissolved in 8 mL of dry DMF. TEA (1.00 mL, 7.02 mmol) was added to the mixture as a base. The reaction mixture was stirred for 19 h at 40 °C, concentrated to 2.5 mL, precipitated into cold methanol twice and filtered. The final block copolymer PCL-*mikto*-PTFSGlc was dried in vacuum at 40 °C overnight and obtained as a white powder. The obtained PCL-*mikto*-PTFSGlc copolymers were precipitated into cold methanol twice and dried in an oven at 40 °C overnight to afford a white powder.

¹H NMR of PCL-*mikto*-PTFSGlc (400 MHz, DMSO-d₆, ppm, TMS): 1.75-2.90 (b, 3H × y, CH₂CH(C₆F₄(S-C₆H₅O-(OH)₅))), 1.39 (m, 2H × n, -CH₂CH₂CH₂CH₂CH₂-), 1.66 (m, 2H × n, -CH₂CH₂CH₂O), 1.66 (m, 2H × n, -CO CH₂CH₂CH₂-), 2.31 (t, 2H × n, -OCOCH₂CH₂-), 3.65 (t, 2H × n, -CH₂CH₂O-), 4.07 (t, 2H × (n-1), -CH₂CH₂O-), 4.2-5.5 (broad multiplet, 10H × m, -S-C₆H₅O-(OH)₅).

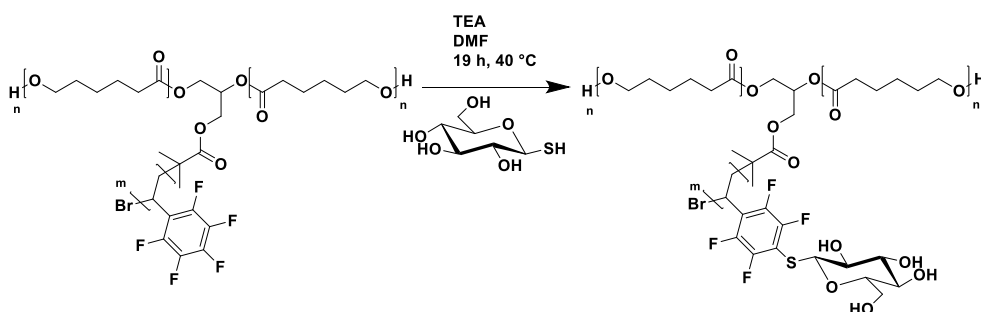


Figure 2.7 Para-fluorine click reaction using 1-thio-β-D-glucose.

2.3.3.6 Synthesis of thermo-responsive block copolymers

The polymerization was carried out as described above (Figure 2.8)²²². In brief, Cu(I)Br was added to a nitrogen purged Schlenk tube fitted with a magnetic stirrer bar and followed by further 10 minutes of degassing. Meanwhile, Me₆TREN was mixed with half of the total amount of H₂O and was degassed for 15 minutes. Then the ligand/solvent mixture was transferred with a degassed syringe into Cu(I)Br containing flask and the disproportionation reaction was allowed to proceed at room temperature for 30 minutes. NIPAM in H₂O and PCL in THF were degassed for 20 minutes at the same time and added to a Schlenk tube subsequently. The reaction was started by adding the PCL macroinitiator in THF solution at room temperature and stopped by bubbling with air for 3 minutes. The final reaction mixture was analyzed by GPC and NMR to determine the molecular properties and monomer conversion. Monomer conversion for NIPAM was calculated by comparing the integration of backbone protons of the polymer with the vinyl protons of the monomer in the ¹H NMR spectra. The obtained PCL-*mikto*-PNIPAM copolymers were precipitated into cold diethyl ether twice and dried in an oven at 40 °C overnight to afford a white powder.

¹H NMR of PCL-*mikto*-PNIPAM can be found in Figure 2.22 (400 MHz, CDCl₃, ppm, TMS): 1.13 (s, 6H × m, -NHCH(CH₃)₂), 1.66 (m, 2H × n, -CH₂CH₂CH₂CH₂CH₂-), 1.5-1.7 (m, 4H × n, -CH₂CH₂CH₂CH₂CH₂-), 1.7-2.1 (s, 3H × m, -CHCH₂-), 2.30 (t, 2H, -CH₂CH₂CO-), 3.96 (b, H × m -NHCH(CH₃)₂), 4.07 (t, 2H × (n-1), -CH₂CH₂O-), 6.52 (b, H × m, -NHCH(CH₃)₂).

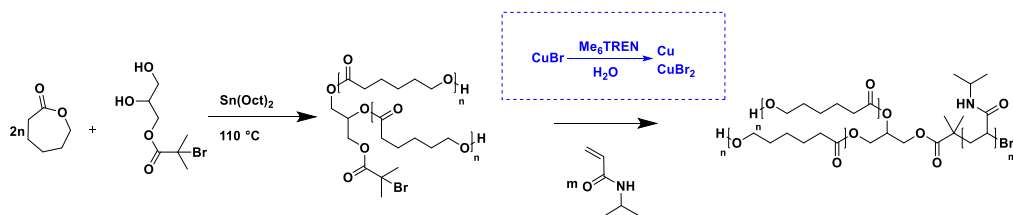


Figure 2.8 SET-LRP of NIPAM and then ROP of ϵ -CL.

2.4 Results and discussion

2.4.1 Optimization of ROP of ϵ -CL

ROP of ϵ -CL was carried out using benzyl alcohol as an initiator and Sn(Oct)₂ as a catalyst. Firstly, ϵ -CL was used directly from the bottle without purification and polymerized at 110 °C for 24 h in bulk. GPC results indicated (Figure 2.9) the existence of two different polymer distributions with high polymer dispersity (1.60), which might be due to the existence of water in the system. Polymers could be initiated from either benzyl alcohol or water, which leads to two different polymer species. Meanwhile, transesterification reaction is one of the most commonly seen reactions in ROP and will lead to the formation of non-uniform polymer chain distribution, observed by the low retention time shoulder and high retention time tailing in the GPC trace. Thus distilled ϵ -CL was used for the rest of polymerizations.

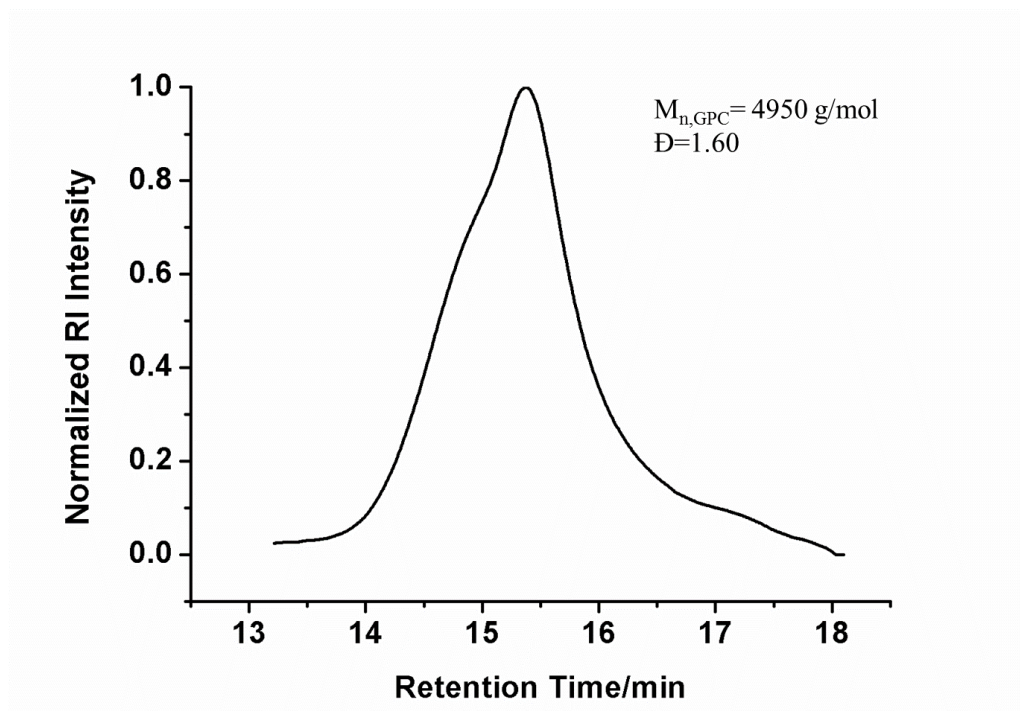


Figure 2.9 GPC trace of PCL polymerized from non-distilled ϵ -CL.

The polymerization was optimized by the catalyst amount, solvent influence and reaction temperature. The properties of final polymers were characterized using GPC and NMR spectroscopy. Table 2.1 shows the summary of the results obtained from the optimization reactions for ROP of ϵ -CL. At lower catalyst loading, only polymers with low DP were obtained (Table 2.1 (P1)) while the increase of the catalyst leading to higher monomer conversion and produce longer polymer chains (Table 2.1 (P2)). However, further increase in catalyst amount led to a significant amount of transesterification reaction and afforded a bimodal distribution in the GPC traces (Table 2.1 (P3), Figure 2.10 (P3)).

In further note, the polymers obtained in bulk polymerization normally possess high polydispersity (P1-P3). In order to achieve better control over polymer properties, anhydrous toluene was introduced as a solvent. The results shown introduced toluene significantly lowered the \bar{D} of the final product (Table 2.1 (P4-P5)) and afforded

narrowly distributed polymers (Figure 2.10 (P4-P5)). However, too much solvent led to the notable decrease of the polymerization rate and an increase in reaction time.

The effect of reaction temperature was also investigated in this study. Polymerization did not proceed at 90 °C confirmed by the absence of polymer formation employing Sn(Oct)₂ as a catalyst. When elevating the reaction temperature to even higher temperatures (130 °C), the polymerization reached to 97 % conversion after 9 h with relatively good control over molecular weight and Đ (Table 2.1 (P6) and Figure 2.10 (P6)).

In conclusion, the ROP of ε-CL was optimized in the aspect of catalyst amount, solvent amount, reaction temperature and temperature. Catalyst amount influences the reaction rate and also led to the existence of side reactions. Addition of solvent to the system lowers the reaction speed whilst improve the control over polymer properties. Meanwhile, the increase of reaction temperature accelerates the reaction rate without the loss of control over final polymers. In summary, after optimization, ROP of ε-CL could be achieved at 130 °C for 9 h with decent control over polymer properties.

Table 2.1 Summary of the results obtained from the optimization reactions for ROP of ϵ -CL

Entry	[M]:[I] :[Catalyst]	Solvent ^a / Monomer volume ratio	<i>T</i> [°C]	Time [h]	Conversion ^b [%]	<i>M_n</i> ,GPC ^c [g/mol]	<i>D</i>
P1	50:1:0.005	In bulk	110	24	15	1030	1.37
P2	50:1:0.025	In bulk	110	24	100	5740	1.60
P3	50:1:0.05	In bulk	110	24	100	6750	1.92
P4	50:1:0.025	1:1	110	24	13	890	1.19
P5	50:1:0.025	1:5	110	24	93	5580	1.23
P6	50:1:0.025	1:5	130	9	97	5700	1.25

^a Toluene was used here as a solvent; ^b Conversion calculated from ¹H NMR; ^c DMF eluent, linear PS standards.

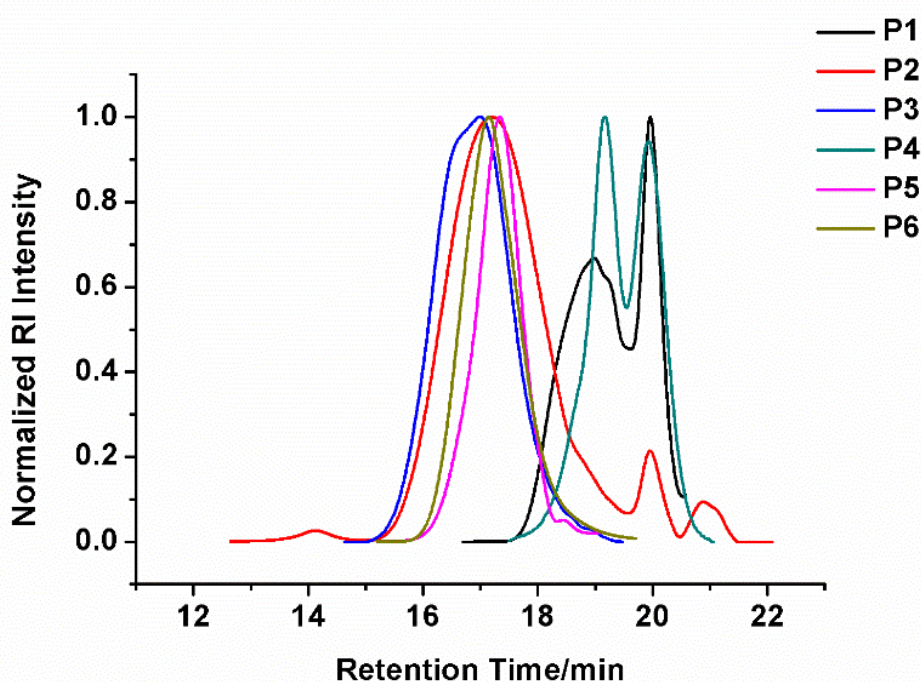


Figure 2.10 GPC traces of polymers from the optimization reactions for ROP of ϵ -CL.

Purified PCL was isolated with an 85 % yield. ¹H NMR of PCL can be found in Figure 2.11. NMR result shows the appearance of polymer peak and complete removal of

monomer and solvent in the final purified product.

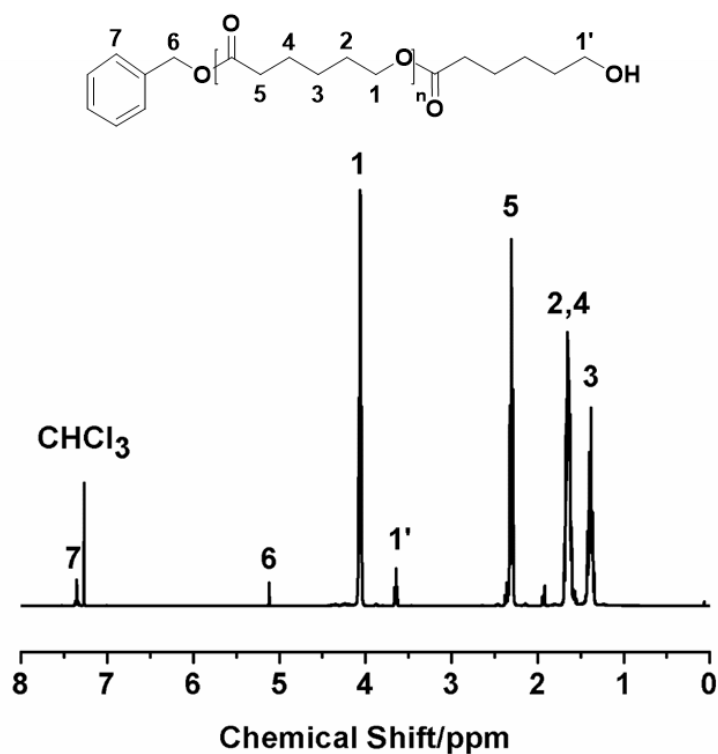
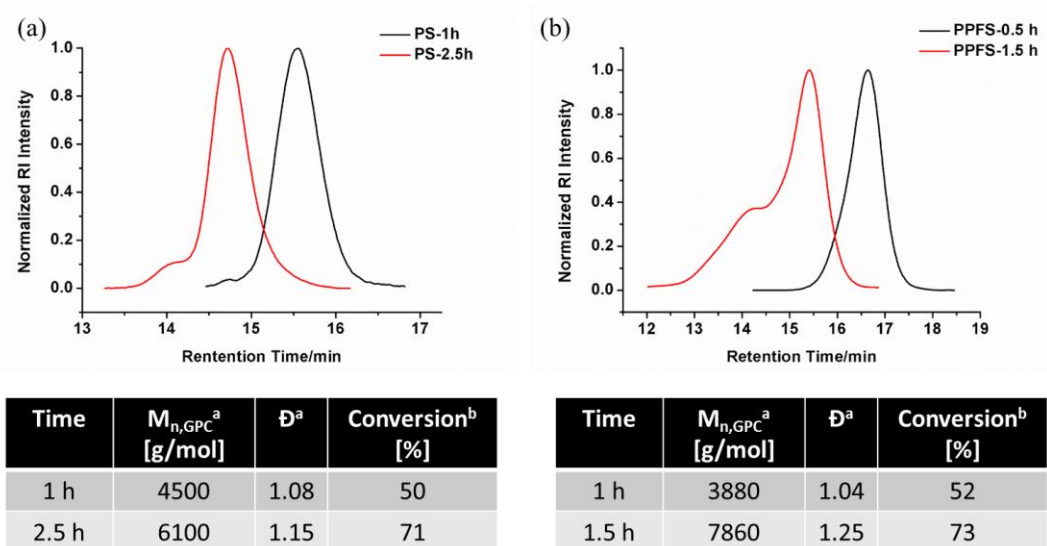


Figure 2.11 ^1H NMR of homo PCL. The result confirms the formation of polymers and complete removal of solvent and left-over monomers.

2.4.2 Optimization of ATRP of styrene and 2,3,4,5,6-pentafluorostyrene.

PS or PPFS homopolymers were prepared by ATRP of styrene or PFS initiated by EB*i*B using Cu(I)Br/PMDETA as a catalyst in anisole. The reaction was carried out at $110\text{ }^\circ\text{C}$ and samples were isolated from the reaction mixture employing a degassed syringe for ^1H NMR and THF GPC to determine monomer conversions at predetermined time points.



^a DMF eluent, linear PS standards; ^b Conversion calculated from ¹H NMR.

Figure 2.12 GPC traces obtained from ATRP of (a) styrene and (b) PFS at different time points. GPC traces show the growth of the polymers after the chain extension step. Additionally, chain-chain coupling reactions, which leads to increase of polymer dispersity, were observed in the polymers after longer reaction time.

The GPC results show ATRP of styrene maintained narrow polymer distribution ($\bar{D}=1.08$) without chain-chain coupling after 1 h reaction (50 % monomer conversion) (Figure 2.12 (a)) and chain-chain coupling was observed when monomer conversion reached higher values (70 %, $\bar{D}=1.15$) at 2.5 h. Compared to styrene, PFS polymerization was observed to possess higher reaction rate but also sustained control ($\bar{D}=1.04$) over polymerization at 50 % monomer conversion after 30 minutes while starting to form chain-chain coupling products ($\bar{D}=1.25$) at higher monomer conversions when left the reaction for an hour (Figure 2.12 (b)).

Final purified PS and PPFS were isolated with a 50 % yield attributed to the copper removal step. ¹H NMR of PS can be found in Figure 2.5 (a) and ¹H NMR of PPFS can be found in Figure 2.5 (b). NMR results confirmed the polymer formation and removal of monomer and solvent after purification.

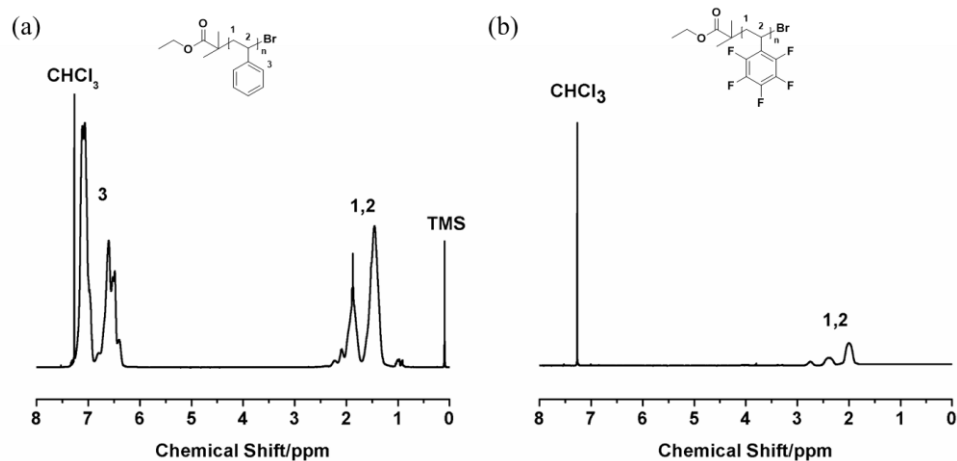


Figure 2.13. ^1H NMR of homo (a) PS and (b) PPFS. The result confirms the formation of polymers and complete removal of solvent and left-over monomers.

2.4.3 Synthesis of heterofunctional initiator

2,3-dihydroxypropyl 2-bromo-2-methylpropanoate was synthesized in a two-step process. The first step of the reaction was esterification between the Bibb and DL-1,2-isopropylidenglycerol under the catalysis of TEA in THF and the second step of the reaction was the deprotection of the hydroxyl groups.

The heterofunctional initiator was obtained as white crystals with a 65 % yield. ^1H -NMR of the initiator can be found in Figure 2.14. NMR Spectrum confirms the chemical structure and the purity of the structure in the final product.

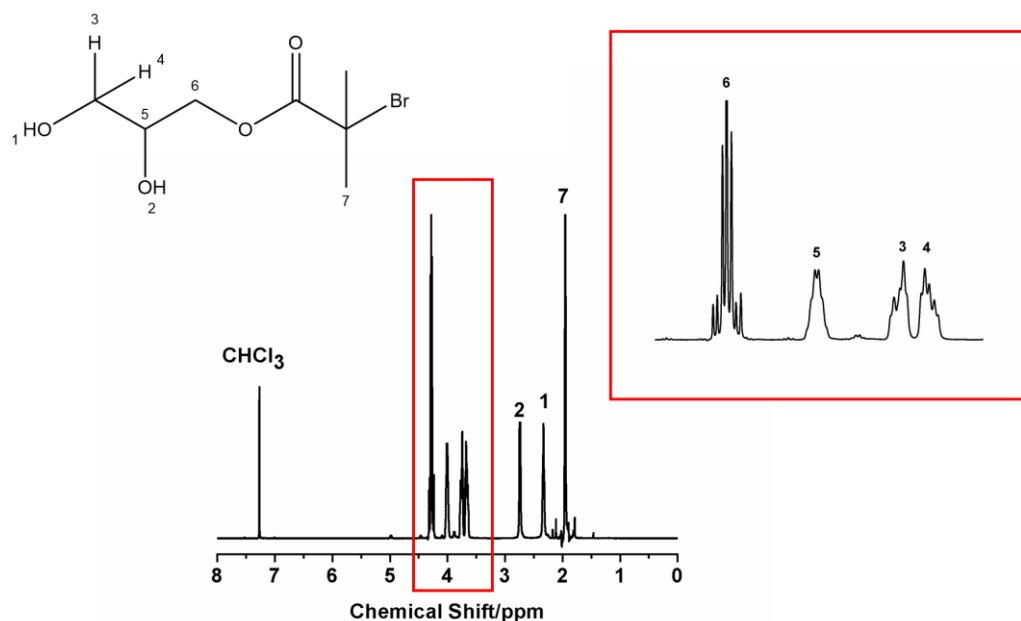


Figure 2.14 ^1H NMR of the heterofunctional initiator (2). NMR Spectrum confirms the chemical structure and the purity of the structure in the final product.

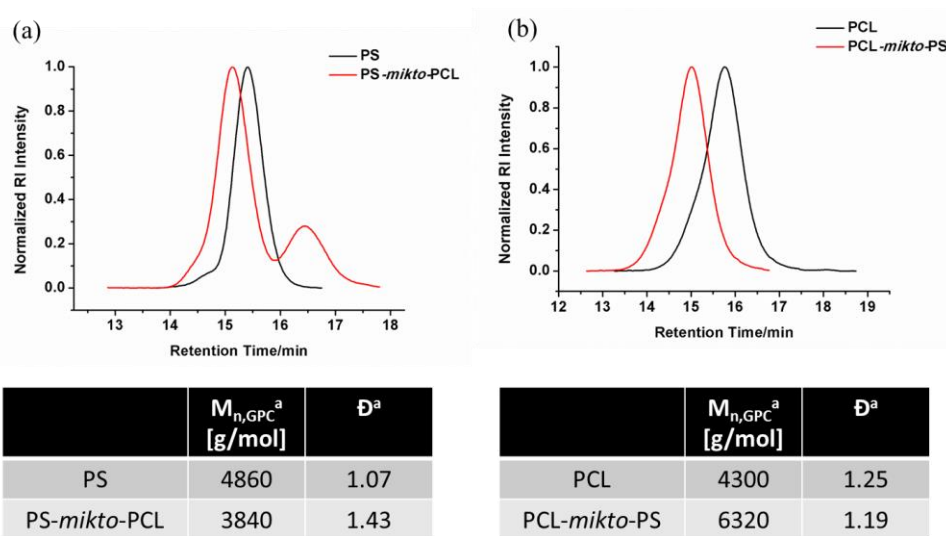
2.4.4 Synthesis of miktoarm block copolymers using the heterofunctional initiator

Synthesis conditions of PCL-*mikto*-PS and PCL-*mikto*-PPFS block copolymers were optimized. Reactions were carried out in either ROP of ϵ -CL and then ATRP of styrene or the other way around.

In both circumstances, homo PCL and homo PS (PPFS) were synthesized using the heterofunctional initiator followed by precipitation in cold methanol twice. The obtained white powder was filtered, dried and kept in the fridge until further use.

PCL ($M_{n,theo} \approx 11600 \text{ g mol}^{-1}$) and PS ($M_{n,theo} \approx 6000 \text{ g mol}^{-1}$) were used as macroinitiators for the chain extension reactions. Either PCL or PS was used as a macroinitiator to initiate the chain extension reaction. Figure 2.15 shows the GPC traces before and after chain extension reaction. In Figure 2.15 (a), it can be seen that

when PS was utilized here as the macroinitiator, not only PS-*mikto*-PCL was formed, but homo PCL was initiated by impurities in the system. However, when PCL was used as a macroinitiator, there is a clear shift in the GPC traces without leftover macro initiators or side polymers and \bar{D} stays low after the chain extension (Figure 2.15 (b)). This difference was caused by the sensitivity of ROP and the tolerance of ATRP system towards the water. Starting from here, PCL-*mikto*-PS and PCL-*mikto*-PPFS block copolymers were synthesized always utilizing PCL as a macroinitiator.



^a DMF eluent, linear PS standards.

Figure 2.15 GPC traces of (a) PS first and then PCL and (b) PCL first then PS. The GPC traces show the growth of polymer chains after chain extension reactions. However, lower molecular weight polymers were formed when using PS as the macro initiator while only block copolymers were synthesized utilizing PCL as the macro initiator.

Similar to homopolymerization of styrene and PFS, PCL-*mikto*-PS and PCL-*mikto*-PPFS block copolymers were prepared utilizing the PCL macroinitiator in anisole at 110 °C. The monomer: initiator: Cu(I)Br: PMDETA ratio was maintained at 80:1:1:1 for all the polymerizations. Samples were isolated from the reaction mixture to monitor reaction process.

Figure 2.16 shows the kinetic results of PCL-*mikto*-PS and PCL-*mikto*-PPFS at

different time points. The PCL macroinitiator has been successfully converted into block copolymers observed by a clear shift in GPC. Well-defined block copolymers with low polydispersity were obtained at $\approx 70\%$ (Figure 2.16 (a), (c) and (e)). However, compared with homopolymerization of styrene, monomers were consumed slower (50 % monomer consumption after 7 hours) while could reach higher conversion without chain-chain coupling of polymer chains compared to the case in homo polymerization, which can attribute to the higher steric hindrance of the macroinitiator compared with the heterofunctional initiator. Furthermore, in line with the homopolymerization results before, PFS was consumed faster than styrene at the same time point (Figure 2.16 (c) and (d)). Similarly, PFS was consumed slower (50 % monomer consumption after 4 hours) while could reach higher conversion without chain-chain coupling of polymer chains (Figure 2.16 (b), (d) and (f)) compared to the case in homo polymerization.

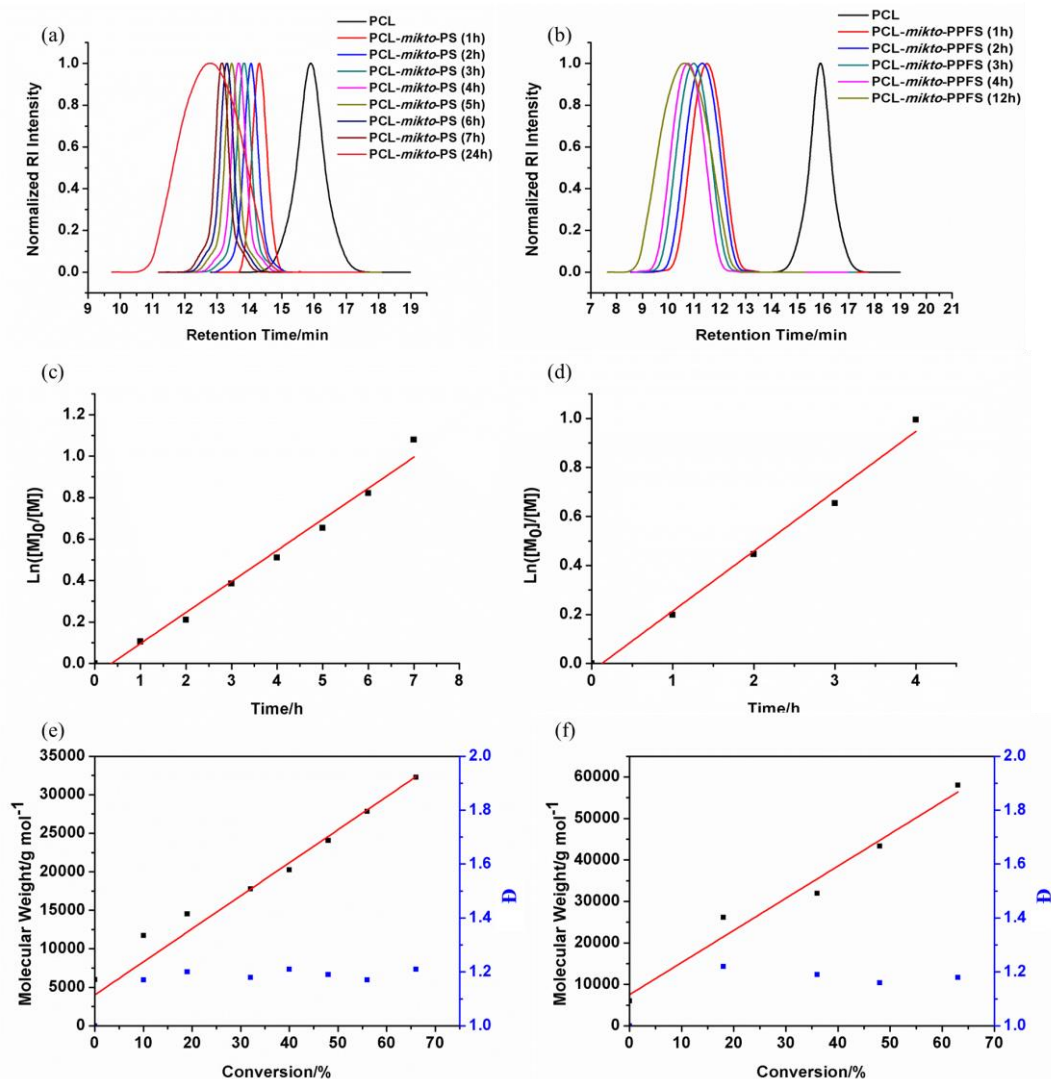


Figure 2.16 GPC traces of (a) PCL-*mikto*-PS and (b) PCL-*mikto*-PPFS at different time points using the PCL macroinitiator; (c) styrene and (d) PFS monomer conversion by ^1H NMR with time; (e) and (f) molecular weight and \bar{D} of block copolymers. The GPC traces (a) and (b) show the complete growth of the macro initiator during the chain extension reactions. Images (c), (d), (e) and (f) shows the linear relationship between molecular weight with time and conversion. The \bar{D} of polymers also maintains low during the polymerization which shows the successful control over polymerization.

PCL-*mikto*-PS was isolated with a 47 % yield while PCL-*mikto*-PPFS was purified with a 45 % yield. ^1H NMR of PCL-*mikto*-PS can be found in Figure 2.17 (a) and ^1H NMR of PCL-*mikto*-PPFS can be found in Figure 2.17 (b). NMR spectra shows the appearance of both PCL and PS/PPFS peaks in the final block copolymers. Together with the GPC traces before, the formation of block copolymers were confirmed.

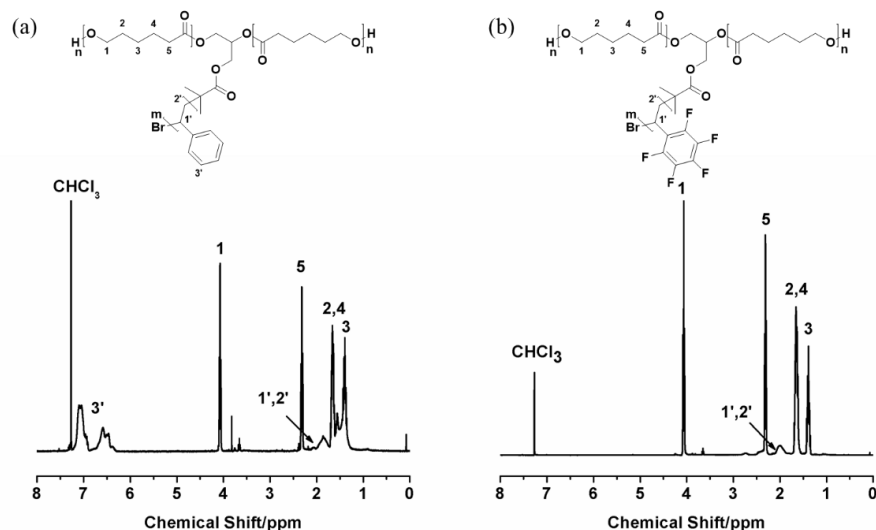


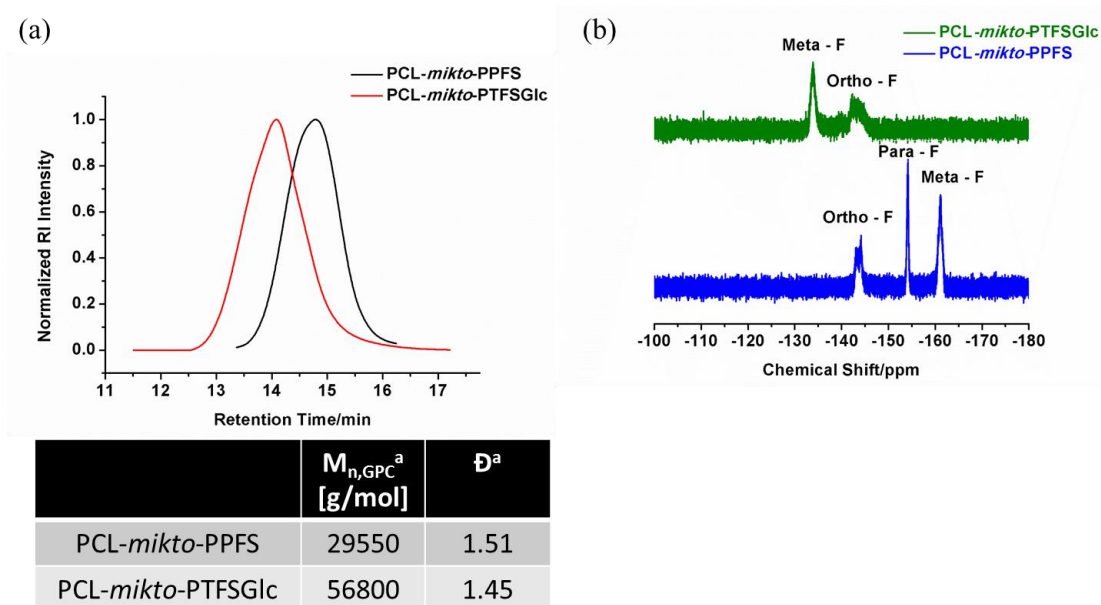
Figure 2.17 ^1H NMR of purified (a) PCL-*mikto*-PS and (b) PCL-*mikto*-PPFS. The result confirms the formation of block polymers and complete removal of solvent and left-over monomers.

2.4.5 Synthesis of miktoarm glycopolymer

PCL-*mikto*-PTFSGlc was obtained by functionalizing PCL-*mikto*-PPFS utilizing para-fluorine click reaction of 1-thio- β -D-glucose. The reaction was carried out in DMF at 40 °C for 19 h.

GPC results (Figure 2.18 (a)) and ^{19}F NMR (Figure 2.18 (b)) spectroscopy indicate the quantitative consumption of para fluorine groups after the click reaction and

successful preparation of PCL-*mikto*-PTFSGlc.



^a DMF eluent, linear PS standards.

Figure 2.18 (a) GPC traces and (b) ¹⁹F NMR of PCL-*mikto*-PPFS and PCL-*mikto*-PTFSGlc. The GPC traces (a) shows the growth of polymer chains and (b) ¹⁹F NMR shows the complete consumption of *para*-fluorine in the polymers.

Purified PCL-*mikto*-PTFSGlc was isolated with an 80 % yield. ¹H NMR of PCL-*mikto*-PTFSGlc can be found in Figure 2.19. NMR spectra shows the appearance of sugar peaks after the click reaction. Together with the GPC traces before, the formation of glycopolymers was confirmed.

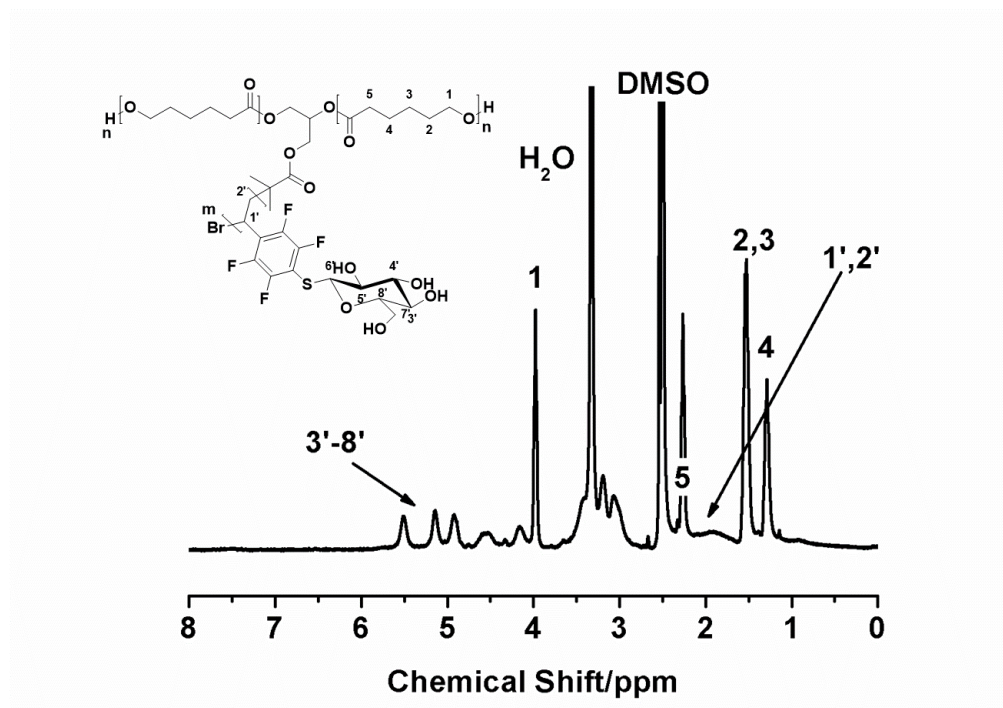


Figure 2.19 ^1H NMR of purified PCL-*mikto*-PTFSGlc. The result confirms the formation of glycopolymers after the *para*-fluorine click reactions.

In conclusion, PCL, PCL-*mikto*-PS, PCL-*mikto*-PPFS and PCL-*mikto*-PTFSGlc were successfully synthesized combining ROP and ATRP to afford well-defined miktoarm copolymers. The molecular weight, \bar{D} and conversion of each copolymer shown in Table 2.2. Purified polymers were directly employed to produce 3D scaffold with different hydrophobicity in the next stage utilizing electrospinning.

Table 2.2 Summary of the results of PCL, PCL-*mikto*-PS, PCL-*mikto*-PPFS and PCL-*mikto*-PTFSGlc

Composition ^a	Conversion [%]	$M_{n,theo}$ [g mol ⁻¹]	$M_{n,GPC}^d$ [g mol ⁻¹]	\bar{D}^d	
(PCL ₈₀) ₂	CL	100 ^b	11600	18190	1.46
(PCL ₈₀) ₂ - <i>mikto</i> -PS ₅₆	Styrene	70 ^b	22420	27350	1.29
(PCL ₈₀) ₂ - <i>mikto</i> -PPFS ₅₉	PFS	65 ^b	28280	29550	1.51
(PCL ₈₀) ₂ - <i>mikto</i> -PTFSGlc ₅₉	Thio-glucose	100 ^c	51410	56800	1.45

^a Calculated by GPC results; ^b Conversion (ρ) measured by ^1H NMR; ^c Conversion (ρ) measured by ^{19}F NMR; ^d DMF eluent, PS standards.

2.4.6 Synthesis of thermo-responsive miktoarm block copolymers

To provide more advanced properties to the system, thermo-responsive polymer PNIPAM was copolymerized with PCL through a combination of ROP and SET-LRP. According to the results from the optimization reactions before, PCL-*mikto*-PNIPAM was synthesized employing PCL as a macroinitiator.

Benefiting from the comparable lower critical solution temperature (LCST) of PNIPAM to body temperature, it has been widely used in the fabrication of thermo-responsive carriers²²³. PNIPAM could be polymerized via ATRP²²⁴, RAFT²²⁵ or SET-LRP²²⁶ while SET-LRP in aqueous system showed the optimal control over polymer properties and structure within a short reaction time²²². Thus here, aqueous SET-LRP was decided to be combined with ROP to afford PCL-*mikto*-PNIPAM.

Monomer: initiator: Cu(I)Br: Me₆TREN ratio was maintained at 80:1:0.16:0.24 for all polymerization reactions. Reactions were carried out at 25 °C and samples were withdrawn from the reaction mixture employing a degassed syringe for ¹H NMR and GPC analysis to determine monomer conversions and molecular weights, respectively, at predetermined time points. However, the solubility of the PCL macroinitiator in water restricted the chain extension reaction in pure aqueous system followed by utilizing the THF/water biphasic system. The ratio of THF/water was adjusted and the representative picture of reaction mixtures could be found in Figure 2.20. It is worth noting that when THF volume ratio is above 50 %, Cu(I)Br cannot disproportionate into Cu(0) observed by no formation of Cu(0) powder, which acts as the reactive species in aqueous SET-LRP. However, when THF ratio was below 25 %, the PCL macroinitiator aggregated into precipitates (Figure 2.20 (a)) which also prevented this

reaction. When THF ratio was elevated to 33 %, PCL could disperse into the solution phase and form emulsion solution (Figure 2.20 (b)). Further increase in THF amount led to the formation of a homogenous solution without interference with the disproportionation process (Figure 2.20 (c)).

GPC results indicate the solvent effect on initiator efficiency. Figure 2.21 (a) shown that the PCL macroinitiator cannot fully initiate the polymerization if it is not completely soluble. The fully soluble system allows a complete shift in the GPC traces with less than 15 % initiator left (Figure 2.21 (b)).

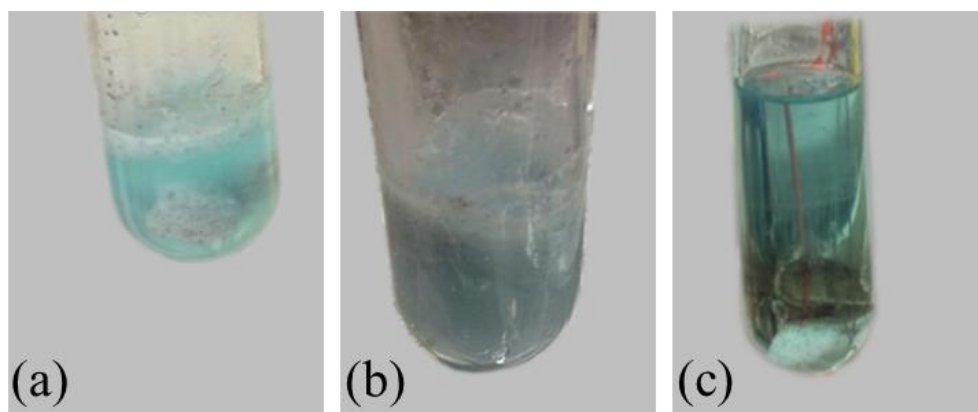


Figure 2.20 Reaction mixture using (a) 3: 1, (b) 2: 1 and (c) 1: 1 water: THF volume ratio. Image (a) shows the formation of polymer precipitates in 3:1 water: THF mixture. Dispersion solution without large aggregation (Image b) was observed with the increase in water: THF ratio to 2:1 and clear soluble reaction mixture was formed with further increase in THF amount to 50 %.

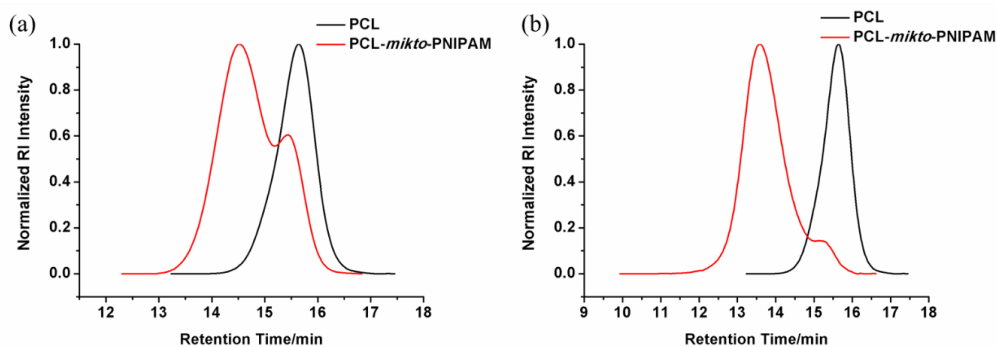


Figure 2.21 GPC traces of PCL-*mikto*-PNIPAM in (a) 2:1 and (b) 1:1 water/THF volume. All the GPC traces show the growth of polymer chains after chain extension reactions. However, significant lower amount of uninitiated macro initiator was left in the system with higher THF ratio.

PCL-*mikto*-PNIPAM was isolated with a 44 % yield. ^1H NMR of PCL-*mikto*-PNIPAM can be found in Figure 2.22. NMR spectra shows the appearance of NIPAM peaks and together with the GPC traces, confirm the formation of PCL-*mikto*-PNIPAM.

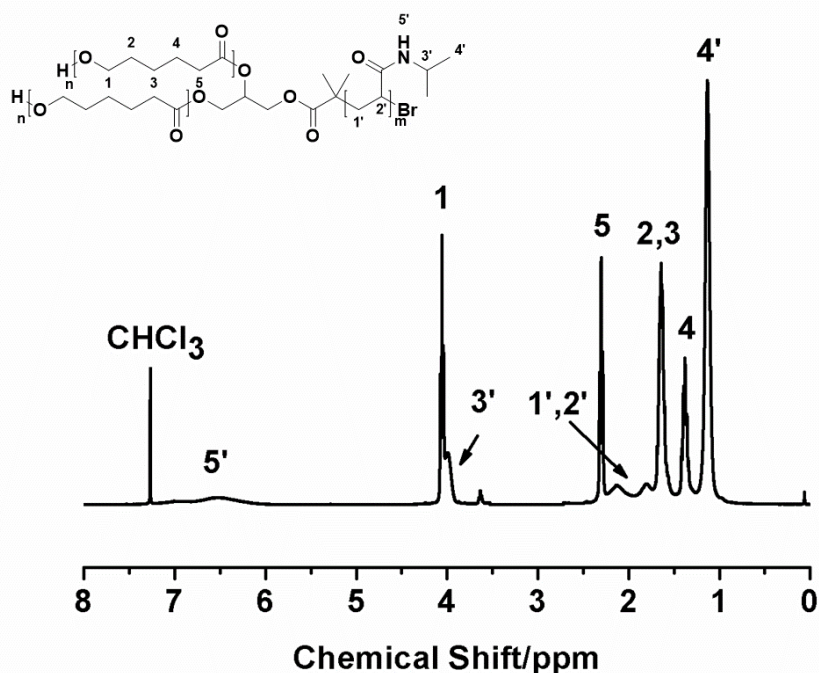


Figure 2.22 ^1H NMR of purified PCL-*mikto*-PNIPAM. The result confirms the formation of PCL-*mikto*-PNIPAM after the chain extension reactions.

In conclusion, miktoarm thermo-responsive polymer PCL-*mikto*-PNIPAM were successfully synthesized by a combination of ROP and SET-LRP, which showed the potential to functionalize PCL with more advanced properties.

2.5 Conclusion

In this chapter, ROP of ϵ -CL, and ATRP of styrene and PFS were optimized. Then heterofunctional initiator was designed and synthesized to combine ROP with ATRP and SET-LRP followed by miktoarm block copolymers synthesis through core first approach. Lastly, para-fluorine click reaction was utilized here to graft sugar moieties onto polymer backbone and functionalized PCL with bioactive molecules.

The results showed the successful synthesis of PCL, PCL-*mikto*-PS, PCL-*mikto*-PPFS, PCL-*mikto*-PTFSGlc and PCL-*mikto*-PNIPAM was effectively synthesized with well-defined polymer properties. PCL was obtained using ROP at 130 °C for 9 hours utilizing toluene as solvent. Then PCL was employed as a macroinitiator to afford PCL-*mikto*-PS and PCL-*mikto*-PPFS via ATRP at 110 °C in anisole for 8 hours and 4 hours, respectively. Followed on this, and PCL-*mikto*-PTFSGlc was synthesized using para-fluorine click reaction. Lastly, thermos-responsive PCL-*mikto*-PNIPAM was achieved by a chain extension reaction of PCL via co-solvent mixture. All polymer samples were characterized using GPC and NMR to evaluate the chemical compositions. In summary, these polymers are successfully synthesized and will be fabricated into materials in the next chapters to characterize their performance for the promotion of tendon healing and related biological properties.

Chapter 3. Materials development and optimization

3.1 Introduction

In chapter 2, three block copolymers with distinct chemical compositions, poly (ϵ -caprolactone-*mikto*-polystyrene) (PCL-*mikto*-PS), poly (ϵ -caprolactone-*mikto*-poly (2,3,4,5,6-pentafluorostyrene) (PCL-*mikto*-PPFS), poly (ϵ -caprolactone-*mikto*-poly (4-(1-thio- β -D-glucopyranosido)-2,3,5,6-tetrafluorostyrene) (PCL-*mikto*-PTFSGlc), were synthesized, with potential interests for further medical applications. However, in order to implement the synthetic polymers in tissue regenerations like tendon regeneration and healing, polymers need to be manufactured into 3D membranes. Common methods for the design and fabrication of 3D porous membranes include electrospinning⁸⁷, self-assembly⁸⁹, 3D²²⁷ or 4D printing²²⁸. All these methods offer the advantages of highly organized biomimetic structures²²⁹ and easily programmable production of the final products²³⁰. However, electrospinning remains to be one of the most widely used approaches owing to the simple, straightforward process of obtaining ultrafine fibres with comparable dimension to native tissue⁹².

For electrospinning, an electric voltage is employed to generate smooth and uniform fibres bundles at the macro or nano scale⁹⁷, and the dimension of the fibres can be manipulated by changing the compound solution properties, applied voltage, or environmental parameters⁹⁵. Spinning conditions were first optimized in order to produce uniform and smooth fibres, and also to control factors such as aligning fibre orientation²³¹ employing a rotating drum. Luo and coworkers showed how fibre alignment alters cell signaling and provides more physiological organized structures²³⁰. Specifically for tendon-related disease, the ability to recapitulate aligned fibre structures shows promise for promoting tendon healing and stimulating cell

functions²³²⁻²³³. However, for any given polymer, electrospinning conditions need to be optimized based on the specific compound, for efficient control over fibre properties.

3.2 Experiments overview and hypotheses

The goals of this chapter are to optimize the electrospinning processes to manufacture membranes with uniform and smooth fibre morphologies for further analysis, and then to characterize the mechanical properties of the resulting membranes. Firstly, the translation of block copolymers synthesized in chapter 2 allows the fabrication of real material that can be utilized in tendon injuries to afford both anti-adhesive and healing promotion properties. Additionally, to obtain suitable platform for tendon healing, aligned porous fibrous membranes with improved mechanical properties, which potentially could reduce the suture number utilized in surgeries and achieve cell patterning on the inner side of the final product, are the main rationale of this chapter. The hypothesis is that membranes will have consistent material properties, despite the different chemical compositions of the four polymers, but that material properties can be manipulated by altering fibre alignment in the electrospinning process. The materials should also be able to maintain a stable mechanical behavior under cyclic movement.

3.3 Methods

3.3.1 Preparation of polymer electrospinning solutions

In order to produce continuous fibre bundles, sufficient chain-chain entanglement within the electrospun solutions is required¹¹⁷, which can be achieved by adding a

high molecular weight constituent to the solution¹⁰⁸. High molecular weight PCL (Capa™ 6500D, Mw ≈ 50000 Da) was kindly provided by Perstorp Winning Formulas Corporation and utilized here to provide enough chain-chain entanglement. Homo-PCL was first used in isolation to optimize initial electrospinning conditions, mixing it at different chloroform (CHCl₃): dimethylformamide (DMF) ratios and then also with various polymer concentrations. Once preliminary settings were established, PCL-*mikto*-PS, PCL-*mikto*-PPFS, PCL-*mikto*-PTFSGlc were mixed with homo-PCL at 1:4 weight ratio to prepare the electrospinning solutions for manufacturing membranes. It should be noted that specifically for the electrospinning of PCL-*mikto*-PTFSGlc, the insolubility of the polymer in CHCl₃, meant ethyl formate was used instead, which is known to ensure PCL solubility²³⁴. All the solutions were stirred for at least six hours to achieve homogenous mixtures before electrospinning into fibres.

3.3.2 Electrospinning

The polymer solutions were transferred to a plastic syringe (5 ml, Injekt®, Braun, Germany) fitted with a metal needle (0.8 mm diameter), and then connected with a 20-gauge PTFE syringe tube onto the pump. The flow rate of the polymer solution was controlled by a programmable syringe pump (Genie, Kent Scientific Corporation, USA). All membranes were electrospun at 25 kV, supplied directly from a high DC voltage power supply (0-30 kV, Glassman High Voltage Inc, Whitehouse Station, NJ, United States) with a fixed solution flow rate of 1 ml/h. The resulting membranes were collected onto either a static aluminum foil covered steel plate (randomly oriented fibrous membranes) or a rotating aluminum foil covered steel collector (aligned fibrous membranes) with a distance of 10 cm to 15 cm between the plate and the tip

of the spinneret (**Figure 3.1**). Membranes were dried in a vacuum oven at 40 °C overnight to remove the residual solvent before further analysis.

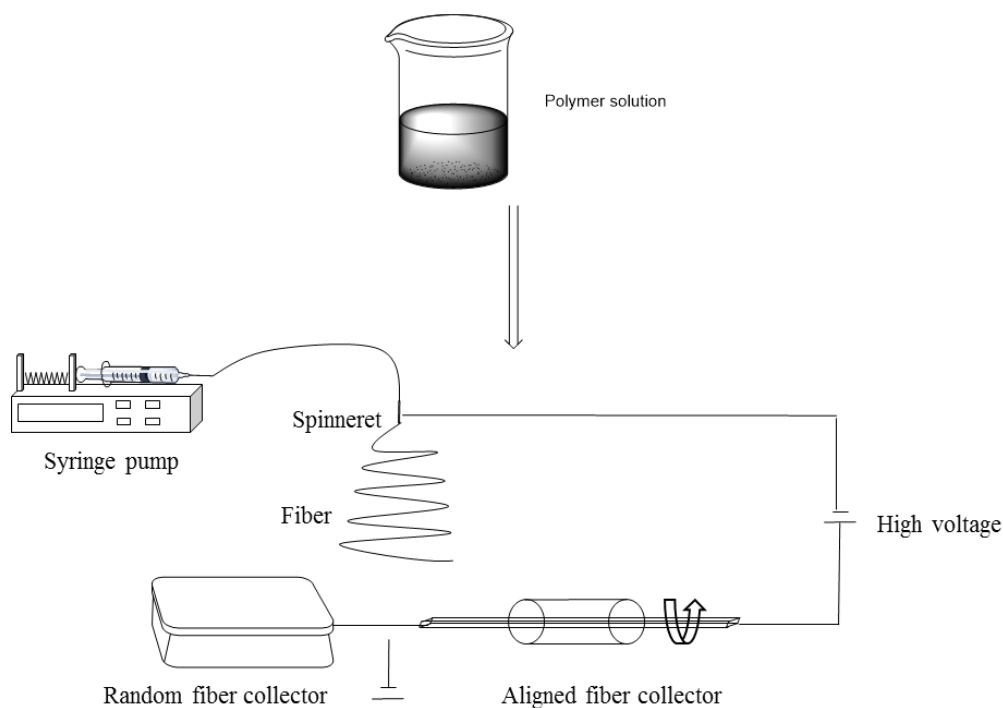


Figure 3.1 Schematic representation of electrospun solution preparation and electrospinning setup for membranes with different fibre orientation. The fibres alignment was adjusted by changing the collector type and utilized the dragging force to align the fibre bundles.

3.3.3 Characterization of polymer membranes

Random and aligned membranes of materials P1 to P4 (P1-P4-R and P1-P4-A) were taken further, to fully understand the morphology and surface properties of the obtained membranes, and also to characterize the mechanical properties.

Fibre morphology was evaluated using a scanning electron microscope (Inspect F, FEI, Netherlands), by punching a 5 mm diameter circular disc from each sample for analysis. The average fibre diameter of each disc was obtained by manually measuring the diameters of at least 100 fibres from at least three SEM images random located across the sample using Image J (ImageJ software, NIH Image, MD, U.S.A) with a

single value (mean \pm standard deviation (SD)) presented for each membrane type.

Additionally, the images were further analyzed using a Fast Fourier Transform (FFT) described previously²³⁵ to elucidate the difference in fibre arrangement presented in random and aligned fibre images. In brief, images were first transformed into 8-bit images and then thresholded to achieve a sharp contrast. A frequency distribution histogram from the transformed image was then established using the directionality plugin in Fiji/ImageJ (ImageJ software, NIH Image, MD, U.S.A.)²³⁶, denoting the number of fibres in each direction. The program divided the images into small squares and evaluated the Fourier power for each angle to compute the spectra²³⁷. Spectra were reconstructed in Origin 9.0 (OriginLab, Northampton, MA) via reporting the data from -90 to 90 degree in bins of two degrees with zero degree denoting the mean fibre orientation.

Surface wettability was also determined via water contact angle measurements (WCA) taken for a drop of purified water deposited onto the samples using a micro-pipette. A small rectangle sample (20 mm * 30 mm) was cut from each membrane, and WCAs were measured with a Kruss DSA100 (Hamburg, Germany) followed by image analysis of the sessile drop using the inbuilt DSA 1.9 software. For each rectangular test sample, at least five measurements were taken at different locations across the surface area.

3.3.4 The uniaxial tensile tests

All mechanical testing was performed at room temperature using an Instron 3365 (Instron Co, Norwood, MA, USA) materials testing system, equipped with a 100 N load cell. Rectangular samples (~ 40 mm * 10 mm) were prepared manually from P1-

P4 membranes, ensuring that samples both with and against fibre direction were prepared from aligned materials. The thickness of each individually prepared sample was measured using a light microscope and the mean value used for cross-sectional area calculations. Each test specimen was mounted vertically between the pneumatic grips at a gauge length of roughly 20 mm, after which a 0.1 N preload was applied to ensure a consistent starting condition and then the test gauge length was measured. For pull to failure tests, samples were stretched at 1 % strain s⁻¹ and the ultimate tensile stress and strain and maximum modulus were obtained from the calculated stress-strain curves. A continual modulus curve was also drawn, calculated over every five points of the stress-strain curve, from which a maximum value was found. At least six samples were tested for each type of membrane and fibre orientation condition, and mean values presented here.

3.3.5 Cyclic loading tests

The cyclic load response of samples was also investigated utilizing cyclic loading tests. Samples were prepared, secured in grips and subjected to a tare load as previously described, after which ten loading-unloading cycles were applied, straining the samples along the fibre direction to 30 % strain (n=6 per strain condition), followed by a pull to failure test at 1 % strain s⁻¹ 238-239. The ultimate tensile stress and strain and maximum modulus were obtained from the pull to failure tests, and hysteresis was determined from the loading cycles. The values were averaged over six repeat tests.

3.3.6 Cyclic recovery tests

The recoverability of aligned samples was also investigated employing P4-A samples as representative material. Samples were prepared, secured in grips and subjected to a tare load as previously described, after which ten loading-unloading cycles were applied, straining the samples along the fibre direction to either 10 %, 20 % and 30 % strain (n=2 per strain condition). Samples were then returned to 0 % strain for 30 minutes or 24 hours at room temperature to allow for any recovery, after which they were subjected to a further 10 loading-unloading cycles to the same peak strain, followed by a pull to failure test at 1 % strain s⁻¹. The ultimate tensile stress and strain and maximum modulus were obtained from the pull to failure test, and hysteresis and percentage recovery from the loading cycles.

A further random and aligned P4 specimen were subjected to ten loading cycles to 30 % strain, then prepared for SEM images to compare fibre dimensions and alignment after the cyclic loading. Three images were taken of the micro-scale surface morphology of each membrane, with a representative image of each shown here. The diameters of 35 fibres in each image were manually analyzed and data combined to give a frequency distribution of fibre diameter for each group. All fibres orientation in three images were analyzed using Image J and data combined to give an angle plot of fibre orientation.

3.3.7 Statistical Analyses

All data were analyzed using statistical analysis software GraphPad Prism 6.0 (GraphPad Software, San Diego, CA) and expressed as mean ± SD. All the mechanical results were smoothed using Curve Fitting Toolbox™ (MATLAB and Statistics

Toolbox Release 2017b, The Math Works, Inc., Natick, Massachusetts, United States.) to remove noise from the data before further processing. Due to the non-normal distribution of the mechanical data, Kruskal-Wallis tests were performed followed by Dunn's tests for all mechanical data analysis, with $p < 0.05$ considered significant.

3.4 Results and discussion

3.4.1 Optimization of electrospinning condition

Chloroform (CHCl_3) and dimethylformamide(DMF) were chosen as the solvent for electrospinning of PCL according to a procedure reported before²⁴⁰. In order to construct membranes with smooth and uniform fibre bundles, various solvent ratios and polymer concentrations were investigated before selecting electrospun conditions.

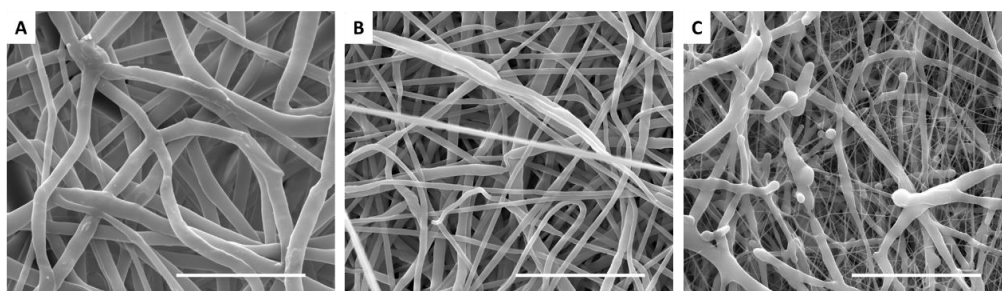


Figure 3.2 A typical SEM image of PCL electrospun fibres in (A) 1:1; (B) 1:3 and (C) 1:5; weight ratio CHCl_3 : DMF solutions; Images show the influence of solvent volatility and dielectric constant on fibre form; Scale bar represents 10 μm in all pictures.

Firstly, CHCl_3 : DMF ratio was optimized, while the polymer concentration was kept constant at 20 wt. %. Figure 3.2 shows the typical images of electrospun PCL

membranes using different solvent ratios. When chloroform reached more than 50 wt. % in the final solution, it led to blockage of the spinneret, thus solvent ratios were set up to a maximum of 50 % chloroform. The fibres tend to possess thicker diameters at higher chloroform ratios (Figure 3.2 (A)) due to the low dielectric constant and poor extensibility of the polymer solution under the same voltage⁹⁸. With the increase of DMF fraction, thinner fibres with smooth and uniform appearance were formed, while maintaining the individual 3D porous fibrous structure (Figure 3.2 (B)). However, further increase of DMF in the solvent led to the insufficient removal of the solvent before the fibre reach the collector, evidenced by the formation of very fine fibres which completely merged to create into unseparated thicker fibre bundles (Figure 3.2 (C))²⁴¹. According to the results, CHCl₃: DMF weight ratio was fixed as 1:3 for all following electrospinning.

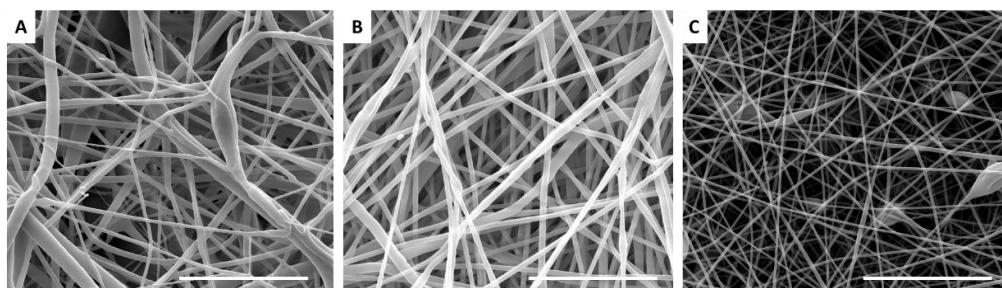


Figure 3.3 A typical SEM image of electrospun fibres of (A) 15 wt. %; (B) 20 wt. % and (C) 25 % wt. % PCL in CHCl₃ and DMF mixture; Low concentration led to non-uniformed fibres while high concentration led to beaded fibres; Scale bar represents 10 μm in all pictures.

After finalizing the suitable solvent ratio, polymer concentration was further explored to determine the appropriate polymer amount for the manufacture of identical bead-free fibres. When PCL concentration was below 15 wt. %, fibres were emitted with droplets due to the lack of entanglement within the solution⁹⁷. Thus 15 wt. %, 20 wt. % and 25 wt. % PCL solutions were prepared to evaluate the appropriate polymer

concentration. Figure 3.3 shows typical SEM images of fibre bundles at different polymer concentrations. Figure 3.3 (A) shows the lower polymer ratio, in fibres with various diameter were generated because the insufficiency of chain entanglement led to the creation of non-uniformed fibres. When the polymer concentration was elevated to 20 wt. %, straight, uniform fibres were produced with smooth surface morphology (Figure 3.3 (B)). Further increase of polymer concentration leads to the inability of fibres to elongate within the electric field, and subsequently, the formation of beaded fibres (Figure 3.3 (C)). Based on these results, 20 % polymer solutions were applied to fabricate the rest membranes.

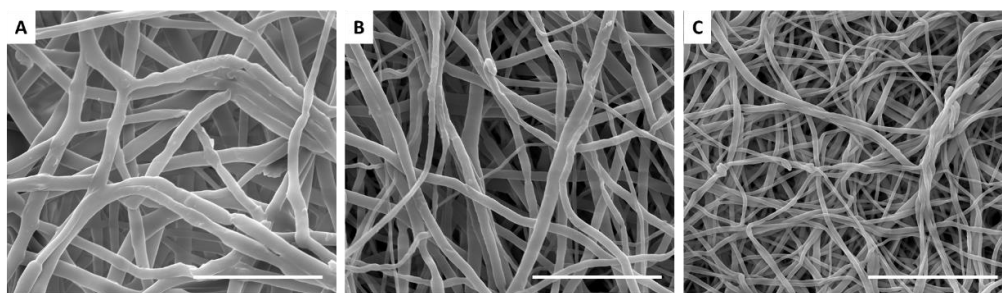


Figure 3.4 Typical SEM images of electrospun fibres at (A) 20 KV; (B) 25 KV and (C) 30 KV using 20% wt .% PCL solution; Higher voltage generated thinner fibres bundles; Scale bar represents 10 μm in all pictures.

Applied voltage also had a significant influence on fibre diameters⁹⁷ as shown in Figure 3.4. It can be clearly observed that with the increase in voltage (Figure 3.4 from A to C), there is a clear decrease in fibre diameters. However, all the fibres possessed a smooth surface with uniform fibre diameter, demonstrating simple control over fibre diameter by adjusting the applied voltage.

Another advancement electrospinning provides is the straightforward manipulation over fibre alignment and fibre structure, allowing the fabrication of aligned fibres¹⁰⁶ and also the ability to manufacture more complex arrangements, such as core-shell fibres¹¹¹.

First fibre alignment was investigated, using a rolling collector at 2080 rpm. Considering the fibre alignment, Figure 3.5 shows a typical image of random and aligned fibre materials, with a matched fibre distribution angle plot. A notable difference in fibre distribution was witnessed between the random fibre group (Figure 3.5 (A)) and aligned fibre group (Figure 3.5 (B)). Results show effective control over fibre organization with smooth fibre appearance was achieved. Subsequently, all polymers were fabricated into both random and aligned fibres to acquire membranes with optimal mechanical properties and provide potential cell attachment stimulation via alignment.

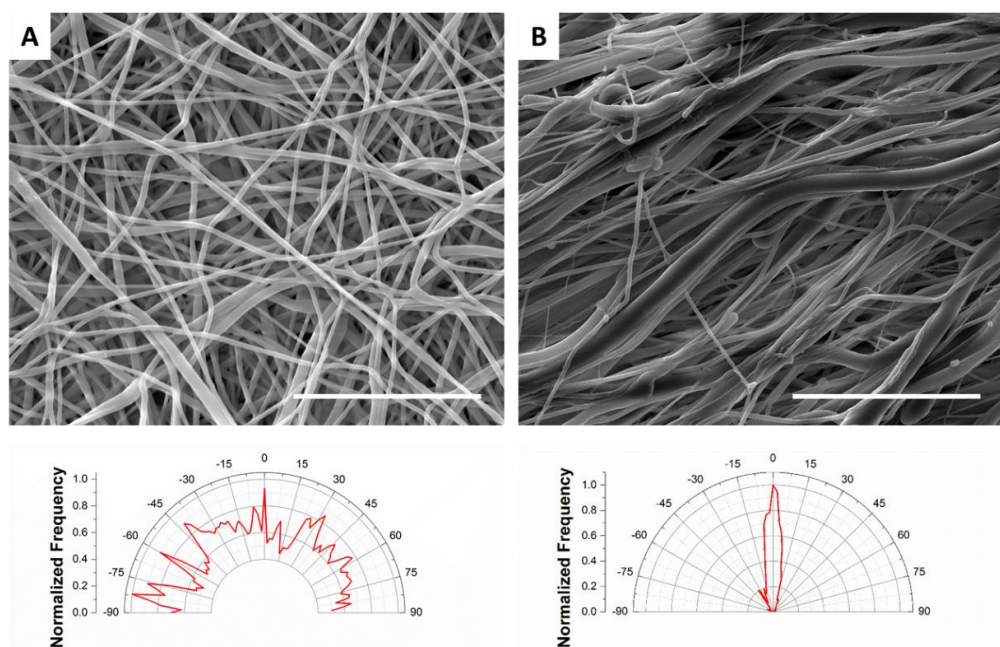


Figure 3.5 A typical SEM image of (A) random and (B) aligned PCL electrospun fibres with corresponding angle plot below; Fibre alignment has been controlled via adjusting collector type; Scale bar represents 10 μm in all pictures.

In summary, having optimized electrospinning conditions, the previously synthesized PCL-*mikto*-PS and PCL-*mikto*-PPFS were dissolved in CHCl_3 : DMF (w/w = 1:3) together with homo PCL (CapaTM 6500D) in 1:4 w/w ratios as outlined in Figure 3.6. The chemical structure of four block copolymers synthesized in chapter 2 could be

found in Figure 3.6. For the electrospinning of PCL-*mikto*-PTFSGlc, ethyl formate was employed to replace CHCl₃ due to the solubility of this polymer.

In total, three random and three aligned fibrous membranes, approximately 300mm × 200 mm were made from each sample solution and dried in a vacuum oven at 40 °C overnight to remove the residual solvent before further analysis.

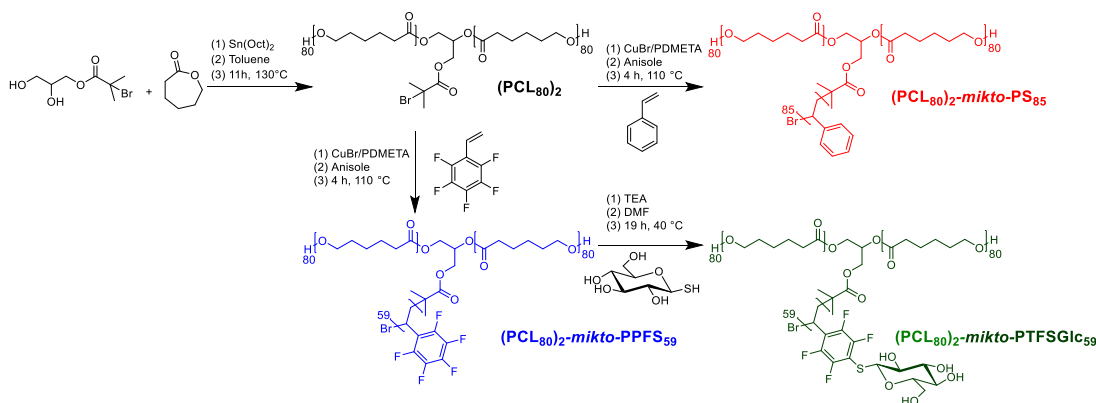


Figure 3.6 Scheme of polymer synthesis route and detailed chemical structures of each polymer.

Table 3.1 Composition of solutions for electrospun membranes.

Membrane code	Solution composition	Solvent ratio
Random P1 (P1-R) Aligned P1 (P1-A)	PCL ^a	CHCl ₃ : DMF (w/w = 1:3)
Random P2 (P2-R) Aligned P2 (P2-A)	PCL- <i>mikto</i> -PS: PCL ^a = (w/w = 1:4)	CHCl ₃ : DMF (w/w = 1:3)
Random P3 (P3-R) Aligned P3 (P3-A)	PCL- <i>mikto</i> -PPFS: PCL ^a = (w/w = 1:4)	CHCl ₃ : DMF (w/w = 1:3)
Random P4 (P4-R) Aligned P4 (P4-A)	PCL- <i>mikto</i> -PTFSGlc: PCL ^a = (w/w = 1:4)	ethyl formate: DMF (w/w = 1:3)

^a PCL was kindly provided by Perstorp Winning Formulas Corporation (Capa™ 6500D).

3.4.2 Characterization of final polymer membranes

A small disc from one membrane of each material was cut to analyze with SEM in order to investigate fibre organization and characteristics, whilst a second sample was cut to determine hydrophobicity using water contact angle measurements.

All membranes appeared to possess a smooth finish when viewed at the macro-scale, while individual fibre arrangement was visible at the microscale with scanning electron microscope. Three images were taken at the micro-scale to investigate fibre morphology of each membrane, with a representative image of each shown in Figure 3.7.

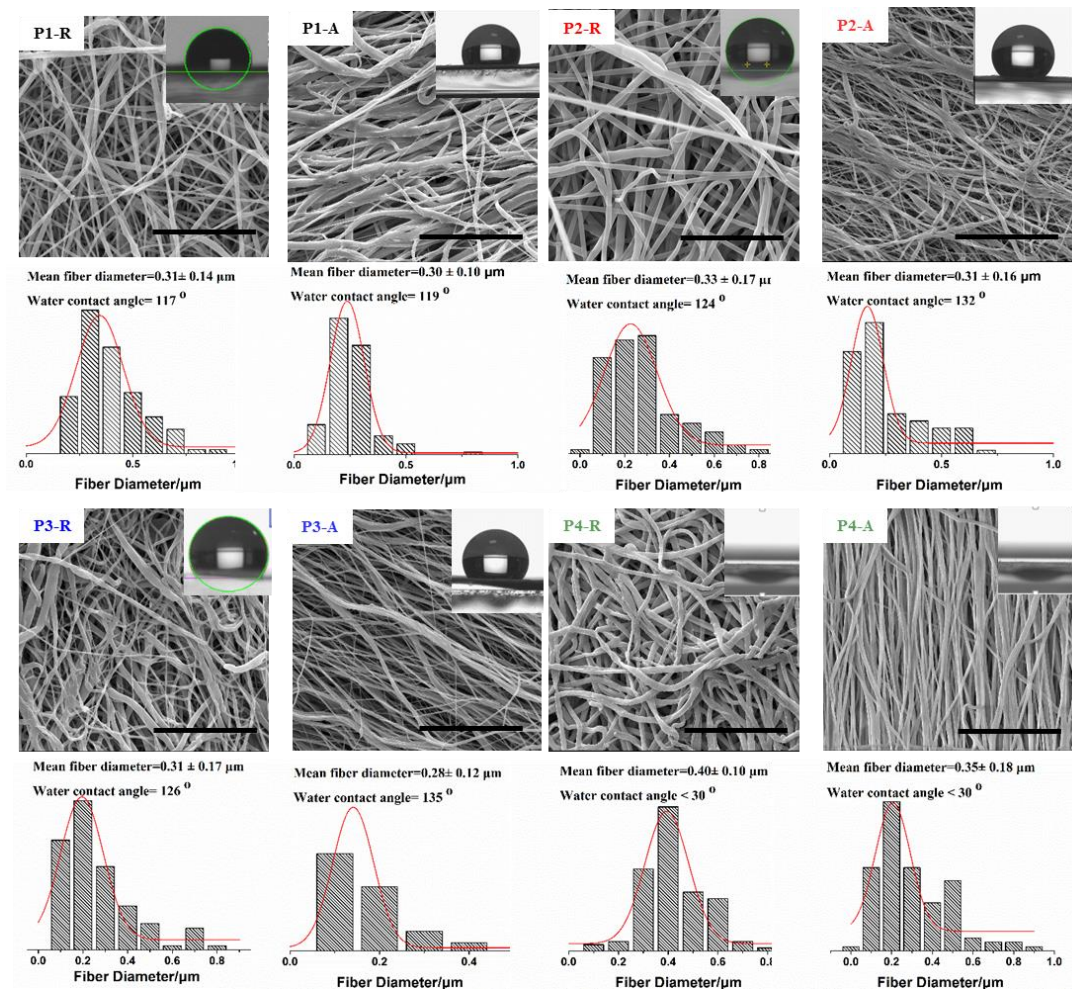


Figure 3.7 A typical SEM image of both random and aligned polymer membranes, with inset showing a matched typical water contact angle result. Mean fibre diameter and water contact angle across all analyzed samples are presented with fibre diameter distribution graph combining all analyzed fibres. Scale bar represents $10 \mu\text{m}$ in all pictures. All fibres possess a smooth surface with slightly thinner fibres within aligned fibres systems.

Mean fibre diameter, calculated across all images for a particular membrane material shows a range from $0.2\text{-}0.4 \mu\text{m}$ (Figure 3.8), with the small variability between materials likely attributed to the different solubility of each polymer type in the co-solvent²⁴². Aligned fibre membranes consistently showed a trend towards smaller fibre diameters when compared with their randomly distributed counterparts, likely attributable to the dragging force of the collector (Figure 3.8 (a)).

Water contact angle was measured at five locations across each sample. Overall, data demonstrated that while mixing block copolymers with homo PCL did not

significantly influence the average diameter of fibres in electrospun membranes, it did change the hydrophilicity of the surface significantly (Figure 3.8). Whilst the incorporation of a hydrophobic block (PS or PPFs) created a surface which behaves slightly more hydrophobically (P2-P3), the incorporation of hydrophilic glycopolymer made the surface more significantly hydrophilic, such that the WCA was reduced to zero (P4). Aligning fibres within membranes resulted in an insignificant but consistent increase in water contact angle relative to the corresponding randomly oriented fibres materials for each hydrophobic membrane only, likely a result of reduced spacing between fibres in aligned materials. Glycopolymer based membranes retained their hydrophilicity regardless of fibre arrangement.

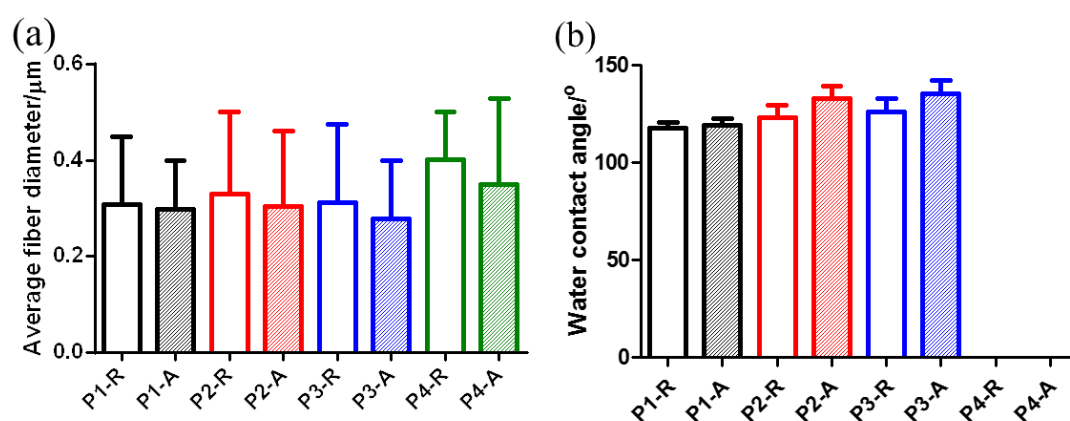


Figure 3.8 (a) Fibres diameters and (b) water contact angle of different membranes. Changes in chemical composition did not alter fibre diameter significantly, but dramatically affected the surface hydrophobicity.

3.4.3 Mechanical properties of electrospun membranes

Six randomly oriented and twelve aligned fibre samples were cut from the electrospun membranes, for the quasi-static pull to failure tests, with aligned fibrous membranes pulled with and against the fibre direction (n=6 per test condition).

Mechanical test data highlighted no significant differences in the mechanical

properties of the four membrane materials, but a significant, order of magnitude increase in the failure properties and modulus of aligned fibres relative to their randomly oriented counterparts when loaded in the fibre direction (Figure 3.9 (a-d), Figure 3.10, and Figure 3.11). Trends in sample specific and material mechanical parameters were consistent for all membrane materials, indicating consistent fibre arrangement and spacing between test groups.

Increased stress and reduced strain are commonly seen in membranes if comparing random and aligned fibres, as the large majority of fibres are directly loaded and directly recruited to resist the applied strain in the aligned instance, meaning there is less space for fibre movement, relative to the situation in a randomly oriented membrane.

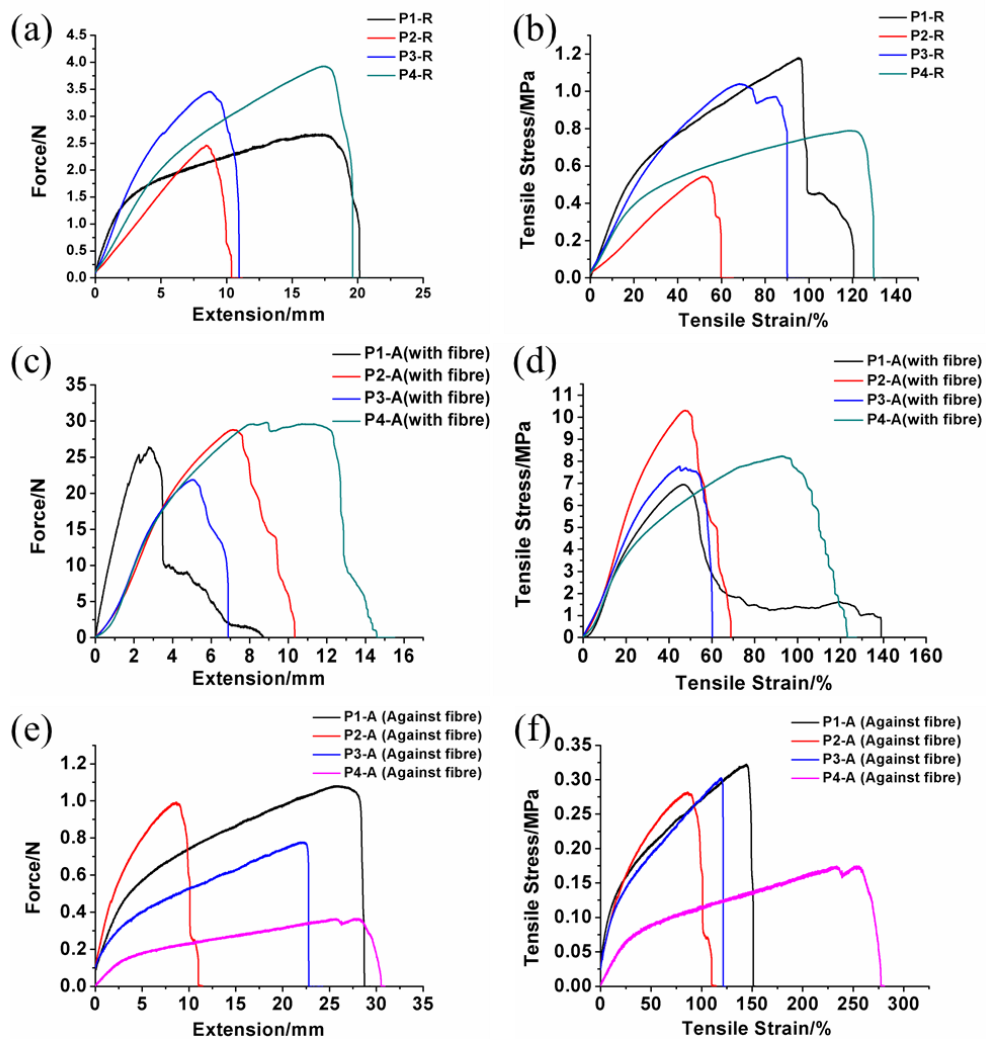


Figure 3.9 Representative pull to failure curves for both random (a-b) and aligned polymer membranes (P1-P4; with (c-d) and against the fibre (e-f)). All the samples were pulled to failure at 1 % strain/s. Note the substantial variation of scale on the Y-axis denoted the substantially improved failure properties for aligned fibre systems.

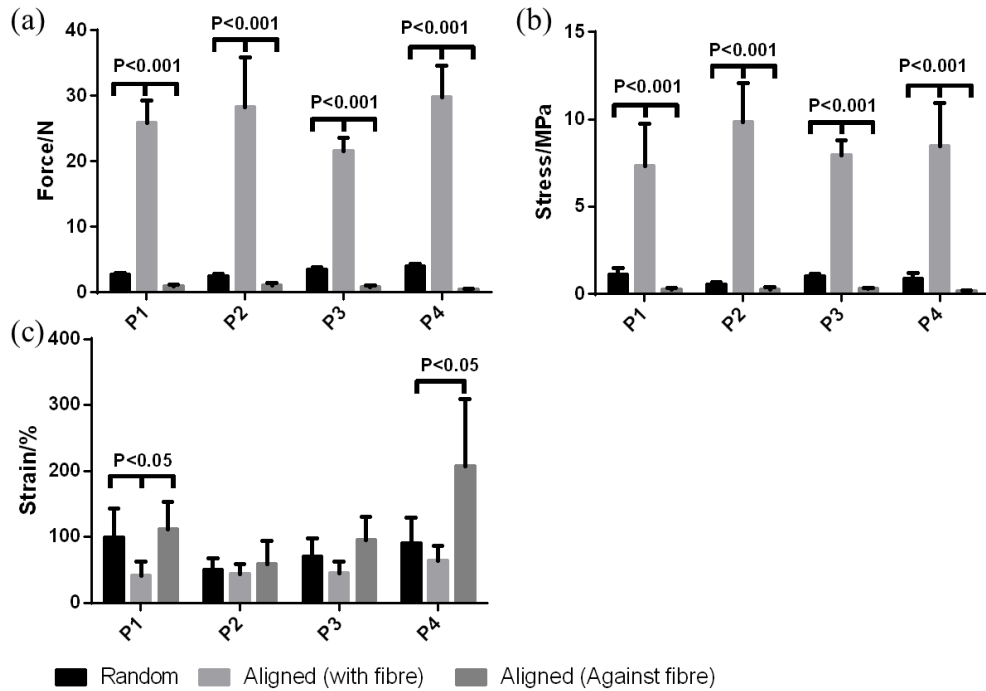


Figure 3.10 Comparison of mean (a) force, (b) stress and (c) strain between all random and aligned polymer membranes groups. Significantly higher failure properties and slightly decreased strain were observed when samples were loaded with the fibre direction.

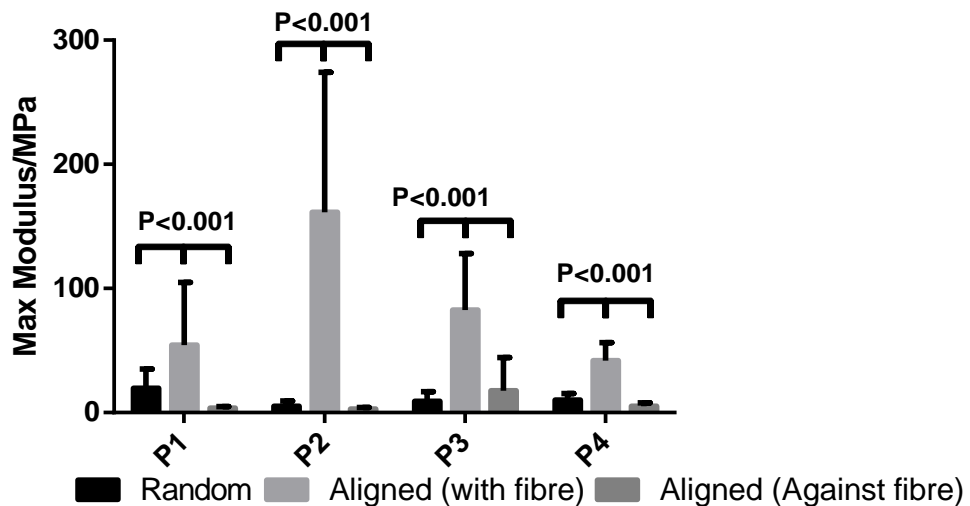


Figure 3.11 Comparison graphs of maximum modulus between all random and aligned polymer membranes groups. Significant higher stiffness was witnessed when loaded with fibre direction compared with the rest groups.

It was also notable that a clear decrease in the failure properties and modulus of aligned fibres loaded against the fibre direction was evident, relative to the random fibres, and aligned fibres loaded with the fibre direction (Figure 3.9 and Figure 3.10 and Figure 3.11) caused by the lower amount of fibres involved in withstanding the load during the tensile tests.

Membranes were further explored to ascertain their elastic, plastic and time-dependent parameters, and capacity to manage repeated cyclic loading, as required in many biological applications. Samples were subjected to ten cycles to 30 % strain before a pull to failure test.

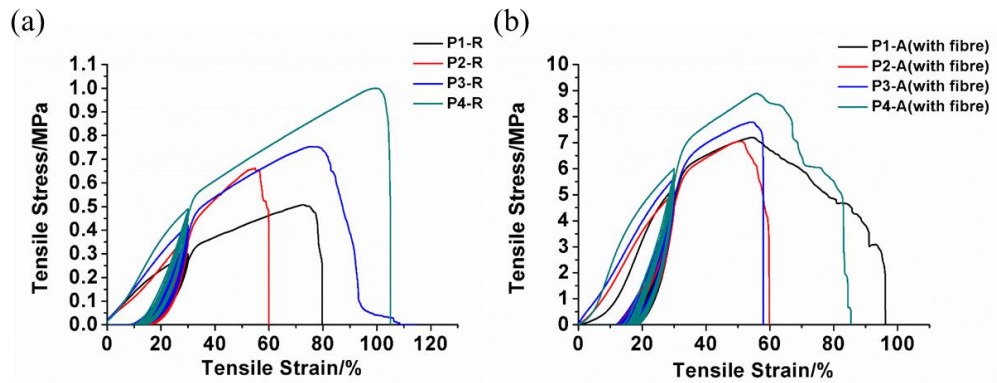


Figure 3.12 Representative cyclic loading curves for both random and aligned polymer membranes (P1-P4). (a) Random fibre samples and (b) aligned fibre samples (loaded with the fibre direction). Note the substantial variation of scale on the Y-axis indicated the considerably higher failure properties of aligned fibre systems.

The cyclic loading curves demonstrated the Mullins effect, in that the mechanical response is irreversibly dependent on the maximum load previously encountered, with instantaneous softening occurring if the load is increased beyond its previous all-time maximum value (Figure 3.12). Concomitant with this behavior, most plastic deformation and energy loss were observed within the first cycle (93% deformation and 71 % hysteresis).

Importantly, materials showed a stable mechanical state after the first loading cycle (Figure 3.12), showing promise for producing future materials with consistent mechanical behavior. ‘Plastic-rubber’ behavior is quite common for PCL derived materials¹⁹⁶, and occurs as the weaker bonds between fibres bundles start to rupture and lead to the softening of the materials during the first cycle. However, once broken the primary stronger bonds govern response, and instantaneous softening will appear again if the load is increased beyond its previous all-time maximum value, which causes the break of more bonds.

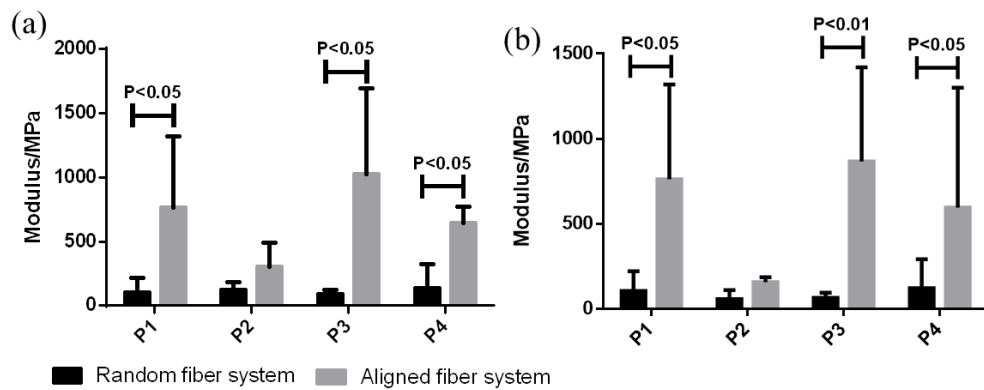


Figure 3.13 Comparison graphs of the maximum modulus (a) with cycle 1 and (b) without cycle 1 between all random and aligned polymer membranes groups. Notable higher stiffness was observed when loaded with fibre direction compared with the rest groups and a higher maximum modulus evident after the first loading cycle.

Meanwhile, in line with the results from pull to failure tests, there is still a significant increase in the failure properties and maximum modulus in aligned fibres relative to their randomly oriented counterparts when loaded with the fibre direction (Figure 3.12 and Figure 3.13). Nonetheless, all the membranes behave differently in the first loading cycle relative to further cycles. To understand the performance of the materials *in vivo*, which is normally under constant cyclic movement, we extracted the maximum modulus with or without the first loading cycle (Figure 3.13). It was observed that all aligned membranes maintained the same trend in modulus and

stiffness which shown stiffening after the first cycle and a stable mechanical state (Figure 3.12). It was also notable that all the aligned fibre can sustain more than 20 N force (similar to single suture strength) with 30 % strain deformation¹⁵⁸, potentially indicating the suitability of applying these materials in tendon healing.

In order to further characterize the recovery ability of these membranes, two aligned P4 membranes were prepared. Samples were subjected to ten loading cycles, then returned to the unloaded state to allow 30 minutes of recovery, before applying a further ten loading cycles and pull to failure measurements.

Results showed a similar slope to loading-unloading curves when 10%, 20 % and 30 % strain was applied (Figure 3.14 (a)). The last cycle of the first load batch was directly compared with the first cycle of the second load batch (Figure 3.14 (b) and (c)). After 30 mins recovery period, at which point data suggested, samples showed a slight recovery of plastic deformation. This small ratio of recovery could cause by the relatively increased mobility of the PCL chain above its glass transition temperature.

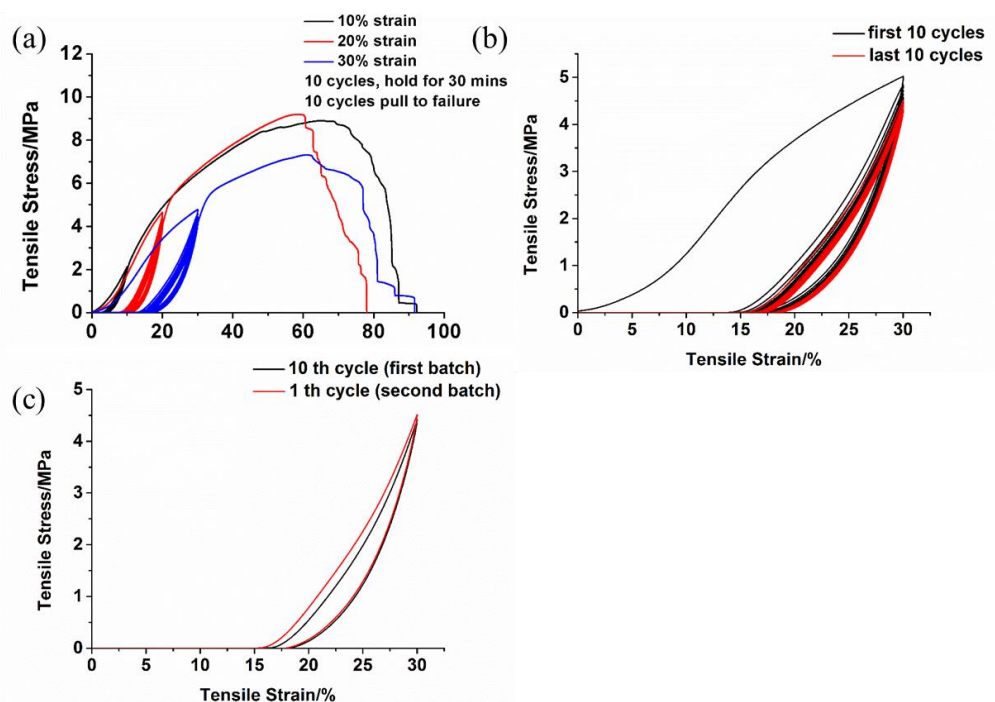


Figure 3.14 (a) Representative stress-strain curves showing cyclic loading followed by a pull to failure for aligned P4 materials. Samples were pulled to 10 %, 20 % or 30 % strain cycles and then returned to 0% strain for 30 minutes before repeating the 10 loading cycles and then pulling failure at 1 % strain s^{-1} . (b) Extracted stress-strain curves of the first and last ten cycles; (c) A direct comparison of the extracted stress-strain curve (30 % strain) of the last cycle from first loading batch and the first cycle from the second loading batch. Samples show slightly recovery of mechanical properties after 30 minutes of holding at the original position.

To further investigate the contribution of thermal behavior of the PCL chain to the recovery ability of membranes, two more samples were prepared from P4-A, and the double batches of loading cycles repeated, with a 24 hours wait period between batches (Figure 3.15). Interestingly, samples showed the ability to recover to original mechanical behavior after allowing this larger recovery period.

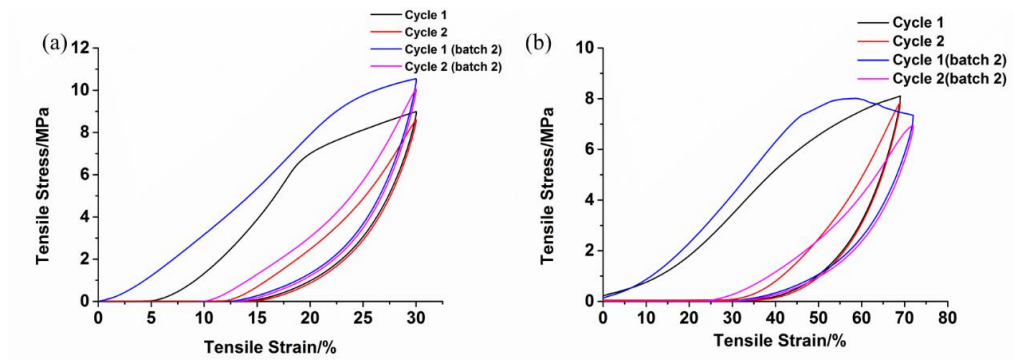


Figure 3.15 Cyclic loading curves for aligned P4 membranes, subjected to two batches of ten loading cycles, with a 24 hours recovery period between batches. Curved show stress-strain data for the first two cycles before and after recovery for two individual samples.

Further random and aligned P4 specimen was subjected to ten loading cycles to 30 % strain, then prepared for SEM images to compare fibre dimensions and alignment after the cyclic loading. Three images were taken of the micro-scale surface morphology of each membrane, with a representative image of each shown in Figure 3.16.

Figure 3.16 demonstrates no notable change in fibre orientation, but a thinning in fibre diameter after the cyclic loading. These results corresponded to the cyclic loading-unloading results obtained before, in which the random fibre maintained the lower failure force and failure stress compared with aligned fibre membranes after ten loading-unloading cycles.

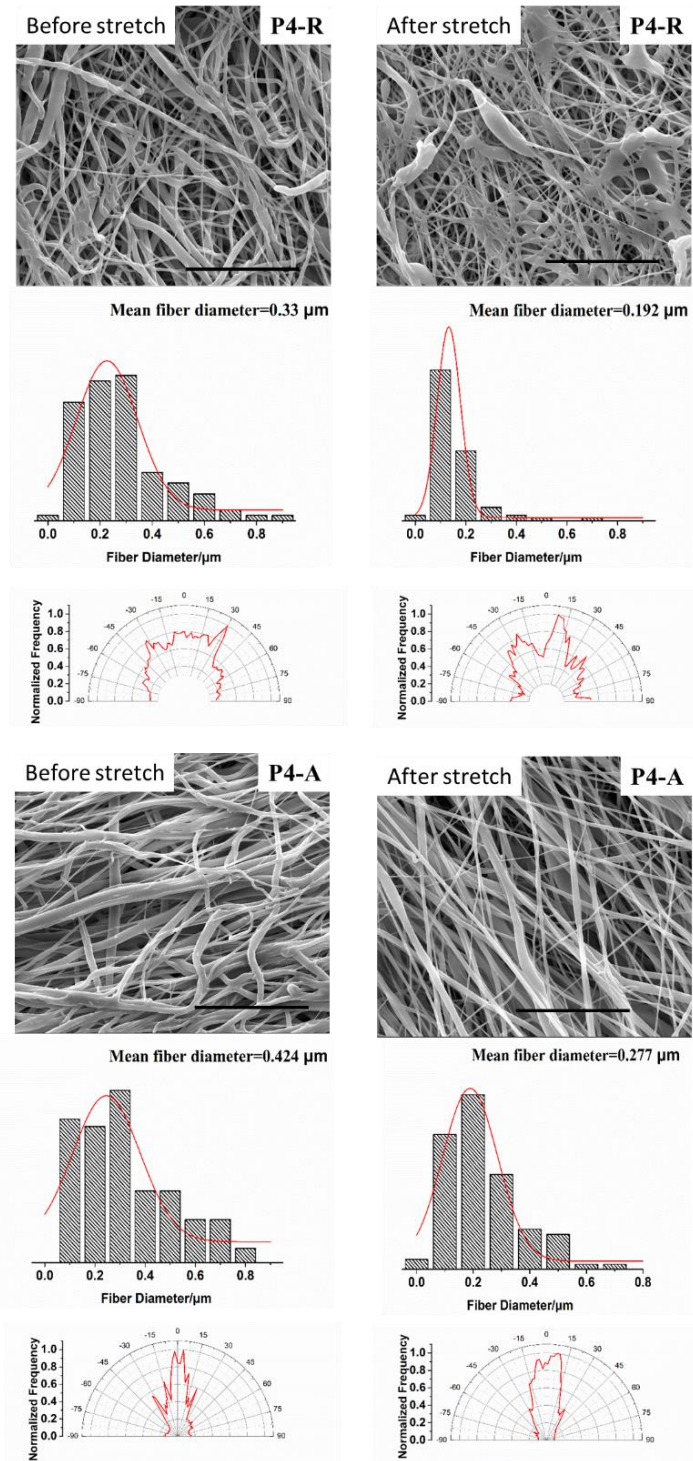


Figure 3.16 A SEM image of both a random and aligned polymer membrane, before and after being stretched to 30 % strain; A frequency distributions of fibre diameter and angle plot of fibre alignment is shown for each image. Scale bar represents 10 μm in all pictures, no notable change in fibre orientation was observed after the loading cycles.

3.6 Conclusion

The experimental work in this chapter shows the success for translation of previously synthesized polymers into 3D membrane via electrospinning.

Firstly, electrospinning conditions were optimized and control of fibre orientation achieved by using a rotary collector. Eight types of membranes were fabricated using different polymer solutions. The influence of chemical composition on the fibre structure and surface properties was characterized using SEM and WCA, and parameters like fibre diameter and fibre alignment were analyzed and compared using Image J and GraphPad. Then the mechanical properties of all membranes were then compared. For the successful application of these materials in tendon injury, which is normally under cyclic movements, the cyclic response of these materials was also evaluated. Lastly, the recoverability of these materials was ascertained using cyclic loading recovery tests.

Results showed that smooth, uniform fibre bundles were acquired after optimization. Furthermore, by arranging fibres into the same direction, the failure force and stress could be significantly improved. Aligned membrane groups also showed elevated modulus relative to random counterparts. Results highlighted a typical Mullins effect behavior of these materials. Meanwhile stable mechanical behavior and analogous fibre orientation were observed under constant cyclic movements after removal of plastic deformation. The recovery results showed the mechanical properties are fully recoverable after holding at the original position for an adequate period.

In conclusion, electrospun membranes with strong, stable and recoverable mechanical properties, which are suitable for tendon healing and other related biomedical applications, were designed and fabricated through electrospinning with different chemical compositions. In order to characterize the cell interaction between the

obtained platforms and cells, *in vitro* biological evaluation of the materials will be carried out in the next chapter.

Chapter 4. *In vitro* biological characterization using tendon cells

4.1 Introduction

In chapter 3, synthetic polymers were successfully electrospun into 3D membranes, with a uniform smooth porous 3D structure on the microscale, and the ability to recapitulate the structure observed in tendons at the microscale. The mechanical evaluation of these materials also demonstrates a strong, stable and recoverable material for biomedical applications. However, successful use of the membranes in biomedical applications also requires appropriate biocompatibility, and suitable cell affinity. It has previously been shown that hydrophobic surfaces will change the conformation of adsorbed proteins²⁴³ and thus lower cell attachment²⁴⁴⁻²⁴⁵, and there has been some early interest in adapting glycopolymers for biomedical applications^{213, 246-247}. This gives an exciting opportunity to combine the versatility of polymer chemistry with biological applications²⁴⁸⁻²⁴⁹, and it has been witnessed that glycopolymers can significantly lower the toxicity of polymer-based nanoparticles towards mammalian cells²⁵⁰⁻²⁵¹ as well as provide functional groups for cell attachment to bio-inert polymers like PCL⁶⁸. However, the interaction between tendon cells and glycopolymers has not been well investigated.

4.2 Experiment overview and hypotheses

The aim of this chapter was to investigate the biological performance of the obtained membranes (P1-P4-R and P1-P4-A) from chapter 3, investigating preliminary cell toxicity, cell attachment and cell activity.

It is hypothesized that hydrophobic membranes (P2-P3) will show low cell attachment while the glycopolymer-incorporated membrane would promote the interaction with tendon cells and facilitate the generation of 3D cell interactions in the preliminary stage. It is also hypothesized that fibre alignment will guide cell alignment specifically in the glycopolymer P4-A materials at initial cell attachment.

4.3 Methods

4.3.1 Isolation of tendon cells from bovine joint

Tendon cells were isolated from bovine extensor tendons via tissue digestion (1 U/ml Dispase and 2 mg/mL collagenase type II for 24 hours at 37 °C) were adopted as a cell source²⁵². Cells were cultured in Dulbecco's Modified Eagle Medium (DMEM) (low glucose, pyruvate) supplemented with 10% (v/v) bovine serum, 100 U/mL penicillin, 1% (v/v) nonessential amino acids, 2% (v/v) N-2-hydroxyethylpiperazine-N-2-ethane sulfonic acid (HEPES), 0.37% (w/v) sodium bicarbonate, and 1% (v/v) L-glutamine, here referred as culture medium) at 37 °C, 5% CO₂ in a humidified incubator. The culture medium was changed every 2 days and cells maintained until use at passage three, when they were harvested using trypsin-EDTA (0.25% trypsin).

4.3.2 Polymer membrane and cell preparation for *in vitro* tests

Figure 4.1 showed a schematic depiction of the preparation of cell seeded electrospun polymer samples, and the related assays that were investigated. Fifteen discs (15mm diameter) were cut from each material P1-P4-R and P1-P4-A, using a punch. All discs were sterilized by immersion in 70% ethanol overnight, and irradiated under UV light,

after which they were washed repeatedly with sterile PBS to remove residual ethanol prior to cell seeding. SEM images of membranes after sterilization could be found in appendix Figure S.1.

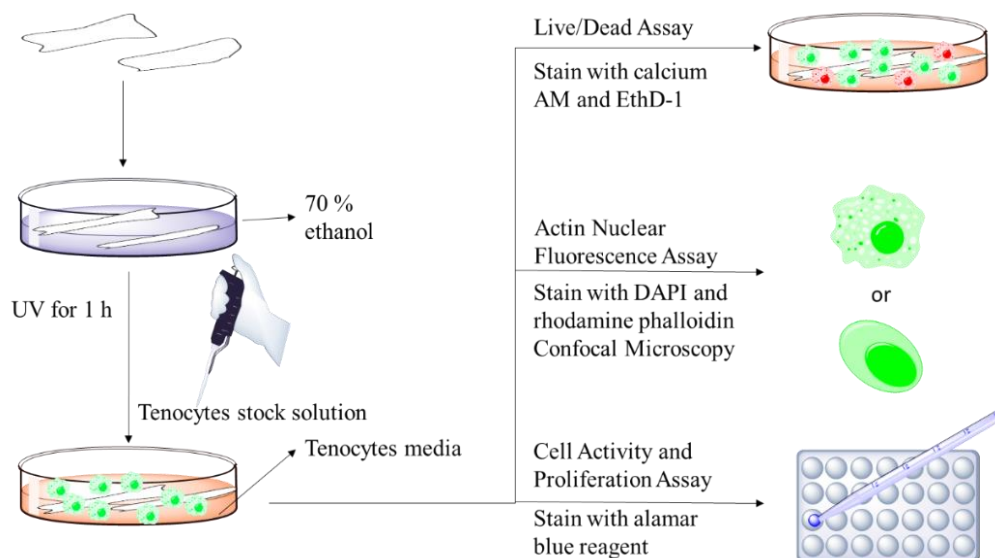


Figure 4.1 Schematic representation of samples preparation for *in vitro* cell tests using live-dead assay, cytoskeleton assay and Alamar blue assay.

4.3.3 Preliminary cell viability and affinity on membranes

Six sterilized discs of each membrane material (P1-P4-R and P1-P4-A) were placed individually, one disc per well, into the wells of a non-cell culture-treated 24-well plate, and cell solution pipetted directly onto the discs, in order to seed them at a density of 1×10^4 cells/cm². Cell seeding density was firstly optimized to achieve countable images. Six sterilized discs of PEG and six empty wells were additionally prepared in the same manner, providing negative controls. For positive controls, cells were seeded directly onto 6 wells of a standard cell culture-treated 24-well plate. Discs and controls were then incubated in complete culture medium for up to 48 hours.

The preliminary toxicity of membranes was investigated by comparing cell viability on the membranes with that on the positive control standard tissue-culture treated

plates. In addition, preliminary cell affinity with each material was investigated by comparing the percentage area covered by live cells, compared to both positive and negative controls.

Both cell viability and cell coverage were determined at 24 hours and 48 hours (three discs of each material or control well per time point). At the relevant time point, 2 μ M/ml calcein AM and 10 μ M/ml ethidium homodimer were added to each well for 30 minutes at 37 °C, and stained cells were observed under a fluorescence microscope. Both 2.5x and 10x magnification were used, and images were taken at an excitation/emission of 488/526 nm (calcein AM) and 568/612 nm (ethidium homodimer) (Leica DM4000 B LED, Heidelberg, Germany). Matched images of samples were taken at the two wavelengths, in which calcein AM produced an intense uniform green fluorescence in live cells, while ethidium homodimer produced a bright red fluorescence in dead cells. At least three pictures were taken at random locations across the surface of each disc at each time point. The number of live cells (L_m) and dead cells (D_m) on the membrane disc, and live cells (L_w) and dead cells (D_w) in the well were counted in Image J (ImageJ software, NIH Image, MD, U.S.A.) and preliminary cell viability was calculated as a live cell ratio (Eq. 4.1).

$$\text{Live cell ratio} = \frac{L_m + L_w}{L_m + L_w + D_m + D_w} \quad \text{Eq. 4.1}$$

Cell coverage was also calculated using Image J (ImageJ software, NIH Image, MD, U.S.A.), dividing the area covered with viable cells by the whole area of interest.

The cell viability and cell affinity analyses were repeated three times, with three different sets of membranes and controls, and tendon cells from three different bovine donors.

4.3.4 *In vitro* preliminary cell adhesion and morphology assay

Six sterilized discs of each membrane material (P1-P4-R and P1-P4-A) and six media-coated glass slides (positive controls) were placed, one disc per well, into two non-cell culture-treated 24-well plates. Cell solution was pipetted directly onto the discs and glass slides, in order to seed them at a density of 4×10^4 cells/cm², and all samples incubated in complete culture medium for up to 48 hours. The cytoskeleton of cells on each electrospun membrane was compared with that of tendon cells cultured on media-coated glass slide surfaces (positive control) after 24 hour and 48 hour.

To visualize the cytoskeletal arrangement, cell coated discs and glass slides were washed twice in PBS, and then fixed in 4% paraformaldehyde for 10 minutes. After removing the fixative, cells were washed repeatedly in PBS, permeabilized with 0.1% Triton X-100 in PBS for 10 minutes, and then washed twice more in PBS. The actin cytoskeleton was then stained with Alexa Fluor 488 phalloidin (20 μ g/mL) in PBS with 1% (wt) bovine serum albumin for 30 minutes, after which, cells were washed twice in PBS and the cell nucleus stained with DAPI (1 μ g/mL) in PBS with 1%(wt) bovine serum albumin for 1 minute before a final wash in PBS. Samples were imaged under a confocal laser scanning microscope (Leica TCS SP2; Leica Microsystems, Heidelberg, Germany) at an excitation/emission of 488/526 nm (phalloidin) and 358/468 nm (DAPI). At least 3 matched pictures at each wavelength were taken for each sample at 40x magnification, and an additional picture digitally zoomed 3 times was taken, to show the morphology of a single cell.

The preliminary cytoskeletal analysis was repeated three times with three different sets of membranes and controls, and tendon cells from three different bovine donors.

4.3.5 Preliminary cell viability and morphology on aligned membranes

To ascertain the influence of fibre alignment on preliminary cell viability and cell attachment pattern, twelve sterilized discs of aligned P1-P4 materials and an additional twelve discs of the randomly oriented P1-P4 membranes were prepared in non-cell culture treated 24-well plates, and preliminary cell viability, affinity and morphology examined, as described in sections 4.3.3 and 4.3.4.

The resulting confocal images were further analyzed using a Fast Fourier Transform (FFT) described previously²³⁵ to elucidate the correlation between fibre alignment and cell orientation presented in each image. In brief, images were first transformed into 8-bit images and then thresholded to achieve a sharp contrast. A frequency distribution histogram from the transformed image was then established using the directionality plugin in Fiji/ImageJ (ImageJ software, NIH Image, MD, U.S.A.)²³⁶, denoting the number of actin and nucleus in each direction. The program divided the images into small squares and evaluated the Fourier power for each angle to compute the spectra²³⁷. Spectra were reconstructed in Origin 9.0 (OriginLab, Northampton, MA) via reporting the data from -90 to 90 degree in bins of two degrees with zero degree denoting the mean cell orientation.

The actin and nucleus angle plot of cells were compared between random and aligned fibre membranes. Both the experiments and analyses were repeated three times with tendon cells from three different bovine donors and mean data combining all three repeats presented.

4.3.6 Preliminary cell activity with the existence of different polymer-based membrane

Three sterilized discs of each membrane material (P1-P4-R) were placed, one disc per well, into a cell culture treated 24-well plate. The 12 wells with membranes plus an additional three blank wells were all seeded with cells at a density of 4×10^4 cells/cm², as previously described. Cell activity on each membrane and control well was investigated using an Alamar blue assay after 24 hours, 48 hours, and 96 hours. At the 24 hour time point, a 1/10 volume ratio of Alamar blue reagent was added to the culture media of each well, and plates returned to the incubator for another 4 h. At this point, 100 μ L of the Alamar blue media mixture was taken from each sample well and its fluorescence was detected using a Fluo Star plate reader (BMG LABTECH). At least 3 technical repeats were performed for each sample. After obtaining a reading, all media was discarded from each sample and control well, and fresh media was added, after which the plate was returned to the incubator. The same samples and controls were subjected to repeat Alamar blue assays at 48 hour and 96 hour following the same procedure, to monitor the cell activity over time. The preliminary activity of cells on membranes was displayed normalized to the activity of the control samples. The Alamar blue assay was repeated for three sets of membranes and controls, using tendon cells from three different bovine donors.

4.3.7 Statistical Analyses

Results are expressed either as mean \pm SD or box-whisker plots. The normality of the data was characterized using Shapiro-Wilk normality tests. For the live and dead assay, a one way ANOVA was performed followed by Tukey comparison of means, while for

viable cell coverage and Alamar blue analysis, due to the non-normal distribution of the data, Kruskal–Wallis tests were performed followed by Dunn’s tests using statistical analysis software GraphPad Prism 6.0 (GraphPad Software, San Diego, CA). Unless otherwise stated, $p < 0.05$ was considered significant.

4.4 Results and discussion

4.4.1 Results of preliminary cell viability and affinity on membranes

Preliminary cell viability was maintained above 60 % in all test groups for up to 48 hours of incubation (Figure 4.2 and Figure 4.3). No significant differences in viability were evident between any of the test groups, nor between test groups and the positive control, of cells cultured on tissue culture plates, indicating that membranes were non-toxic to tendon cells *in vitro*.

To characterize the effect of chemical structure on tendon cells affinity, cell number and coverage were calculated using Image J for the quantitative analysis (Figure 4.4 and Figure 4.5). As P1-P3 membranes are all hydrophobic in terms of surface wettability, PEG was chosen as hydrophilic negative control. It was notable that both the number of cells and cell coverage were significantly improved on P4 membranes relative to P1-P3 (Figure 4.4 and Figure 4.5), with coverage on P1-P3 membranes below that seen in negative controls using non-treated 24-well plates during the first 48 hours. The preliminary cell coverages on P1-P3 were also comparable to the results from hydrophilic PEG negative control, which is commonly considered a gold standard for an anti-adhesive platform²⁵³. Taken together, these data suggest that incorporating sugar molecules into a polymer, even at low percentages, can enhance its interaction with cells, while hydrophobic polymers can effectively lower cell

attachment during the initial stage.

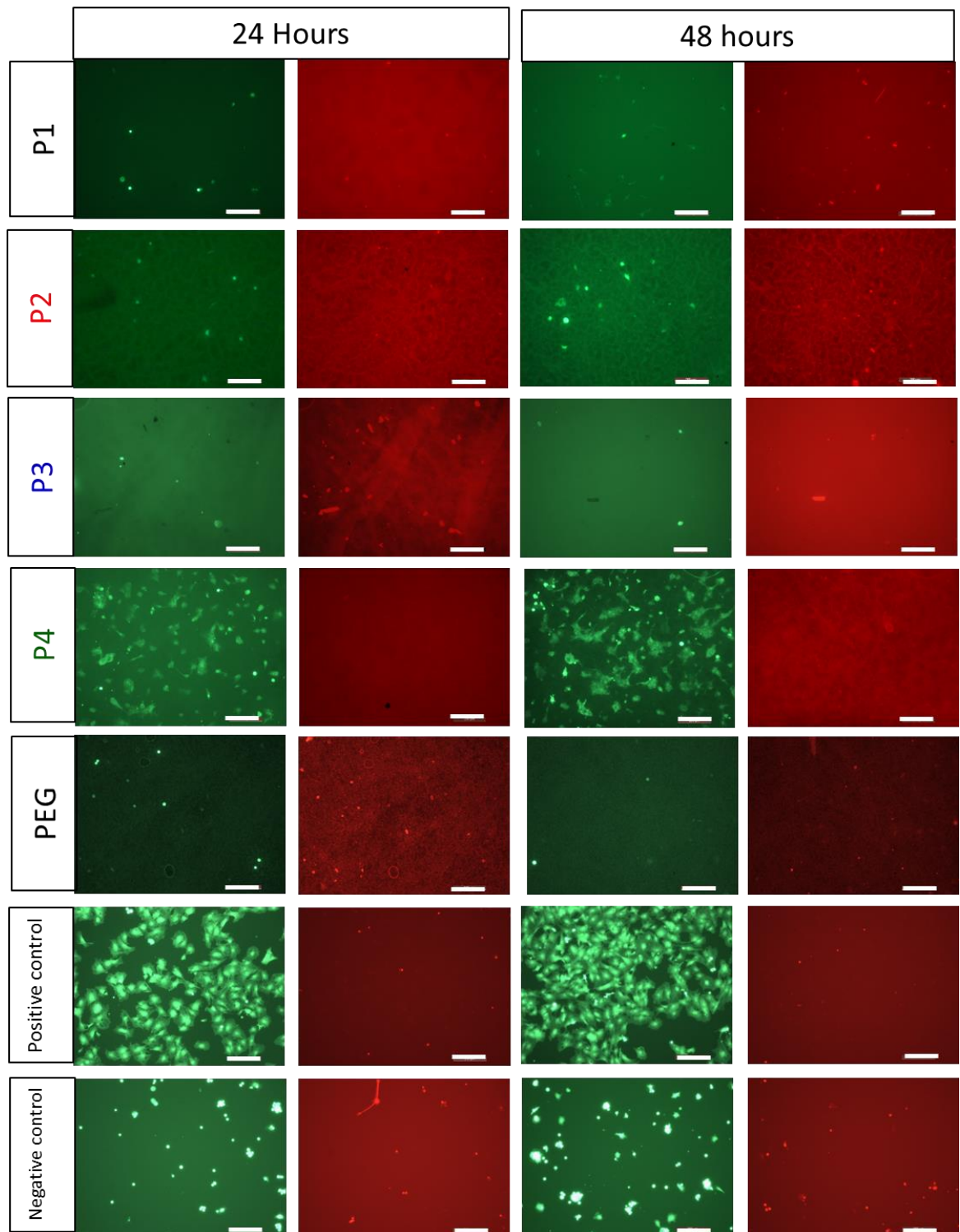


Figure 4.2 Typical images of the live-dead assay with tendon cells on random P1-P4 polymer membranes, PEG and positive and negative control surfaces after (a) 24 hours and (b) 48 hours. Viable cells are shown in green and dead cells in red. Scale bar represents 200 μm in all pictures. Significant higher number of cells could be observed on P4 membrane compared with P1-P3 groups.

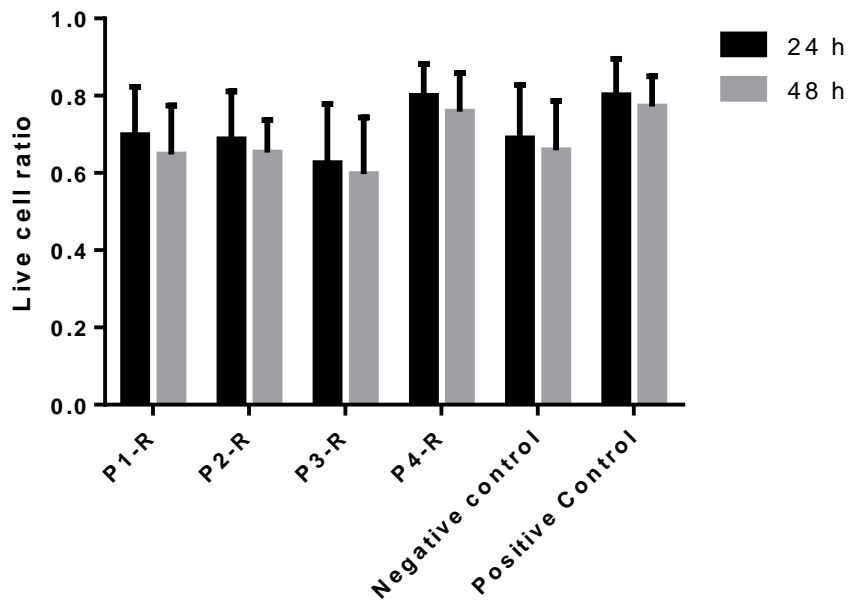


Figure 4.3 Comparison of cell viability on P1-P4 membranes and the tissue plastic controls at 24 hour and 48 hour time points. All the membranes maintain higher than 60 % cell viability after 48 hours incubation without significant different between membranes.

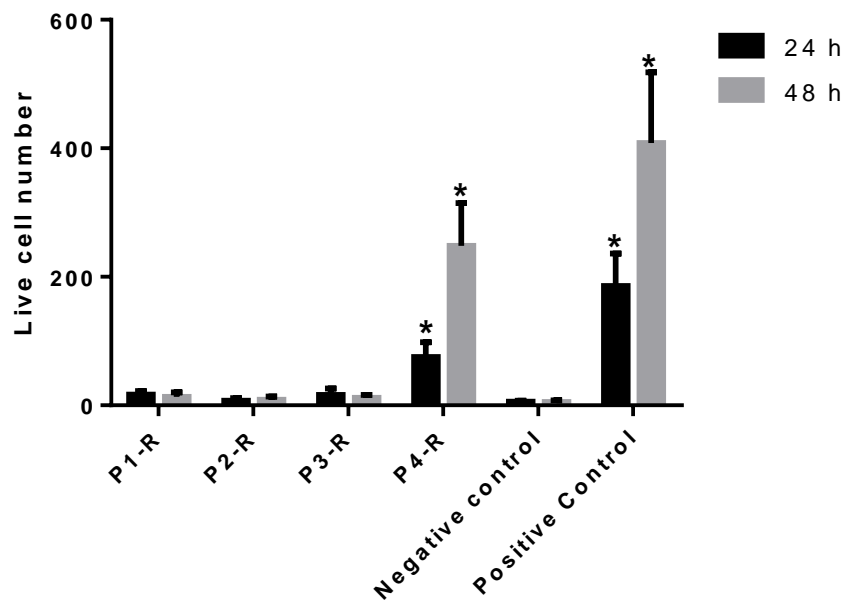


Figure 4.4 Comparison of cell number on different membranes and the tissue plastic controls at 24 hour and 48 hour time points; * represent significant the indicate group different from all other groups of data. Significant higher number of viable cells were observed on P4 membrane compared with P1-P3.

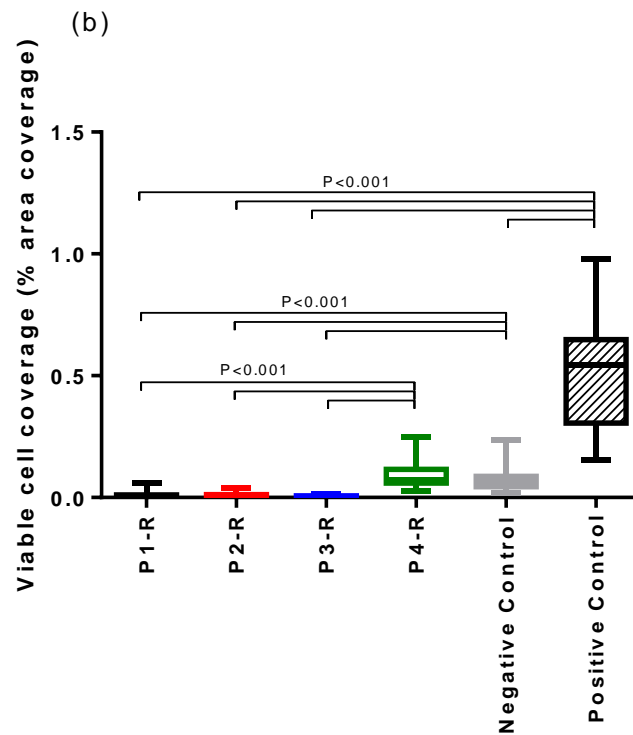
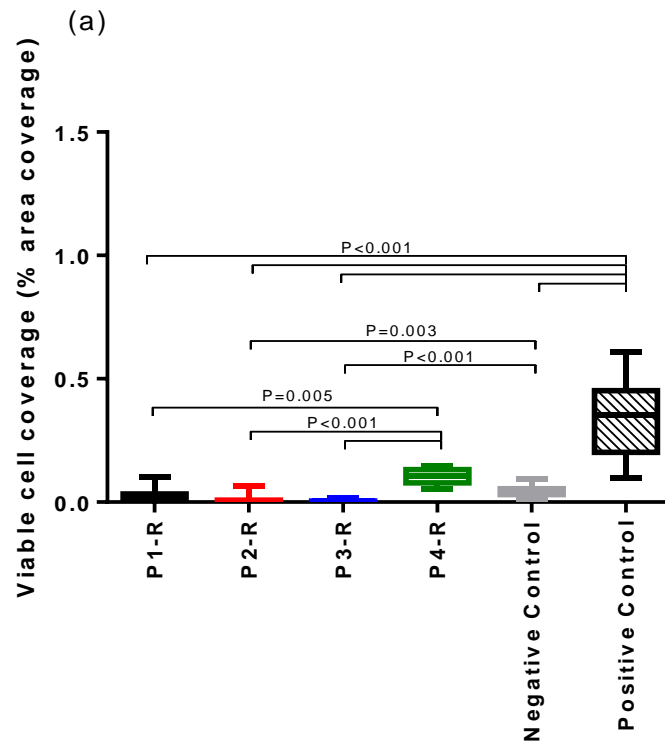


Figure 4.5 Comparison of viable cell coverage between different membranes and tissue culture plastic controls at the (a) 24 hour and (b) 48 hour time points. Significant higher of cell coverage was observed on P4 membrane compared with P1-P3.

4.4.2 *In vitro* preliminary cell adhesion and morphology

Images of cytoskeleton arrangement of cells on each material demonstrate that tendon cells on the P4-R membranes were better adhered with greater cytoskeleton tension, relative to the rounder cells on P1-P3-R membranes (Figure 4.6) during the first 48 hours. These data further support the hypothesis that the grafted sugar molecules provide the membrane with a functional group, which facilitates preliminary cell migration and cell attachment during the initial stage.

To visually assess how initial cell attachment differed between groups during the first 48 hours, images were digitally zoomed (Figure 4.6: grey scale bar images). Under higher magnification, it can be clearly observed that the cells on P4-R tend to form a well-spread 3D structure on the surface, while an isolated round cell pattern is observed on P1-P3-R.

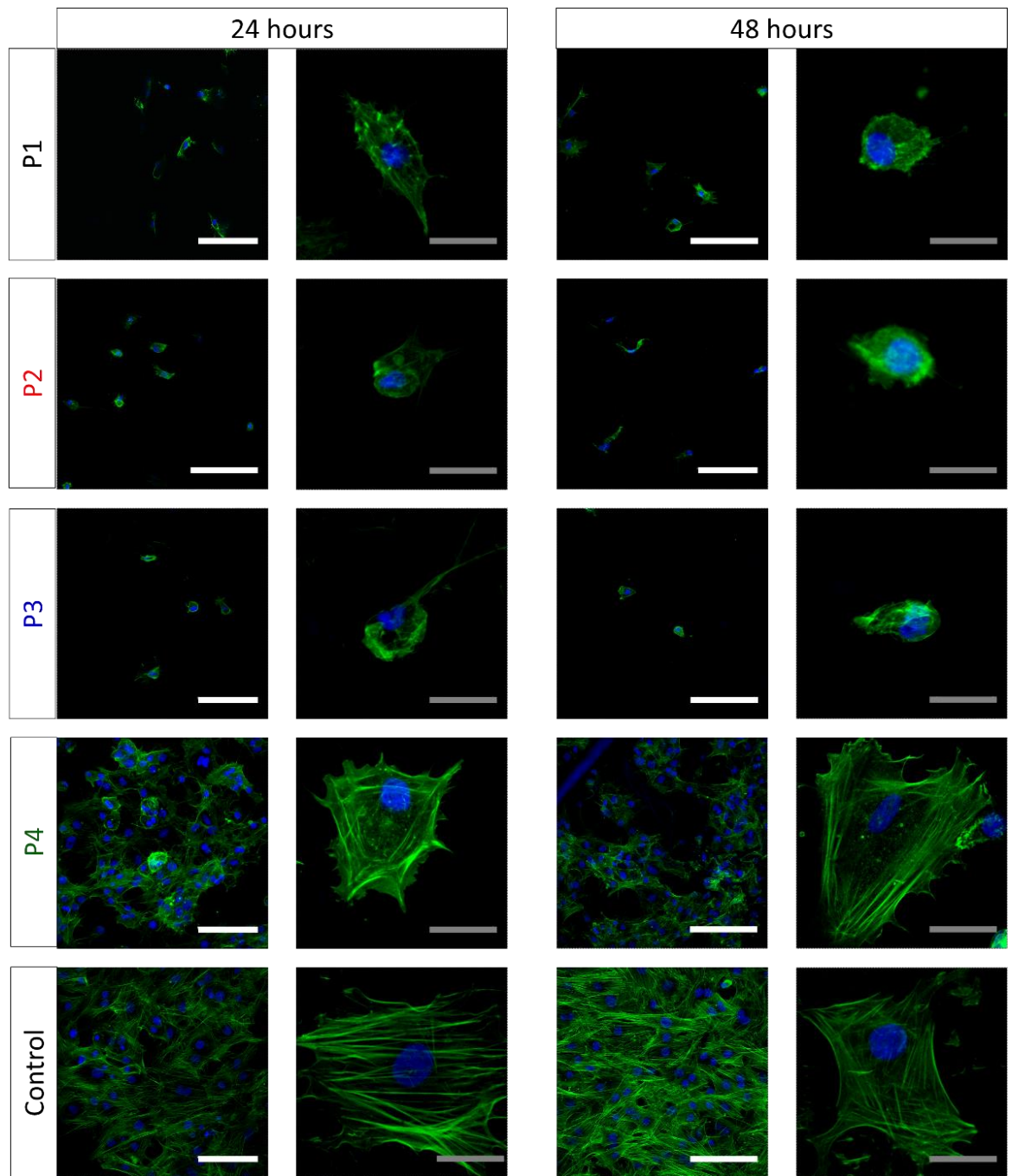


Figure 4.6 Typical images of tendon cells seeded onto each of the polymer membranes (P1 to P4) and on tissue culture plastic (control). Green staining represents the cytoskeleton while blue represents the nucleus of cells. Images show cells after 24 hours (left columns), and 48 hours (right columns). Two different magnifications are shown for each condition: the white scale bar represents 100 μm ; the grey scale bar represents 25 μm . Greater cytoskeleton tension was observed on the P4-R membrane relative to the rounder cells on P1-P3-R membranes during the first 48 hours.

4.2.3 Results of preliminary cell viability and morphology on aligned membranes

To better recapitulate native tendon, aligned fibre membranes were proposed to orientate tendon cells along the tendon long axis in our system. To further characterize the influence of the fibre alignment on preliminary cell toxicity and initial attachment, twelve more samples were prepared using aligned fibre membranes (Figure 4.7 and Figure 4.8). In line with results on random fibre membranes, cell viability was maintained above 60 % in all groups regardless of fibre orientation (Figure 4.3 and Figure 4.9). As shown previously, incorporating sugar molecules into the polymer, even at low percentages, can enhance its interaction with cells and show a tendency towards higher cell viability (Figure 4.9) during the first 48 hours. In further note, in line with our previous experiments, the number of cells was significantly improved on the aligned sugar-incorporating P4 membranes relative to the P1-P3 membranes (Figure 4.7), while fibre organization did not influence typical cell coverage on a surface, it did influence cell organization, with images consistently demonstrating that cells aligned with and spread along the fibres in the aligned membranes (Figure 4.7 and Figure 4.8). It was proved the alignment can stimulate cell differentiation and function through the micro mechanics generated by the fibres, which potentially could be used to activate cells function²³¹. Additionally, after the degradation of the membranes, the collagen fibres cell synthesized could potentially arranged into the same direction and help to improve the healed tendon mechanics.

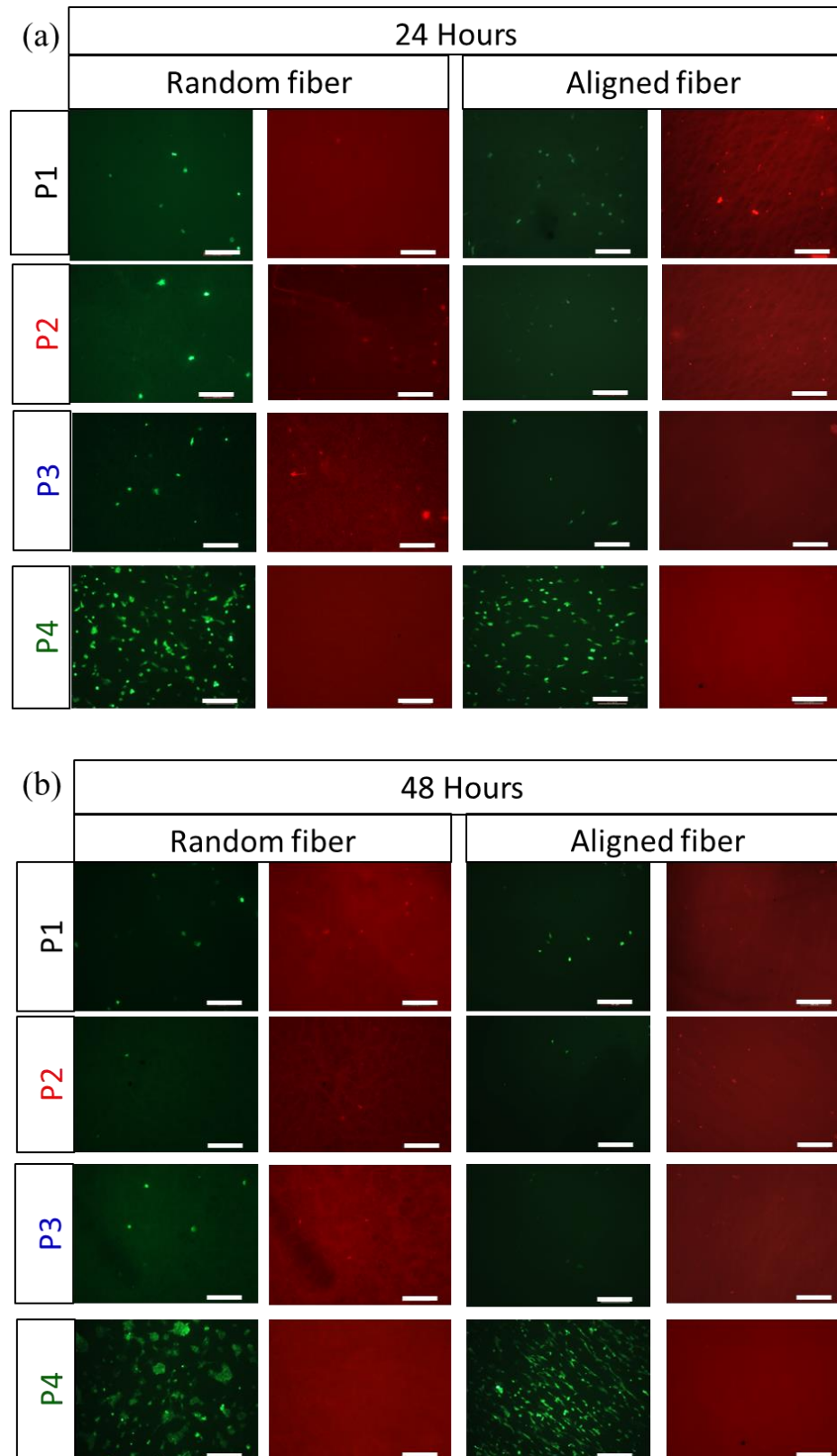


Figure 4.7 Live/dead assay of tendon cells on random and aligned P1-P4 polymer membranes after (a) 24 hours and (b) 48 hours. Viable cells are shown in green and dead cells in red. Scale bar represents 200 μm in all pictures. Significant higher number of cells could be observed on P4 membrane with different cell attach pattern on random and aligned fibres.

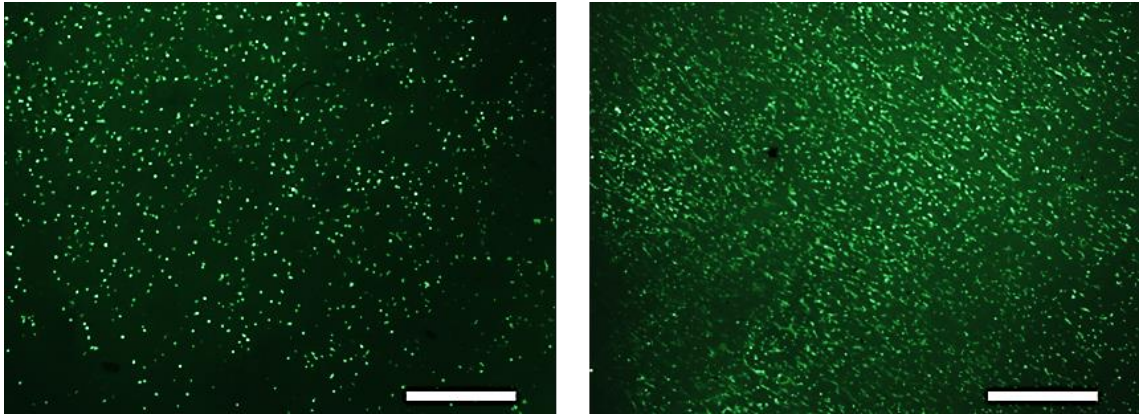


Figure 4.8 Live tendon cells on (a) random and (b) aligned P4 membranes at 2.5 magnification. Scale bar represents 1 mm in all pictures. Different initial cell attachment pattern was observed at low magnification.

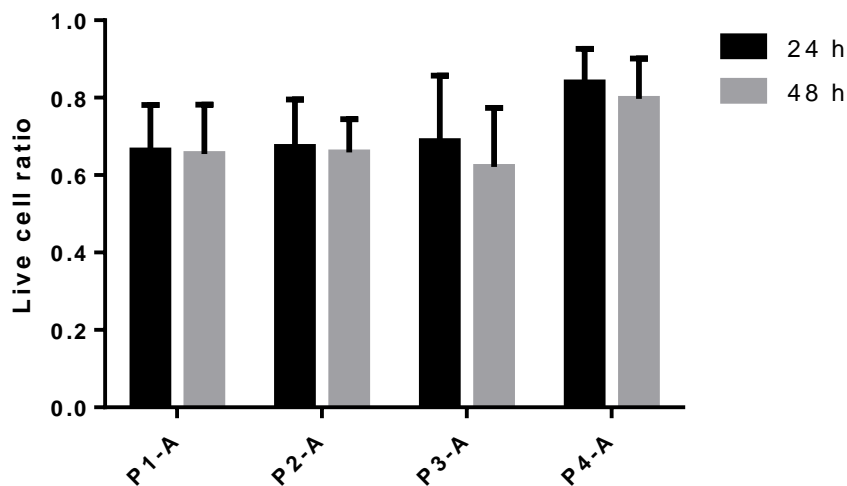


Figure 4.9 Comparison of preliminary cell viability across aligned P1-P4 membranes, at 24 hour and 48 hour time points. All the membranes maintain higher than 60 % cell viability after 48 hours incubation without significant different between membranes.

Cell morphology also differed between aligned and random materials, but only for P4 (Figure 4.10 and Figure 4.11). The cells form clusters, which are randomly distributed on the random P4 group, with the nucleus evenly oriented evenly in each direction. On the other hand, the cells appear aligned and stretched along the fibre direction in the aligned fibre systems, looking more similar to cell pattern seen within tendons.

To further visually examine cell attachment between different groups, images were digitally zoomed indicating elongation of the cytoskeleton in the fibre direction. Subsequent quantitative analysis of cell alignment was carried using Image J, with the histogram data showing that both the cytoskeleton and nucleus orientation clearly exhibit a Gaussian distribution, compared to their random arrangement on the random fibre systems (Figure 4.12). As discussed before, there is a significant difference in cell attachment after incorporation of sugar moieties into the membranes. It has been proven that the glycopolymer interacts with cells ²⁵⁴⁻²⁵⁵ and alignment of fibres has here been shown to translate into the aligned pathway for efficient control over cell attachment. As mentioned before, this alignment showed in Figure 4.12 could stimulate cell differentiation and function through the micro mechanics generated by the fibres.

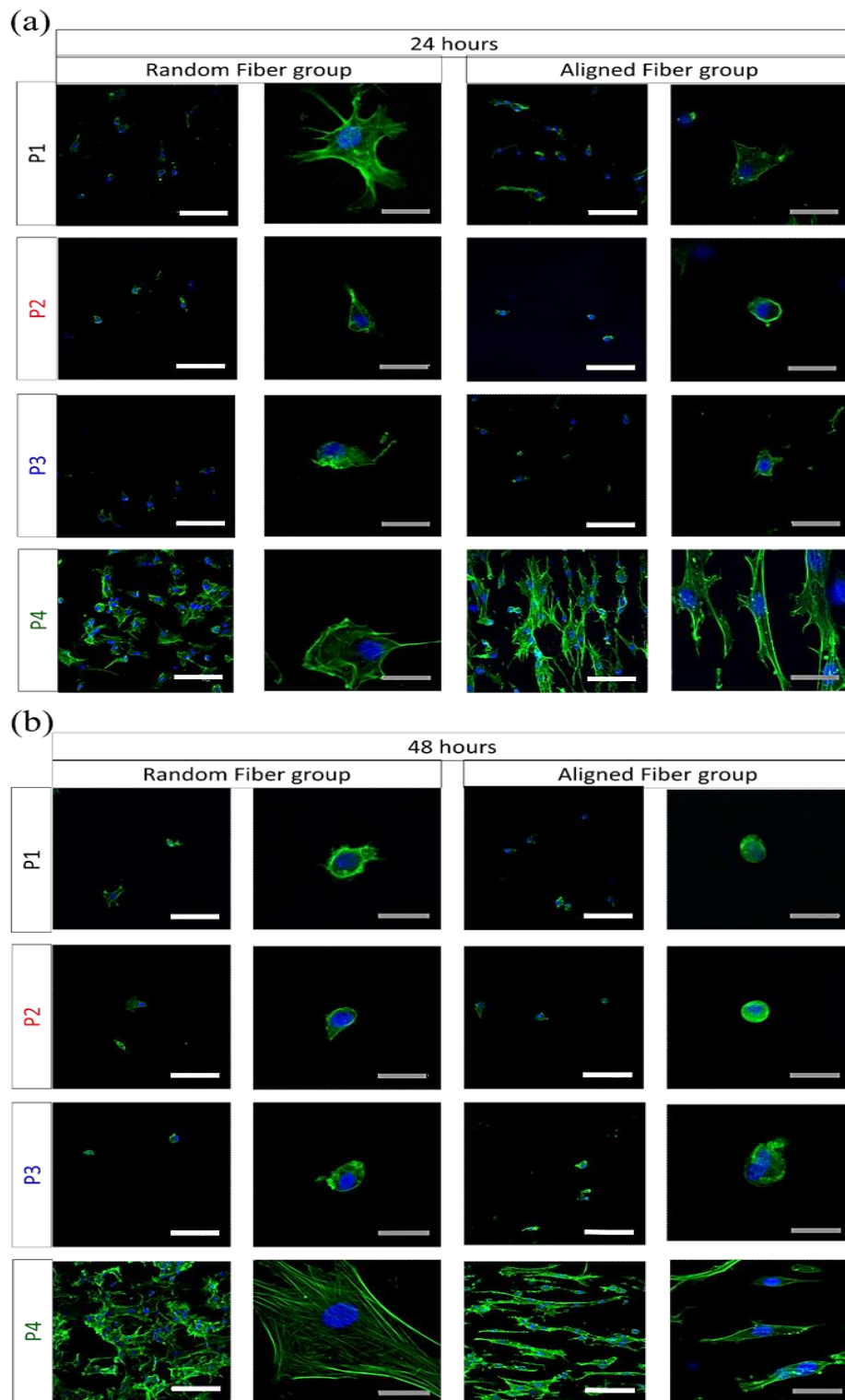


Figure 4.10 Typical images of tendon cells seeded onto both random and aligned polymer membranes (P1 to P4). Green staining represents the cytoskeleton while blue represents the nucleus of cells. Images show cells after (a) 24 hours and (b) 48 hours. Two different magnifications are shown for each condition: the white scale bar represents 100 μm ; the grey scale bar represents 25 μm .

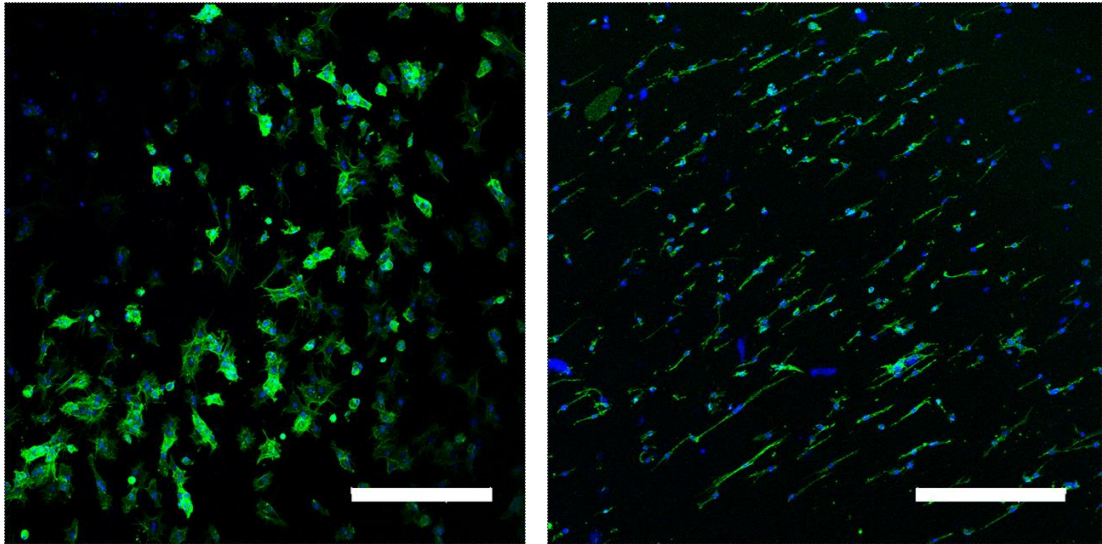


Figure 4.11 Confocal images of tendon cells on (a) random and (b) aligned P4 membranes at 10 magnification. Scale bar represents 400 μm in all pictures.

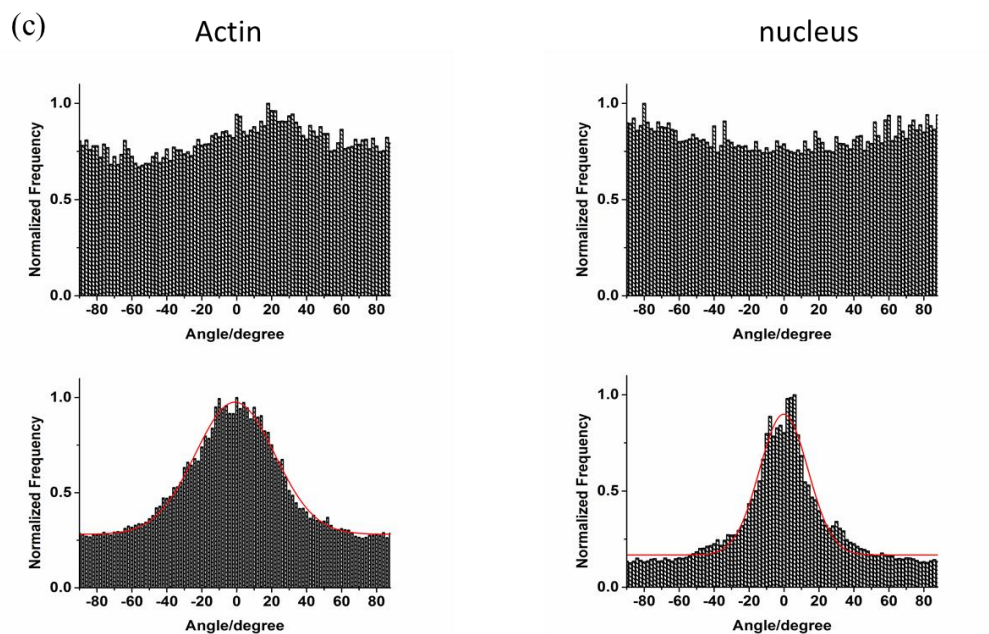


Figure 4.12 Histograms of cell actin and nucleus distribution in both random and aligned fibre systems. A significant difference was witnessed between groups. Aligned fibre systems resulted in clear cell alignment in the fibre direction.

4.4.4 Influence of polymeric membranes over initial cell activity

The influence of chemical composition on cell activity was characterized using an

Alamar blue assay with cell activity calculated relative to that seen in control cells seeded on tissue culture plastic at equivalent time points (control cell activity is shown in Figure 4.13). A trend towards reduced relative cell activity was observed on all the polymer membranes relative to the positive controls for the first 48 hours, after which activity on most membranes tended to increase to either match or surpass that on tissue culture plastic. The activity of cells on PCL was notably lower than in all other materials, and consistently lower than seen in the cell culture plastic controls (Figure 4.14).

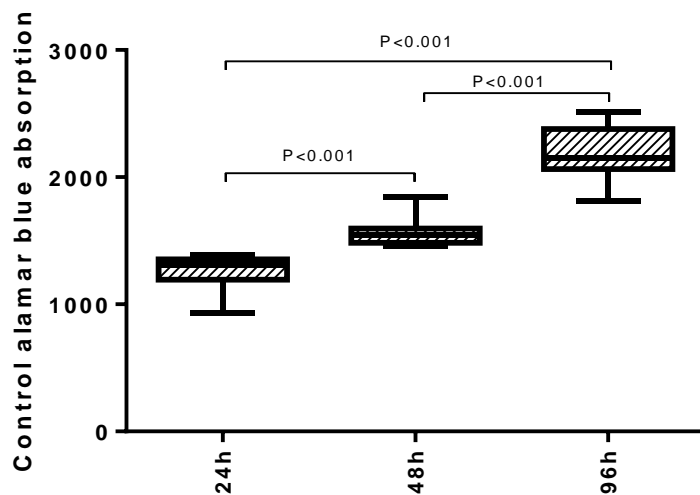


Figure 4.13 Comparison of cell activity in control cells on tissue culture plastic plates. Data compares activity at different time points. The normality of the data was characterized using Shapiro-Wilk normality tests, indicating a non-normal distribution of the data. Results are expressed as box-whisker plots. Statistical significance was calculated using Kruskal-Wallis tests followed by Dunn's tests.

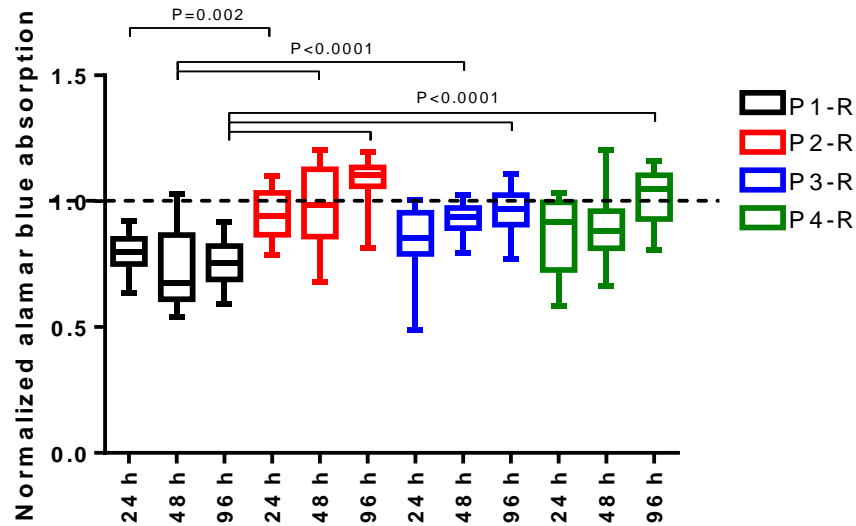


Figure 4.14 Comparison of cell activity between different membranes at different time points. Values represent the mean \pm SD normalized to the activity of control cells at the same time (Set as 1.0) (n = 3). Statistical significance was calculated using the Kruskal-Wallis tests followed by Dunn's tests.

4.5 Conclusion

In this chapter, the interaction between tendon cells and polymer membranes with different chemical compositions and fibre alignments was investigated. Live dead assays showed low membrane toxicity for all materials, indicating possible suitability in biological systems. Meanwhile, tendon cells affinity was shown to be highest on the glycopolymer-based material P4 while the hydrophobic surfaces achieved low cell attachment on the surfaces.

To further characterize tendon cell affinity and morphology on different membranes, a cytoskeleton assay was used to image tendon cell attachment in detail. Tendon cells were found to better adhere on the glycopolymer-based membrane as greater cytoskeleton tension was observed relative to the rounder cells on other membranes. Moreover, it was also observed that through sugar-promoted cell interaction, tendon

cell attachment could be adjusted by orientating the fibre alignment, which would potentially facilitate better healing results for tendon and other related tissue regeneration applications.

Tendon cell activity was also compared for cells in the existence of membranes with different chemical compositions. Data showed that the membranes have some influence on tendon cell activity but no extreme effects of different chemical compositions (within 25 % compared with positive control).

In conclusion, both P2 and P4 possess low cell toxicity and well-controlled cell affinity, which indicate the potential applications of these materials in tendon repair.

Chapter 5 General discussion, conclusion and future work

5.1 General discussion

Tendons connect and transfer strain from muscle to bone, thus allowing muscles to withstand higher stress. Overload of tendon tissue, the increase of age and acute harm will all lead to the injuries of tendon and although have gained tremendous attention over years, it still remains one of the most time and money consuming diseases¹. One of the most several complications of tendon injuries is tendon adhesion, which restricts the movement range as well as the maximum strength of healed tendon¹⁴⁷. Surgical techniques, chemical agents, and physical barriers¹⁵⁴ have all been applied for the prevention of tendon adhesion. Among them, physical barriers showed the wide applicability due to the easy handling, longer retention time, outstanding mechanical properties and biocompatibility⁶ *in vivo*. In further note, chemical agents have been combined with physical barrier taking advantage of the materials science to promote the performance of designed systems¹⁸⁴. Both natural compounds and synthetic polymers have been implemented into the fabrication of anti-adhesive membranes²⁵⁶. Owing to its simple, straightforward process and the formation of well-organized 3D porous structures⁹², electrospinning is one of the most widely used approaches to fabricate anti-adhesive membranes⁶. However, although the adhesion has been effectively prevented, the mechanical properties of healed tendons were sacrificed due to the decreased number of cells followed by the lower amount of fibres deposited during tendon healing²⁵⁷.

This study aimed at designing more defined 3D membranes for tendon adhesion prevention and healing promotion, which including the synthesis of star shape

polymers, fabrication of controlled 3D membrane utilizing electrospinning and evaluation of materials' performance *in vitro* employing bovine tendon cells.

5.1.1 Synthesis of star shaped polymers

Both natural and synthetic polymers have been applied to facilitate tendon adhesion prevention. Synthetic polymers are a common focus for tissue regeneration applications, as the materials offer better mechanical stability and thus excellent control of mechanobiology within the systems. One essential requirement for the selection of polymers is the biocompatibility of the derived materials. Not only benefit from its excellent biocompatibility, but also been shown to possess stronger mechanical behavior and better stability than other polyesters¹⁷⁵, PCL was utilized to constitute the base of the materials.

Meanwhile, it was reported that hydrophobic surfaces will change the conformation of adsorbed proteins²⁵⁸ and thus lower cell attachment²⁴⁴⁻²⁴⁵, which affords the possibility of adhesion prevention here. However, the insufficient healing of tendon still remains to be addressed. As one of the most naturally abundant compound, incorporation of sugar moieties promoted cell attachment to materials, maintaining good viability, thus showing potential for utilizing these materials in tissue engineering. Glycopolymers are promising candidates to address these limitations owing to the existence of bioactive sugar moieties on the polymer backbone^{213, 246-247}. This gives an opportunity to combine the versatility of polymer chemistry with improved cell interaction for biological applications²⁴⁸⁻²⁴⁹. Studies have demonstrated that glycopolymers offer significantly lower toxicity for mammalian cells than standard polymer-based nanoparticles²⁵⁰⁻²⁵¹. However, to date, there has been very little work

focused on fabricating synthetic glycopolymer-based materials, with the main focus on the isolation of cells through sugar-protein interactions²¹⁴⁻²¹⁵ or enzyme immobilization for the delivery purpose²¹⁶. Aiming at improving tendon healing without adhesion, miktoarm hydrophobic copolymers and glycopolymers were chosen to fabricate 3D membranes with distinct cell affinity.

Development of ring-opening polymerization (ROP) allows the synthesis of well-controlled biodegradable polymers with relatively high yield and the possibility for the combination with other functional monomers. In order to retain high livingness of the polymer chains and avoid side reactions, ROP was optimized here to obtain well-controlled PCL with the less time. Although the \bar{D} of the final PCL was not extreme low (~ 1.2), it is much lower compared with the commercial product (1.5-1.6) and showed almost full initiation ability during the following radical polymerization step. Aiming at increasing the hydrophobicity of PCL, styrene was incorporated here as a hydrophobic monomer utilizing atom transfer radical polymerization (ATRP). Coupling reactions were one of the most common side reactions during atom transfer radical polymerization³⁷. Thus here, reaction time was optimized for the purpose of minimizing the side reaction and offer polymers with a well-defined structure. Meanwhile, to introduce functional sugar moieties into PCL, PFS was incorporated here to provide functionality for sugar incorporation. Later on, para-fluorine click reaction was employed here and quantitatively converted the para-fluorine on PFS into glucose units. All the polymers were fully analyzed utilizing GPC and NMR to characterize the molecular weight and the chemical composition of the polymers. GPC results showed a clear shift after each step and NMR confirmed the incorporation of the monomers into the final miktoarm block copolymers, indicating the success in the

synthesis of miktoarm block copolymers by combination of different polymerization techniques.

In summary, by a combination of ROP, ATRP and para-fluorine click reaction, we successfully designed and synthesized both miktoarm hydrophobic polymers (PCL-*mikto*-PS) and miktoarm glycopolymers (PCL-*mikto*-PTFSGlc) with controlled chain length and relatively low polydispersity. This biomaterial provides both anti-adhesive hydrophobic behavior on one side and tendon healing promoter owing to bioactive sugar-containing polymers on the other side.

5.1.2 Materials design and optimization

Electrospinning was selected here to afford porous 3D scaffolds and achieve further control over fibre alignment. Although electrospinning membranes with controlled fibre alignment have been widely used in wound healing and wound dressing²⁵⁹⁻²⁶⁰, it has not been investigated in the promotion of tendon healing. To afford uniform fibres with smooth morphology, firstly, the electrospinning process was optimized in the aspect of solvent ratio and polymer concentration. Then the system was applied to electrospun miktoarm block copolymers to afford membranes with distinct surface properties and chemical compositions. In general, electrospinning of copolymers produced uniform fibres, with some variation in fibre dimensions evident for the different material chemistries investigated, likely a result of the solubility of each polymer type in the co-solvent. To clarify the effects of chemical composition on the surface properties of electrospun fibres, the water contact angles of each membrane were measured. Overall, data demonstrated that mixing block copolymers with homo PCL does change the hydrophilicity of the surface significantly without influencing

the fibre diameter significantly. The incorporation of a hydrophobic block creates a surface, which behaves more hydrophobic and vice versa. Then experiments on the creating aligned or randomly oriented fibres were simply achieved with classical electrospinning approaches by altering fibre collectors. Slightly thinner fibres were attained in aligned membranes compare with the random ones, as a result of the dragging force of the collector, whilst it was also noted that aligning fibres in the hydrophobic block copolymers (P2-P3) led to a further increase in hydrophobicity, which is likely a result of the better organization and reduced spacing between fibres in aligned materials.

Success applications of materials into tissue engineering also require the easy handling and mechanical stability of the materials. It was reported before that the mechanical properties can be optimized by orientating fibres in the same direction¹⁰⁶. To further ascertain the influence of chemical composition and co-mixture polymer systems, the mechanical properties of the materials were investigated, and as typically seen in aligned fibre systems, significant increase in failure stress and modulus and a reduction in failure strain were seen when materials were loaded in the fibre direction, as the large majority of fibres are directly loaded and recruited to resist the applied strain, with less capacity for fibre reorganization under loading²⁶¹. Further, whilst a large energy loss was seen in the first loading cycle for the material, behavior was consistent with further loading, indicating promising mechanical stability. Such ‘plastic-rubber’ behavior is common in PCL derived materials and other polymers and is commonly referred to as the Mullin’s effect¹⁹⁶. During the first loading cycle, weaker bonds between fibres bundles will start to rupture and thus led to the softening of the materials, after which stable mechanical behavior will be witnessed with further cycles to the same strain. However, instantaneous softening will appear again if the load is

increased beyond its previous all-time maximum value at which point further of the weak bonds can be broken. Interestingly, after 30 minutes of rest, a small amount of recovery was seen in the loading curves, which may result from the movement of polymer chains above their glass transition temperature, leading to the rebuild of bonds between fibres. Further investigation of these relationships is warranted to fully understand material behavior. The mechanical properties of these materials showed fully recoverability after enough time at room temperature, which further proved the energy loss observed before was caused by the break of reversible weaker physical bonds between the fibre bundles rather than the break of chemical covalent bonds.

Relating these mechanical parameters to those of other scaffold materials, or typical aligned fibrous tissues, shows promising strength, stability and flexibility of the membranes²⁶². Taking as an example, in its stable state, the glycopolymer membranes achieve a maximum modulus of around 700 MPa and failure strain of 40 %. This offers vastly improved stiffness and stability relative to typical natural materials such as collagen gels¹⁸⁷ but not at the expense of poor flexibility as seen with cellulose¹⁸⁸⁻¹⁸⁹ or chitosan¹⁹⁰ based materials. Indeed, the mechanical parameters are reasonably well matched to those of tendon or ligament, which are generally in the range of 500-1000 MPa modulus and 10-25% failure strain²⁶³⁻²⁶⁵.

In summary, 3D membranes of the modified PCL materials, with controlled mechanical properties of appropriate magnitude to suit a range of biomedical applications, were successfully electrospun to make membranes with a tissue mimetic structure, which could potentially be used in tissue engineering. Fibre orientation has been controlled, offering capacity to recapitulate the anisotropy of many fibrous tissues. The morphology and properties of the membranes were characterized by SEM and an assessment of water contact angle, showing that hydrophilicity of a membrane

could be dramatically improved with the addition of sugar groups, without altering the fibre diameters.

Such materials offer real promise as a tissue regeneration platform²⁶⁶⁻²⁶⁸, bringing excellent mechanical properties for functional loading in a highly controllable and tunable material, in which cell-material interactions can also be manipulated to meet the needs of different fibrous tissues, through manipulating material chemistry.

5.1.3 *In vitro* preliminary cell biocompatible, cell attachment and cell activity tests

Various synthetic platforms, such as PCL-*c*-PLA²⁵⁶ and PEG-based platforms²⁶⁹, have been researched to lower cell attachment and prevent tendon adhesion. However, here we propose a novel hydrophobic platform for anti-adhesive purpose and a glycopolymer incorporated platform for promoting cell interaction. As the main cell type controls tendon performance by adjusting collagen synthesis and protein secretion²⁷⁰, tendon cells were chosen here as a model cell line to first characterize the toxicity, affinity and influence over cell activity of the designed membranes during the first 48 hours. Tendon cells were seeded directly onto the electrospun membrane and incubate up to 48 hours to characterize initial tendon cells response. Calcein AM and ethidium homodimer were utilized here to investigate both initial cell viability and cell coverage on the materials. Results were obtained by calculating the number of green live cells and red dead cells or area of green live cells, respectively. Preliminary tendon cells affinity to each membrane type was assessed by characterizing cell morphology on the materials, using phalloidin and DAPI to stain the cytoskeleton green and nucleus blue, respectively. The preliminary influence of different membranes on cell activity was characterized using an Alamar blue assay with cell activity normalized to

that seen in control cells seeded on tissue culture plastic at equivalent time points.

In vitro membrane biocompatibility tests with tendon cells showed that all membranes could maintain cell viability above 60 % after 48 h incubation. Additionally, tendon cells attachment capabilities of membranes were lowered by increase the hydrophobicity of the membrane and significantly improved by incorporating sugar molecules into PCL, witnessed by cell coverage on each membrane type during the 48 hours. Cell affinity tests demonstrated that tendon cells on the glycopolymer membranes were better adhered, as greater cytoskeleton tension was observed relative to the rounder cells on the hydrophobic membranes. Both of the results potentially indicate the increase of hydrophobicity decrease protein adherence and lower cell attachment while incorporation of sugar moieties provide functional groups to PCL and promote the interaction with cells. Meanwhile, a trend towards reduced relative cell activity was observed on all the polymer membranes relative to the positive controls for the first 48 hours, after which activity on most membranes tended to increase to either match or surpass that on tissue culture plastic at 96 hours. The activity on PCL was notably lower than in all other materials, and consistently lower than seen in the cell culture plastic controls. It has been shown that the incorporation of proteins or growth factors can increase cell activity on the surface²⁷¹. P4 membranes contain sugar moieties, which interact promptly with lectins and then interact actively with cells, thus leads to an increase in cell activity. In the meantime, cells tend to behave more active when cannot attach to a surface and try to proliferate off, thus there are also improved cell activity trend in the hydrophobic groups.

One additional key function of applying aligned fibre systems in tissue engineering is to guide cell attachment²⁷² and effect cell signaling²⁷³. In tissues with aligned fibres, such as tendon, ligament and intervertebral disc, cells are generally highly elongated

and arranged in rows between fibres, connected via gap junctions along and between rows²⁷⁴⁻²⁷⁵.

The ability of our glycopolymer-based material to control initial tendon cell organization was subsequently investigated, to determine if *in vivo* cell organization could be recapitulated. Excitingly, both cytoskeletal stress fibres and cell nuclei of tendon cells were elongated and aligned in parallel on the aligned glycopolymer membranes during the first 48 hours, recapitulating a number of the key features of cell organization within tissues such as tendon.

Whilst this capacity to control cell organization has previously been demonstrated with peptide functionalized aligned fibre polymers²⁷⁶, this is the first time that a synthetic glycopolymer has been shown to exhibit the same effect on cell attachment. Previous studies have demonstrated that synthetic glycopolymers can interact specifically with human lectins²⁷⁷ and the sequence of sugar moieties diversifies the specific interaction²⁷⁸, potentially explain this promising cell-material interaction.

5.1.4 Limitations

Although this research provided a novel platform for tendon healing, there are still some limitations that worthy noted when interpreting the results.

Firstly, only one specific polymer chain length was designed and synthesized for each chemical composition. It was known that the block polymer chain length has a notable impact on the performance of copolymers in biological systems²⁷⁹⁻²⁸⁰. In order to fully understand the influence of chemical composition, polymers with various chain lengths should be synthesized and characterized.

Additionally, when translating polymers into the 3D scaffold, synthesized block

copolymers were blend with a high molecular weight homo PCL and then electrospun into fibres. Researches showed the ratio of constituent have an influence on the final materials properties^{269, 281}, however, only 1:4 block copolymers to PCL membrane was evaluated in this case. Ideally, membranes with the different block copolymer, PCL ratio should be fabricated for the purpose of optimizing the ratio of block copolymers ratio to achieve optimal results.

Meanwhile, during the mechanical characterization of the membranes, it is evident that 100 N load cell was a magnitude higher than the failure force of random fibre membranes and aligned systems when loading against fibres. Ideally, matched load cells should be applied in each set of experiments. Nevertheless, considering the effect of load cell type over the significant difference between groups is minimal, 100 N load cell was applied for all our mechanical tests.

Lastly, although cell attachment was effectively controlled by implementing changing the chemical composition of the membrane, however, the underlying mechanisms through which cells interact with the materials, and the influence of polymer type on cell metabolism and expression need to be addressed using further analysis.

5.2 Conclusion

Treatment aiming at tendon healing mostly focused on prevention of tendon adhesion and resulted in the sacrifice of healed tendon mechanics²⁸². Starting from here, we proposed a system employing a hydrophobic surface to achieve the anti-adhesive properties and a sugar-containing layer for the purpose of promoting cell attachment and encouraging tendon healing.

In chapter 2, in order to ensure the biocompatibility of the membrane, PCL was

selected as the main part of the miktoarm block copolymers. Functional PCL was synthesized by a combination of ring opening polymerization, atom transfer radical polymerization and post-modification with styrene, PFS and sugar moieties, respectively. Well defined miktoarm copolymers were obtained after optimization of the reaction condition with targeted chain length for further production of materials with distinct properties.

In chapter 3, polymers synthesized before was translated into 3D membrane utilizing electrospinning. Firstly, electrospun conditions were optimized to produce uniform fibres bundles with smooth morphology using homo PCL as the model polymer. Then the conditions were applied to the electrospun of other miktoarm copolymers. Results showed all the systems possessed well-controlled porous surface while having distinct hydrophilicity. Later on, alignment of fibres was achieved by adjusting the collector type and uni-directional fibres were obtained. This not only provides membranes with a stronger mechanical strength, which could help the real application of these materials, but also recapitulates, the anisotropy of tendon tissues. Mechanical characterization of these materials showed the strong, stable and recoverable of the obtained platforms.

In chapter 4, to confirm the suitability of these systems for tendon healing purpose, tendon cells were chosen here as a model cell source for the evaluation of materials' toxicity, cell affinity and effect on cell activity. The *in vitro* cell culture showed the biocompatibility of these membranes for tendon healing. It was observed by changing the chemical composition of the materials, tendon cell affinity towards materials can be easily and efficiently adjusted. Additionally, fibre alignment also provides extra biological cues for cell guidance, which benefits the applications of these materials in tendon healing.

In summary, these membranes provide a potential candidate for adhesion-free tendon

healing with optimal healing mechanics. Furthermore, the obtained platforms should also possess the possibility for related biomedical applications.

5.3 Future work

Whilst this study has offered a novel platform for tendon healing, it does need further experiments to elucidate the mechanism behind in order to achieve better results.

- Combination of electrospun layers and characterize the mechanics and cell responses.

Preliminary trials on fabrication of bilayer membranes were carried out by sequentially depositing homo PCL fibres on to the same matrix in layers, following a procedure reported before⁸⁸. The collector orientation between layers was adjusted to obtained fibres with a distinct stack orientation. The cross-section image of the resulting membrane showed clear delineation of the layers (Figure 5.1), with distinct differences in fibre stack orientation, achieved by adjusting the collector orientation before electrospun the second layer. The merge of the membrane boundary witnessed between layers and difference in fibre orientation observed within layers proved the success in the fabrication of the bi-layer system. These data validate the possibility to construct bi-layer membranes via electrospinning.

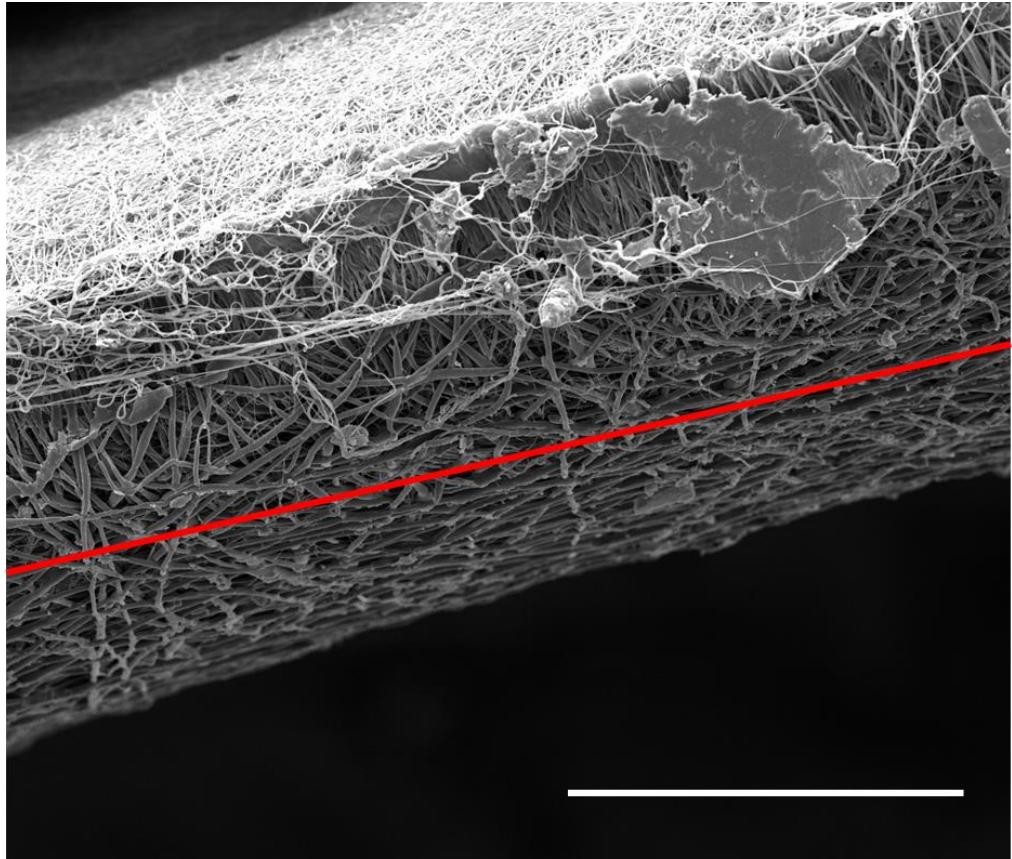


Figure 5.1 SEM image of a cross-section of a bi-layer electrospun membrane. Redline indicates the boundary between the two layers. Two different fibre orientations are shown in the image. Scale bar represents 200 μm .

- Need further molecular biological assay to illuminate the relationship between material apparent properties and the mechanism behind. For instance, the mechanism of higher cell attachment and coverage on glycopolymers-based membranes towards tendon need to be addressed.
- *In vitro* degradation assay need to be addressed to characterize both structural and mechanical stability of the membranes under cell environment. Afterwards, collagen production need to be performed to evaluate the influence of both chemical composition and micro mechanics generated by fibres on the collagen amount and maturation.

References

1. Abbah, S. A.; Spanouides, K.; O'Brien, T.; Pandit, A.; Zeugolis, D. I., Assessment of stem cell carriers for tendon tissue engineering in pre-clinical models. *Stem Cell Res. Ther.* **2014**, *5* (2), 38-47.
2. James, R.; Kesturu, G.; Balian, G.; Chhabra, A. B., Tendon: Biology, biomechanics, repair, growth factors, and evolving treatment options. *J. Hand. Surg-AM.* **2008**, *33A* (1), 102-112.
3. Jaibaji, M., Advances in the biology of zone II flexor tendon healing and adhesion formation. *Ann Plas Surg* **2000**, *45* (1), 83-92.
4. Pryce, B. A.; Watson, S. S.; Murchison, N. D.; Staverosky, J. A.; Dünker, N.; Schweitzer, R., Recruitment and maintenance of tendon progenitors by TGF β signaling are essential for tendon formation. *Development.* **2009**, *136* (8), 1351-1361.
5. Chow, J.; Dovel, S.; Thomes, L.; Ho, P.; Saldana, J., A comparison of results of extensor tendon repair followed by early controlled mobilisation versus static immobilisation. *J. Hand Surg. Am.* **1989**, *14* (1), 18-20.
6. Li, J.; Feng, X.; Liu, B.; Yu, Y.; Sun, L.; Liu, T.; Wang, Y.; Ding, J.; Chen, X., Polymer materials for prevention of postoperative adhesion. *Acta Biomater.* **2017**, 21-40.
7. Menderes, A.; Mola, F.; Tayfur, V.; Vayvada, H.; Barutçu, A., Prevention of peritendinous adhesions following flexor tendon injury with seprafilm. *Ann Plas Surg* **2004**, *53* (6), 560-564.
8. Buschmann, J.; Calcagni, M.; Bürgisser, G. M.; Bonavoglia, E.; Neuenschwander, P.; Milleret, V.; Giovanoli, P., Synthesis, characterization and histomorphometric analysis of cellular response to a new elastic DegraPol® polymer

for rabbit Achilles tendon rupture repair. *J. Tissue. Eng. Regen. Med.* **2012**, *9*, 584-594.

9. Jenkins, A.; Kratochvil, P.; Stepto, R.; Suter, U., Glossary of basic terms in polymer science (IUPAC Recommendations 1996). *Pure Appl. Chem.* **1996**, *68* (12), 2287-2311.

10. Lutz, J.-F.; Lehn, J.-M.; Meijer, E.; Matyjaszewski, K., From precision polymers to complex materials and systems. *Nat. Rev. Mater.* **2016**, *1* (5), 16024.

11. SZWARC, M., 'Living' polymers. *Nature* **1956**, *178* (4543), 1168.

12. Leuchs, H., Ueber die Glycin-carbonsäure. *Eur. J. Inorg. Chem* **1906**, *39* (1), 857-861.

13. Miyamoto, M.; Sawamoto, M.; Higashimura, T., Living polymerization of isobutyl vinyl ether with hydrogen iodide/iodine initiating system. *Macromolecules* **1984**, *17* (3), 265-268.

14. Kato, M.; Kamigaito, M.; Sawamoto, M.; Higashimura, T., Polymerization of methyl methacrylate with the carbon tetrachloride/dichlorotris-(triphenylphosphine) ruthenium (II)/methylaluminum bis (2, 6-di-tert-butylphenoxide) initiating system: possibility of living radical polymerization. *Macromolecules* **1995**, *28* (5), 1721-1723.

15. Wang, J.-S.; Matyjaszewski, K., Controlled/" living" radical polymerization. Atom transfer radical polymerization in the presence of transition-metal complexes. *J. Am. Chem. Soc.* **1995**, *117* (20), 5614-5615.

16. Solomon, D. H.; Rizzardo, E.; Cacioli, P., Polymerization process and polymers produced thereby. Google Patents: 1986.

17. Chiefari, J.; Chong, Y.; Ercole, F.; Krstina, J.; Jeffery, J.; Le, T. P.; Mayadunne, R. T.; Meijs, G. F.; Moad, C. L.; Moad, G., Living free-radical polymerization by reversible addition– fragmentation chain transfer: the RAFT process. *Macromolecules* **1998**, *31* (16), 5559-5562.

18. Percec, V.; Guliashvili, T.; Ladislaw, J. S.; Wistrand, A.; Stjerndahl, A.; Sienkowska, M. J.; Monteiro, M. J.; Sahoo, S., Ultrafast synthesis of ultrahigh molar mass polymers by metal-catalyzed living radical polymerization of acrylates, methacrylates, and vinyl chloride mediated by SET at 25 C. *J. Am. Chem. Soc.* **2006**, *128* (43), 14156-14165.
19. Satoh, K.; Nakashima, J.; Kamigaito, M.; Sawamoto, M., Novel BF₃OEt₂/R-OH initiating system for controlled cationic polymerization of styrene in the presence of water. *Macromolecules* **2001**, *34* (3), 396-401.
20. Okamoto, Y. In *Cationic ring-opening polymerization of lactones in the presence of alcohol*, Macromol. Symp., Wiley Online Library: 1991; pp 117-133.
21. Nomura, R.; Ueno, A.; Endo, T., Anionic ring-opening polymerization of macrocyclic esters. *Macromolecules* **1994**, *27* (2), 620-621.
22. Albertsson, A.-C.; Varma, I. K., Recent developments in ring opening polymerization of lactones for biomedical applications. *Biomacromolecules* **2003**, *4* (6), 1466-1486.
23. Dechy-Cabaret, O.; Martin-Vaca, B.; Bourissou, D., Controlled ring-opening polymerization of lactide and glycolide. *Chem. Rev.* **2004**, *104* (12), 6147-6176.
24. Xu, F.; Wang, Z.; Yang, W., Surface functionalization of polycaprolactone films via surface-initiated atom transfer radical polymerization for covalently coupling cell-adhesive biomolecules. *Biomaterials* **2010**, *31* (12), 3139-3147.
25. Jiang, H.; Wang, X.; Li, C.; Li, J.; Xu, F.; Mao, C.; Yang, W.; Shen, J., Improvement of hemocompatibility of polycaprolactone film surfaces with zwitterionic polymer brushes. *Langmuir* **2011**, *27* (18), 11575-11581.
26. Gilliom, L. R.; Grubbs, R. H., Titanacyclobutanes derived from strained, cyclic olefins: the living polymerization of norbornene. *J. Am. Chem. Soc.* **1986**, *108* (4),

733-742.

27. Bielawski, C. W.; Grubbs, R. H., Living ring-opening metathesis polymerization. *Prog. Polym. Sci* **2007**, *32* (1), 1-29.
28. Braunecker, W. A.; Matyjaszewski, K., Controlled/living radical polymerization: Features, developments, and perspectives. *Prog. Polym. Sci* **2007**, *32* (1), 93-146.
29. Nicolas, J.; Guillaneuf, Y.; Lefay, C.; Bertin, D.; Gigmes, D.; Charleux, B., Nitroxide-mediated polymerization. *Prog. Polym. Sci* **2013**, *38* (1), 63-235.
30. Hawker, C. J.; Barclay, G. G.; Orellana, A.; Dao, J.; Devonport, W., Initiating systems for nitroxide-mediated "living" free radical polymerizations: synthesis and evaluation. *Macromolecules* **1996**, *29* (16), 5245-5254.
31. Georges, M. K.; Veregin, R. P.; Kazmaier, P. M.; Hamer, G. K., Narrow molecular weight resins by a free-radical polymerization process. *Macromolecules* **1993**, *26* (11), 2987-2988.
32. Gillet, J.-P.; Guerret, O.; Tordo, P., Method for preparing β -phosphorous nitroxide radicals. Google Patents: 2003.
33. Keana, J. F., Newer aspects of the synthesis and chemistry of nitroxide spin labels. *Chem. Rev.* **1978**, *78* (1), 37-64.
34. Forrester, A.; Thomson, R., Stable nitroxide radicals. *Nature* **1964**, *203* (4940), 74-75.
35. Benoit, D.; Chaplinski, V.; Braslau, R.; Hawker, C. J., Development of a universal alkoxyamine for "living" free radical polymerizations. *J. Am. Chem. Soc.* **1999**, *121* (16), 3904-3920.
36. Matyjaszewski, K., Atom transfer radical polymerization (ATRP): current status and future perspectives. *Macromolecules* **2012**, *45* (10), 4015-4039.

37. Matyjaszewski, K.; Xia, J., Atom transfer radical polymerization. *Chem. Rev.* **2001**, *101* (9), 2921-2990.
38. Atzet, S.; Curtin, S.; Trinh, P.; Bryant, S.; Ratner, B., Degradable poly (2-hydroxyethyl methacrylate)-co-polycaprolactone hydrogels for tissue engineering scaffolds. *Biomacromolecules* **2008**, *9* (12), 3370-3377.
39. Tang, W.; Matyjaszewski, K., Effects of initiator structure on activation rate constants in ATRP. *Macromolecules* **2007**, *40* (6), 1858-1863.
40. Tang, W.; Matyjaszewski, K., Effect of ligand structure on activation rate constants in ATRP. *Macromolecules* **2006**, *39* (15), 4953-4959.
41. Braunecker, W. A.; Tsarevsky, N. V.; Gennaro, A.; Matyjaszewski, K., Thermodynamic components of the atom transfer radical polymerization equilibrium: quantifying solvent effects. *Macromolecules* **2009**, *42* (17), 6348-6360.
42. Perrier, S. b., 50th Anniversary Perspective: RAFT Polymerization A User Guide. *Macromolecules* **2017**, *50* (19), 7433-7447.
43. Chong, Y.; Le, T. P.; Moad, G.; Rizzardo, E.; Thang, S. H., A more versatile route to block copolymers and other polymers of complex architecture by living radical polymerization: the RAFT process. *Macromolecules* **1999**, *32* (6), 2071-2074.
44. Convertine, A. J.; Lokitz, B. S.; Vasileva, Y.; Myrick, L. J.; Scales, C. W.; Lowe, A. B.; McCormick, C. L., Direct synthesis of thermally responsive DMA/NIPAM diblock and DMA/NIPAM/DMA triblock copolymers via aqueous, room temperature RAFT polymerization. *Macromolecules* **2006**, *39* (5), 1724-1730.
45. Stenzel, M. H.; Cummins, L.; Roberts, G. E.; Davis, T. P.; Vana, P.; Barner-Kowollik, C., Xanthate mediated living polymerization of vinyl acetate: a systematic variation in MADIX/RAFT agent structure. *Macromol. Chem. Phys.* **2003**, *204* (9), 1160-1168.

46. Zheng, G.; Pan, C., Preparation of star polymers based on polystyrene or poly(styrene-*b*N-isopropyl acrylamide) and divinylbenzene via reversible addition-fragmentation chain transfer polymerization. *Polymer* **2005**, *46* (8), 2802-2810.
47. Zhang, C.; Zhou, Y.; Liu, Q.; Li, S.; Perrier, S. b.; Zhao, Y., Facile synthesis of hyperbranched and star-shaped polymers by RAFT polymerization based on a polymerizable trithiocarbonate. *Macromolecules* **2011**, *44* (7), 2034-2049.
48. Gody, G.; Maschmeyer, T.; Zetterlund, P. B.; Perrier, S., Rapid and quantitative one-pot synthesis of sequence-controlled polymers by radical polymerization. *Nat. Commun.* **2013**, *4*, 2505-2514.
49. Luo, K.; Yang, J.; Kopečková, P.; Kopeček, J. i., Biodegradable multiblock poly [N-(2-hydroxypropyl) methacrylamide] via reversible addition– fragmentation chain transfer polymerization and click chemistry. *Macromolecules* **2011**, *44* (8), 2481-2488.
50. Zhang, Q.; Wilson, P.; Li, Z.; McHale, R.; Godfrey, J.; Anastasaki, A.; Waldron, C.; Haddleton, D. M., Aqueous copper-mediated living polymerization: exploiting rapid disproportionation of CuBr with Me6TREN. *J. Am. Chem. Soc.* **2013**, *135* (19), 7355-7363.
51. Leng, X.; Nguyen, N. H.; van Beusekom, B.; Wilson, D. A.; Percec, V., SET-LRP of 2-hydroxyethyl acrylate in protic and dipolar aprotic solvents. *Polym. Chem.* **2013**, *4* (10), 2995-3004.
52. Aksakal, R.; Resmini, M.; Becer, C., SET-LRP of acrylates catalyzed by a 1 penny copper coin. *Polym. Chem.* **2016**, 6564-6569.
53. Gauthier, M. A.; Gibson, M. I.; Klok, H. A., Synthesis of Functional Polymers by Post-Polymerization Modification. *Angew. Chem. Int. Ed.* **2009**, *48* (1), 48-58.
54. Becer, C. R.; Hoogenboom, R.; Schubert, U. S., Click chemistry beyond metal-

- catalyzed cycloaddition. *Angew. Chem. Int. Ed.* **2009**, *48* (27), 4900-4908.
55. Posner, T., Beiträge zur Kenntniss der ungesättigten Verbindungen. II. Ueber die Addition von Mercaptanen an ungesättigte Kohlenwasserstoffe. *Ber. Dtsch. Chem. Ges.* **1905**, *38* (1), 646-657.
56. Correspondence. *J. Soc. Chem. Ind.* **1938**, *57* (32), 752-754.
57. Yilmaz, G.; Uzunova, V.; Hartweg, M.; Beyer, V.; Napier, R.; Becer, C. R., The effect of linker length on ConA and DC-SIGN binding of S-glucosyl functionalized poly (2-oxazoline) s. *Polym. Chem.* **2018**, *9* (5), 611-618.
58. Lin, C.-C.; Raza, A.; Shih, H., PEG hydrogels formed by thiol-ene photo-click chemistry and their effect on the formation and recovery of insulin-secreting cell spheroids. *Biomaterials* **2011**, *32* (36), 9685-9695.
59. Kharkar, P. M.; Rehmann, M. S.; Skeens, K. M.; Maverakis, E.; Kloxin, A. M., Thiol-ene click hydrogels for therapeutic delivery. *ACS Biomater. Sci. Eng.* **2016**, *2* (2), 165-179.
60. Pummer, W. J.; Wall, L. A., Reactions of hexafluorobenzene. *Science* **1958**, *127* (3299), 643-644.
61. Godsell, J.; Stacey, M.; Tatlow, J., Hexafluorobenzene. *Nature* **1956**, *178* (4526), 199.
62. Becer, C. R.; Babiuch, K.; Pilz, D.; Hornig, S.; Heinze, T.; Gottschaldt, M.; Schubert, U. S., Clicking Pentafluorostyrene Copolymers: Synthesis, Nanoprecipitation, and Glycosylation. *Macromolecules* **2009**, *42* (7), 2387-2394.
63. Gan, D.; Mueller, A.; Wooley, K. L., Amphiphilic and hydrophobic surface patterns generated from hyperbranched fluoropolymer/linear polymer networks: minimally adhesive coatings via the crosslinking of hyperbranched fluoropolymers. *J. Polym. Sci. A* **2003**, *41* (22), 3531-3540.

64. Mueller, A.; Kowalewski, T.; Wooley, K. L., Synthesis, characterization, and derivatization of hyperbranched polyfluorinated polymers. *Macromolecules* **1998**, *31* (3), 776-786.
65. Ott, C.; Hoogenboom, R.; Schubert, U. S., Post-modification of poly(pentafluorostyrene): a versatile "click" method to create well-defined multifunctional graft copolymers. *Chem. comm.* **2008**, (30), 3516-3518.
66. Noy, J.-M.; Koldevitz, M.; Roth, P. J., Thiol-reactive functional poly (meth) acrylates: multicomponent monomer synthesis, RAFT (co) polymerization and highly efficient thiol–para-fluoro postpolymerization modification. *Polym. Chem.* **2015**, *6* (3), 436-447.
67. Qian, E. A.; Wixtrom, A. I.; Axtell, J. C.; Saebi, A.; Jung, D.; Rehak, P.; Han, Y.; Moully, E. H.; Mosallaei, D.; Chow, S., Atomically precise organomimetic cluster nanomolecules assembled via perfluoroaryl-thiol S_NAr chemistry. *Nat. Chem.* **2017**, *9* (4), 333-340.
68. Liu, R.; Patel, D.; Screen, H. R.; Becer, C. R., A2B-Miktoarm Glycopolymer Fibres and Their Interactions with Tenocytes. *Bioconjug Chem.* **2017**, *28* (7), 1955-1964.
69. Huisgen, R., Centenary lecture-1, 3-dipolar cycloadditions. 1961.
70. Rostovtsev, V. V.; Green, L. G.; Fokin, V. V.; Sharpless, K. B., A stepwise huisgen cycloaddition process: copper (I)-catalyzed regioselective "ligation" of azides and terminal alkynes. *Angew. Chem.* **2002**, *114* (14), 2708-2711.
71. Tornøe, C. W.; Christensen, C.; Meldal, M., Peptidotriazoles on solid phase:[1, 2, 3]-triazoles by regiospecific copper (I)-catalyzed 1, 3-dipolar cycloadditions of terminal alkynes to azides. *J. Org. Chem.* **2002**, *67* (9), 3057-3064.
72. Agard, N. J.; Prescher, J. A.; Bertozzi, C. R., A strain-promoted [3+ 2] azide–

alkyne cycloaddition for covalent modification of biomolecules in living systems. *J. Am. Chem. Soc.* **2004**, *126* (46), 15046-15047.

73. Lallana, E.; Riguera, R.; Fernandez-Megia, E., Reliable and efficient procedures for the conjugation of biomolecules through Huisgen azide–alkyne cycloadditions. *Angew. Chem. Int. Ed.* **2011**, *50* (38), 8794-8804.

74. Lutz, J. F., 1, 3-Dipolar cycloadditions of azides and alkynes: a universal ligation tool in polymer and materials science. *Angew. Chem. Int. Ed.* **2007**, *46* (7), 1018-1025.

75. Kim, S. O.; Solak, H. H.; Stoykovich, M. P.; Ferrier, N. J.; de Pablo, J. J.; Nealey, P. F., Epitaxial self-assembly of block copolymers on lithographically defined nanopatterned substrates. *Nature* **2003**, *424* (6947), 411-414.

76. Tyrrell, Z. L.; Shen, Y.; Radosz, M., Fabrication of micellar nanoparticles for drug delivery through the self-assembly of block copolymers. *Prog. Polym. Sci* **2010**, *35* (9), 1128-1143.

77. Lutz, J.-F.; Ouchi, M.; Liu, D. R.; Sawamoto, M., Sequence-controlled polymers. *Science* **2013**, *341* (6146), 1238149-1238159.

78. Zhang, Q.; Collins, J.; Anastasaki, A.; Wallis, R.; Mitchell, D. A.; Becer, C. R.; Haddleton, D. M., Sequence-Controlled Multi-Block Glycopolymers to Inhibit DC-SIGN-gp120 Binding. *Angew. Chem. Int. Ed.* **2013**, *52* (16), 4435-4439.

79. Khanna, K.; Varshney, S.; Kakkar, A., Miktoarm star polymers: advances in synthesis, self-assembly, and applications. *Polym. Chem.* **2010**, *1* (8), 1171-1185.

80. Soliman, G. M.; Sharma, A.; Maysinger, D.; Kakkar, A., Dendrimers and miktoarm polymers based multivalent nanocarriers for efficient and targeted drug delivery. *Chem. Comm.* **2011**, *47* (34), 9572-9587.

81. Cai, T.; Yang, W. J.; Neoh, K.-G.; Kang, E.-T., Preparation of jellyfish-shaped

amphiphilic block-graft copolymers consisting of a poly (ϵ -caprolactone)-block-poly (pentafluorostyrene) ring and poly (ethylene glycol) lateral brushes. *Polym. Chem.* **2012**, *3* (4), 1061-1068.

82. Dai, F.; Sun, P.; Liu, Y.; Liu, W., Redox-cleavable star cationic PDMAEMA by arm-first approach of ATRP as a nonviral vector for gene delivery. *Biomaterials* **2010**, *31* (3), 559-569.

83. Sau, T. K.; Murphy, C. J., Self-assembly patterns formed upon solvent evaporation of aqueous cetyltrimethylammonium bromide-coated gold nanoparticles of various shapes. *Langmuir* **2005**, *21* (7), 2923-2929.

84. Xie, J.; Xu, C.; Kohler, N.; Hou, Y.; Sun, S., Controlled PEGylation of monodisperse Fe₃O₄ nanoparticles for reduced non-specific uptake by macrophage cells. *Adv. Mater.* **2007**, *19* (20), 3163-3166.

85. Tian, Y.; Jiang, X.; Chen, X.; Shao, Z.; Yang, W., Doxorubicin-loaded magnetic silk fibroin nanoparticles for targeted therapy of multidrug-resistant cancer. *Adv. Mater.* **2014**, *26* (43), 7393-7398.

86. Guan, B. Y.; Yu, L.; Lou, X. W., Formation of asymmetric bowl-like mesoporous particles via emulsion-induced interface anisotropic assembly. *J. Am. Chem. Soc.* **2016**, *138* (35), 11306-11311.

87. Greiner, A.; Wendorff, J. H., Electrospinning: a fascinating method for the preparation of ultrathin fibres. *Angew. Chem. Int. Ed.* **2007**, *46* (30), 5670-5703.

88. Ma, J.; Wang, H.; He, B.; Chen, J., A preliminary in vitro study on the fabrication and tissue engineering applications of a novel chitosan bilayer material as a scaffold of human neonatal dermal fibroblasts. *Biomaterials* **2001**, *22* (4), 331-336.

89. Lutolf, M.; Hubbell, J., Synthetic biomaterials as instructive extracellular microenvironments for morphogenesis in tissue engineering. *Nat. Biotechnol.* **2005**,

23 (1), 47-55.

90. Gilmore, J.; Burg, T.; Groff, R. E.; Burg, K. J., Design and optimization of a novel bio-loom to weave melt-spun absorbable polymers for bone tissue engineering.

J. Biomed. Mater. Res. B **2017**, *105* (6), 1342-1351.

91. Khalid, B.; Bai, X.; Wei, H.; Huang, Y.; Wu, H.; Cui, Y., Direct blow-spinning of nanofibres on a window screen for highly efficient PM2.5 removal.

Nano Lett. **2017**, *17* (2), 1140-1148.

92. Bhardwaj, N.; Kundu, S. C., Electrospinning: a fascinating fibre fabrication technique.

Biotechnol. Adv. **2010**, *28* (3), 325-347.

93. Anton, F., Process and apparatus for preparing artificial threads. Google Patents: 1934.

94. Naeimirad, M.; Zadhoush, A.; Kotek, R.; Esmaeely Neisiany, R.; Nouri Khorasani, S.; Ramakrishna, S., Recent advances in core/shell bicomponent fibres and nanofibres: A review.

J. Appl. Polym. Sci. **2018**, *135* (21), 46265.

95. Jacobs, V.; Anandjiwala, R. D.; Maaza, M., The influence of electrospinning parameters on the structural morphology and diameter of electrospun nanofibres.

J. Appl. Polym. Sci. **2010**, *115* (5), 3130-3136.

96. Deitzel, J. M.; Kleinmeyer, J.; Harris, D.; Tan, N. B., The effect of processing variables on the morphology of electrospun nanofibres and textiles.

Polymer **2001**, *42* (1), 261-272.

97. Subbiah, T.; Bhat, G.; Tock, R.; Parameswaran, S.; Ramkumar, S., Electrospinning of nanofibres.

J. Appl. Polym. Sci. **2005**, *96* (2), 557-569.

98. Luo, C.; Nangrejo, M.; Edirisinghe, M., A novel method of selecting solvents for polymer electrospinning.

Polymer **2010**, *51* (7), 1654-1662.

99. Zong, X.; Kim, K.; Fang, D.; Ran, S.; Hsiao, B. S.; Chu, B., Structure and

process relationship of electrospun bioabsorbable nanofibre membranes. *Polymer* **2002**, *43* (16), 4403-4412.

100. Putti, M.; Simonet, M.; Solberg, R.; Peters, G. W., Electrospinning poly (ϵ -caprolactone) under controlled environmental conditions: Influence on fibre morphology and orientation. *Polymer* **2015**, *63*, 189-195.

101. Huang, Z.-M.; Zhang, Y.-Z.; Kotaki, M.; Ramakrishna, S., A review on polymer nanofibres by electrospinning and their applications in nanocomposites. *Compos. Sci. Technol.* **2003**, *63* (15), 2223-2253.

102. Kim, G.-M.; Le, K. H. T.; Giannitelli, S. M.; Lee, Y. J.; Rainer, A.; Trombetta, M., Electrospinning of PCL/PVP blends for tissue engineering scaffolds. *J. Mater. Sci. Mater. Med.* **2013**, *24* (6), 1425-1442.

103. Wang, B.; Wang, Y.; Yin, T.; Yu, Q., Applications of electrospinning technique in drug delivery. *Chem. Eng. Commun.* **2010**, *197* (10), 1315-1338.

104. Agarwal, S.; Wendorff, J. H.; Greiner, A., Use of electrospinning technique for biomedical applications. *Polymer* **2008**, *49* (26), 5603-5621.

105. Vimal, S. K.; Ahamad, N.; Katti, D. S., A simple method for fabrication of electrospun fibres with controlled degree of alignment having potential for nerve regeneration applications. *Mater. Sci. Eng. C* **2016**, *63*, 616-627.

106. Cooper, A.; Bhattarai, N.; Zhang, M., Fabrication and cellular compatibility of aligned chitosan–PCL fibres for nerve tissue regeneration. *Carbohydr. Polym.* **2011**, *85* (1), 149-156.

107. Xie, J.; Liu, W.; MacEwan, M. R.; Bridgman, P. C.; Xia, Y., Neurite outgrowth on electrospun nanofibres with uniaxial alignment: the effects of fibre density, surface coating, and supporting substrate. *ACS nano* **2014**, *8* (2), 1878-1885.

108. Kenawy, E.-R.; Bowlin, G. L.; Mansfield, K.; Layman, J.; Simpson, D. G.;

Sanders, E. H.; Wnek, G. E., Release of tetracycline hydrochloride from electrospun poly (ethylene-co-vinylacetate), poly (lactic acid), and a blend. *J. Control. Release* **2002**, *81* (1-2), 57-64.

109. Jiang, H.; Hu, Y.; Li, Y.; Zhao, P.; Zhu, K.; Chen, W., A facile technique to prepare biodegradable coaxial electrospun nanofibres for controlled release of bioactive agents. *J. Control Release*. **2005**, *108* (2-3), 237-243.

110. Loscertales, I. G.; Barrero, A.; Guerrero, I.; Cortijo, R.; Marquez, M.; Ganan-Calvo, A., Micro/nano encapsulation via electrified coaxial liquid jets. *Science* **2002**, *295* (5560), 1695-1698.

111. Yang, C.; Yu, D.-G.; Pan, D.; Liu, X.-K.; Wang, X.; Bligh, S. A.; Williams, G. R., Electrospun pH-sensitive core-shell polymer nanocomposites fabricated using a tri-axial process. *Acta Biomater*. **2016**, *35*, 77-86.

112. Liao, I.-C.; Leong, K. W., Efficacy of engineered FVIII-producing skeletal muscle enhanced by growth factor-releasing co-axial electrospun fibres. *Biomaterials* **2011**, *32* (6), 1669-1677.

113. Aravindan, V.; Sundaramurthy, J.; Kumar, P. S.; Lee, Y.-S.; Ramakrishna, S.; Madhavi, S., Electrospun nanofibres: A prospective electro-active material for constructing high performance Li-ion batteries. *Chem. Comm.* **2015**, *51* (12), 2225-2234.

114. Fujihara, K.; Kotaki, M.; Ramakrishna, S., Guided bone regeneration membrane made of polycaprolactone/calcium carbonate composite nano-fibres. *Biomaterials* **2005**, *26* (19), 4139-4147.

115. Acatay, K.; Simsek, E.; Ow-Yang, C.; Menciloglu, Y. Z., Tunable, superhydrophobically stable polymeric surfaces by electrospinning. *Angew. Chem. Int. Ed.* **2004**, *43* (39), 5210-5213.

116. Xu, J.; Liu, C.; Hsu, P.-C.; Liu, K.; Zhang, R.; Liu, Y.; Cui, Y., Roll-to-roll transfer of electrospun nanofibre film for high-efficiency transparent air filter. *Nano Lett.* **2016**, *16* (2), 1270-1275.
117. Shenoy, S. L.; Bates, W. D.; Frisch, H. L.; Wnek, G. E., Role of chain entanglements on fibre formation during electrospinning of polymer solutions: good solvent, non-specific polymer–polymer interaction limit. *Polymer* **2005**, *46* (10), 3372-3384.
118. Wang, X.; Pellerin, C.; Bazuin, C. G., Enhancing the electrospinnability of low molecular weight polymers using small effective cross-linkers. *Macromolecules* **2016**, *49* (3), 891-899.
119. Kastelic, J.; Galeski, A.; Baer, E., The multicomposite structure of tendon. *Connect. Tissue Res.* **1978**, *6* (1), 11-23.
120. Riley, G.; Harrall, R.; Constant, C.; Chard, M.; Cawston, T.; Hazleman, B., Tendon degeneration and chronic shoulder pain: changes in the collagen composition of the human rotator cuff tendons in rotator cuff tendinitis. *Ann. Rheum. Dis.* **1994**, *53* (6), 359-366.
121. Franchi, M.; Trirè, A.; Quaranta, M.; Orsini, E.; Ottani, V., Collagen structure of tendon relates to function. *Sci. World J.* **2007**, *7*, 404-420.
122. Kadler, K. E.; Holmes, D. F.; Trotter, J. A.; Chapman, J. A., Collagen fibril formation. *Biochem. J.* **1996**, *316* (1), 1-11.
123. Kannus, P., Structure of the tendon connective tissue. *Scand. J. Med. Sci. Sports* **2000**, *10* (6), 312-320.
124. Viidik, A.; Ekholm, R., Light and electron microscopic studies of collagen fibres under strain. *Z. Anat. Entwicklungsgesch* **1968**, *127* (2), 154-164.
125. Wilmink, J.; Wilson, A.; Goodship, A., Functional significance of the

morphology and micromechanics of collagen fibres in relation to partial rupture of the superficial digital flexor tendon in racehorses. *Res. Vet. Sci.* **1992**, *53* (3), 354-359.

126. Mosler, E.; Folkhard, W.; Knörzer, E.; Nemetschek-Gansler, H.; Nemetschek, T.; Koch, M., Stress-induced molecular rearrangement in tendon collagen. *J. Mol. Biol.* **1985**, *182* (4), 589-596.

127. Cheng, V. W.; Screen, H. R., The micro-structural strain response of tendon. *J. Mater. Sci.* **2007**, *42* (21), 8957-8965.

128. Screen, H.; Lee, D.; Bader, D.; Shelton, J., Development of a technique to determine strains in tendons using the cell nuclei. *Biorheology* **2003**, *40* (1, 2, 3), 361-368.

129. O'brien, M., Structure and metabolism of tendons. *Scand. J. Med. Sci. Sports* **1997**, *7* (2), 55-61.

130. Manske, P. R., Flexor tendon healing. *J. Hand Surg. Br.* **1988**, *13* (3), 237-245.

131. P.R. Manske, M. D., FLEXOR TENDON HEALING. *J. Hand Surg.-Br. Eur. Vol.* **1988**, *13B* (3), 9.

132. Hyman, J.; Rodeo, S., Injury and repair of tendons and ligaments. *Phys. Med. Rehabil. Clin. N Am.* **2000**, *11* (2), 267-288.

133. Lin, T. W.; Cardenas, L.; Soslowsky, L. J., Biomechanics of tendon injury and repair. *J. Biomech.* **2004**, *37* (6), 865-877.

134. Smith, R.; McIlwraith, W.; Schweitzer, R.; Kadler, K.; Cook, J.; Caterson, B.; Dakin, S.; Heinegård, D.; Screen, H.; Stover, S., Advances in the understanding of tendinopathies: A report on the Second Havemeyer Workshop on equine tendon disease. *Equine. Vet. J.* **2014**, *46* (1), 4.

135. Peffers, M. J.; Thorpe, C. T.; Collins, J. A.; Eong, R.; Wei, T. K.; Screen, H. R.; Clegg, P. D., Proteomic analysis reveals age-related changes in tendon matrix

composition, with age-and injury-specific matrix fragmentation. *J. Biol. Chem.* **2014**, *289* (37), 25867-25878.

136. Longo, U. G.; Franceschi, F.; Ruzzini, L.; Rabitti, C.; Morini, S.; Maffulli, N.; Denaro, V., Histopathology of the supraspinatus tendon in rotator cuff tears. *Am. J. Sports Med.* **2008**, *36* (3), 533-538.

137. Thorpe, C.; Birch, H.; Clegg, P.; Screen, H., The micro-structural response of tendon fascicles to applied strain is altered with ageing. *Osteoarthr. Cartil.* **2012**, *20*, S246-S247.

138. Longo, U. G.; Lamberti, A.; Maffulli, N.; Denaro, V., Tendon augmentation grafts: a systematic review. *Brit. Med. Bull.* **2010**, 165-188.

139. De Jong, J. P.; Nguyen, J. T.; Sonnema, A. J.; Nguyen, E. C.; Amadio, P. C.; Moran, S. L., The incidence of acute traumatic tendon injuries in the hand and wrist: a 10-year population-based study. *Clin. Orthop. Surg.* **2014**, *6* (2), 196-202.

140. Linderman, S. W.; Gelberman, R. H.; Thomopoulos, S.; Shen, H., Cell and biologic-based treatment of flexor tendon injuries. *Oper. Tech. Orthop.* **2016**, *26* (3), 206-215.

141. Dowling, B.; Dart, A.; Hodgson, D.; Smith, R., Superficial digital flexor tendonitis in the horse. *Equine. Vet. J.* **2000**, *32* (5), 369-378.

142. Yang, G.; Rothrauff, B. B.; Tuan, R. S., Tendon and ligament regeneration and repair: clinical relevance and developmental paradigm. *Birth Defects Res. C Embryo Today* **2013**, *99* (3), 203-222.

143. Gelberman, R. H.; Manske, P. R.; Berg, J. S. V.; Lesker, P. A.; Akeson, W. H., Flexor tendon repair in vitro: a comparative histologic study of the rabbit, chicken, dog, and monkey. *J. Orthop. Res.* **1984**, *2* (1), 39-48.

144. Gelberman, R. H.; Vandeberg, J. S.; Manske, P. R.; Akeson, W. H., The early

stages of flexor tendon healing: a morphologic study of the first fourteen days. *J. Hand Surg. Am.* **1985**, *10* (6), 776-784.

145. Lundborg, G., Experimental flexor tendon healing without adhesion formation—a new concept of tendon nutrition and intrinsic healing mechanisms: a preliminary report. *Hand* **1976**, *8* (3), 235-238.

146. Fujita, M.; Hukuda, S.; Doida, Y., Experimental study of intrinsic healing of the flexor tendon: collagen synthesis of the cultured flexor tendon cells of the canine. *Nihon Seikeigeka Gakkai Zasshi* **1992**, *66* (4), 326-333.

147. Beredjiklian, P. K., Biologic aspects of flexor tendon laceration and repair. *J. Bone Joint Surg.* **2003**, *85* (3), 539-550.

148. Garner, W.; McDonald, J.; Koo, M.; Kuhn 3rd, C.; Weeks, P., Identification of the collagen-producing cells in healing flexor tendons. *Plast. Reconstr. Surg.* **1989**, *83* (5), 875-879.

149. Fenwick, S. A.; Hazleman, B. L.; Riley, G. P., The vasculature and its role in the damaged and healing tendon. *Arthritis. Res.* **2002**, *4* (4), 252-260.

150. Thorpe, C. T.; Birch, H. L.; Clegg, P. D.; Screen, H. R., The role of the non-collagenous matrix in tendon function. *Int. J. Exp Pathol.* **2013**, *94* (4), 248-259.

151. Bunnell, S., Contractures of the hand from infections and injuries. *J. Bone Joint Surg.* **1932**, *14* (1), 27-46.

152. Garlock, J. H., Repair of wounds of the flexor tendons of the hand. *Ann. Surg.* **1926**, *83* (1), 111-123.

153. Voleti, P. B.; Buckley, M. R.; Soslowsky, L. J., Tendon healing: repair and regeneration. *Annu. Rev. Biomed. Eng.* **2012**, *14*, 47-71.

154. Schnüriger, B.; Barmparas, G.; Branco, B. C.; Lustenberger, T.; Inaba, K.; Demetriades, D., Prevention of postoperative peritoneal adhesions: a review of the

literature. *Am. J. Surg.* **2011**, *201* (1), 111-121.

155. Kara, A.; Celik, H.; Seker, A.; Uysal, M. A.; Uzun, M.; Malkoc, M., Granuloma formation secondary to Achilles tendon repair with nonabsorbable suture. *Int. J. Surg. Case. Rep.* **2014**, *5* (10), 720-722.

156. Rawson, S.; Cartmell, S.; Wong, J., Suture techniques for tendon repair; a comparative review. *Muscles. Ligaments. Tendons. J.* **2013**, *3* (3), 220-229.

157. Savage, R., In vitro studies of a new method of flexor tendon repair. *J. Hand Surg. Eur. Vol.* **1985**, *10* (2), 135-141.

158. Rawson, S. D.; Margetts, L.; Wong, J. K.; Cartmell, S. H., Sutured tendon repair; a multi-scale finite element model. *Biomech. Model. Mechanobiol.* **2015**, *14* (1), 123-133.

159. Zhao, C.; Amadio, P. C.; Momose, T.; Couvreur, P.; Zobitz, M. E.; An, K.-N., The effect of suture technique on adhesion formation after flexor tendon repair for partial lacerations in a canine model. *J. Trauma Acute Care Surg.* **2001**, *51* (5), 917-921.

160. Khanna, A.; Gougoulas, N.; Maffulli, N., Modalities in prevention of flexor tendon adhesion in the hand: what have we achieved so far? *Acta Orthop. Belg.* **2009**, *75* (4), 433-445.

161. Strick, M. J.; Filan, S. L.; Hile, M.; McKenzie, C.; Walsh, W. R.; Tonkin, M. A., Adhesion formation after flexor tendon repair: a histologic and biomechanical comparison of 2-and 4-strand repairs in a chicken model. *J. Hand Surg.* **2004**, *29* (1), 15-21.

162. Shi, B.; Ding, J.; Wei, J.; Fu, C.; Zhuang, X.; Chen, X., Drug-incorporated electrospun fibres efficiently prevent postoperative adhesion. *Curr. Pharm. Des.* **2015**, *21* (15), 1960-1966.

163. Andres, B. M.; Murrell, G. A., Treatment of tendinopathy: what works, what does not, and what is on the horizon. *Clin. Orthop. Relat. Res.* **2008**, *466* (7), 1539.
164. Chen, J.; Yang, L.; Guo, L.; Duan, X., Sodium hyaluronate as a drug-release system for VEGF 165 improves graft revascularization in anterior cruciate ligament reconstruction in a rabbit model. *Exp. Ther. Med.* **2012**, *4* (3), 430-434.
165. Thomopoulos, S.; Das, R.; Silva, M. J.; Sakiyama-Elbert, S.; Harwood, F. L.; Zampiakos, E.; Kim, H. M.; Amiel, D.; Gelberman, R. H., Enhanced flexor tendon healing through controlled delivery of PDGF-BB. *J. Orthopaed Res.* **2009**, *27* (9), 1209-1215.
166. Sahoo, S.; Toh, S. L.; Goh, J. C., A bFGF-releasing silk/PLGA-based biohybrid scaffold for ligament/tendon tissue engineering using mesenchymal progenitor cells. *Biomaterials.* **2010**, *31* (11), 2990-2998.
167. Pascher, A.; Steinert, A. F.; Palmer, G. D.; Betz, O.; Gouze, J.-N.; Gouze, E.; Pilapil, C.; Ghivizzani, S. C.; Evans, C. H.; Murray, M. M., Enhanced repair of the anterior cruciate ligament by in situ gene transfer: evaluation in an in vitro model. *Mol. Ther.* **2004**, *10* (2), 327-336.
168. Fukui, N.; Tashiro, T.; Hiraoka, H.; Oda, H.; Nakamura, K., Adhesion formation can be reduced by the suppression of transforming growth factor- β 1 activity. *J. Orthop. Res.* **2000**, *18* (2), 212-219.
169. Magnussen, R. A.; Flanigan, D. C.; Pedroza, A. D.; Heinlein, K. A.; Kaeding, C. C., Platelet rich plasma use in allograft ACL reconstructions: two-year clinical results of a MOON cohort study. *The Knee* **2013**, *20* (4), 277-280.
170. Schepull, T.; Kvist, J.; Norrman, H.; Trinks, M.; Berlin, G.; Aspenberg, P., Autologous platelets have no effect on the healing of human Achilles tendon ruptures a randomized single-blind study. *Am. J. Sports Med.* **2011**, *38-47* (1), 38.

171. Liu, Y.; Skardal, A.; Shu, X. Z.; Prestwich, G. D., Prevention of peritendinous adhesions using a hyaluronan-derived hydrogel film following partial-thickness flexor tendon injury. *J. Orthop. Res.* **2008**, *26* (4), 562-569.
172. Temiz, A.; Ozturk, C.; Bakunov, A.; Kara, K.; Kaleli, T., A new material for prevention of peritendinous fibrotic adhesions after tendon repair: oxidised regenerated cellulose (Interceed), an absorbable adhesion barrier. *Int. Orthop.* **2008**, *32* (3), 389-394.
173. Akpan, U. M.; Taylor, B.; Odusanya, S.; Freeman, J.; Soboyejo, W. In *Studies on sandwiched electrospun scaffold of isomers of poly (lactic acid)(PLA) used in tissue engineering*, Electronics, Computer and Computation (ICECCO), 2014 11th International Conference on, IEEE: 2014; pp 1-4.
174. Boland, E. D.; Wnek, G. E.; Simpson, D. G.; Pawlowski, K. J.; Bowlin, G. L., Tailoring tissue engineering scaffolds using electrostatic processing techniques: a study of poly (glycolic acid) electrospinning. *J. Macromol. Sci., Pure Appl. Chem.* **2001**, *38* (12), 1231-1243.
175. Williams, J. M.; Adewunmi, A.; Schek, R. M.; Flanagan, C. L.; Krebsbach, P. H.; Feinberg, S. E.; Hollister, S. J.; Das, S., Bone tissue engineering using polycaprolactone scaffolds fabricated via selective laser sintering. *Biomaterials* **2005**, *26* (23), 4817-4827.
176. Zhu, A.; Chen, R.; Chan-Park, M. B., Patterning of a Random Copolymer of Poly [lactide-co-glycotide-co-(ϵ -caprolactone)] by UV Embossing for Tissue Engineering. *Macromol. Biosci.* **2006**, *6* (1), 51-57.
177. Lou, C.-W.; Yao, C.-H.; Chen, Y.-S.; Hsieh, T.-C.; Lin, J.-H.; Hsing, W.-H., Manufacturing and properties of PLA absorbable surgical suture. *Text. Res. J.* **2008**, *78* (11), 958-965.

178. Eppley, B. L.; Morales, L.; Wood, R.; Pensler, J.; Goldstein, J.; Havlik, R. J.; Habal, M.; Losken, A.; Williams, J. K.; Burstein, F., Resorbable PLLA-PGA plate and screw fixation in pediatric craniofacial surgery: clinical experience in 1883 patients. *Plast. Reconstr. Surg.* **2004**, *114* (4), 850-856.
179. Shor, L.; Güçeri, S.; Wen, X.; Gandhi, M.; Sun, W., Fabrication of three-dimensional polycaprolactone/hydroxyapatite tissue scaffolds and osteoblast-scaffold interactions in vitro. *Biomaterials.* **2007**, *28* (35), 5291-5297.
180. Babiuch, K.; Becer, C. R.; Gottschaldt, M.; Delaney, J. T.; Weisser, J.; Beer, B.; Wyrwa, R.; Schnabelrauch, M.; Schubert, U. S., Adhesion of Preosteoblasts and Fibroblasts onto Poly (pentafluorostyrene)-Based Glycopolymers and their Biocompatibility. *Macromol. Biosci.* **2011**, *11* (4), 535-548.
181. Meier Bürgisser, G.; Calcagni, M.; Müller, A.; Bonavoglia, E.; Fessel, G.; Snedeker, J. G.; Giovanoli, P.; Buschmann, J., Prevention of Peritendinous Adhesions Using an Electrospun DegraPol Polymer Tube: A Histological, Ultrasonographic, and Biomechanical Study in Rabbits. *BioMed Res. Int.* **2014**, *2014*, 1-13.
182. Chen, S.-H.; Chen, C.-H.; Fong, Y. T.; Chen, J.-P., Prevention of peritendinous adhesions with electrospun chitosan-grafted polycaprolactone nanofibrous membranes. *Acta. Biomater.* **2014**, *10* (12), 4971-4982.
183. Liu, S.; Hu, C.; Li, F.; Li, X.-j.; Cui, W.; Fan, C., Prevention of peritendinous adhesions with electrospun ibuprofen-loaded poly (L-lactic acid)-polyethylene glycol fibrous membranes. *Tissue. Eng. Pt. A.* **2012**, *19* (3-4), 529-537.
184. Liu, S.; Hu, C.; Li, F.; Li, X.-j.; Cui, W.; Fan, C., Prevention of peritendinous adhesions with electrospun ibuprofen-loaded poly (L-lactic acid)-polyethylene glycol fibrous membranes. *Tissue Eng. Part A* **2012**, *19* (3-4), 529-537.
185. Naik, N.; Caves, J.; Chaikof, E. L.; Allen, M. G., Generation of spatially

aligned collagen fibre networks through microtransfer molding. *Adv. Healthc. Mater.* **2014**, *3* (3), 367-374.

186. Jean, A.; Engelmayer, G. C., Anisotropic collagen fibrillogenesis within microfabricated scaffolds: implications for biomimetic tissue engineering. *Adv. Healthc. Mater.* **2012**, *1* (1), 112-116.

187. Lee, S. J.; Liu, J.; Oh, S. H.; Soker, S.; Atala, A.; Yoo, J. J., Development of a composite vascular scaffolding system that withstands physiological vascular conditions. *Biomaterials* **2008**, *29* (19), 2891-2898.

188. Ahn, S.; Chantre, C. O.; Gannon, A. R.; Lind, J. U.; Campbell, P. H.; Grevesse, T.; O'connor, B. B.; Parker, K. K., Soy Protein/Cellulose Nanofibre Scaffolds Mimicking Skin Extracellular Matrix for Enhanced Wound Healing. *Adv. Healthc. Mater.* **2018**, *7* (9), 1701175-1701188.

189. Hossain, K. M. Z.; Hasan, M. S.; Boyd, D.; Rudd, C. D.; Ahmed, I.; Thielemans, W., Effect of cellulose nanowhiskers on surface morphology, mechanical properties, and cell adhesion of melt-drawn polylactic acid fibres. *Biomacromolecules* **2014**, *15* (4), 1498-1506.

190. Zhang, C.; Yuan, H.; Liu, H.; Chen, X.; Lu, P.; Zhu, T.; Yang, L.; Yin, Z.; Heng, B. C.; Zhang, Y., Well-aligned chitosan-based ultrafine fibres committed teno-lineage differentiation of human induced pluripotent stem cells for Achilles tendon regeneration. *Biomaterials* **2015**, *53*, 716-730.

191. Nair, L. S.; Laurencin, C. T., Biodegradable polymers as biomaterials. *Prog. Polym. Sci* **2007**, *32* (8-9), 762-798.

192. Imanish, Y.; Ito, Y.; Liu, L.-S.; Kajihara, M., Design and synthesis of biocompatible polymeric materials. *J. Macromol. Sci. C* **1988**, *25* (5-7), 555-570.

193. Hořojší, V.; Chaloupecka, O., Studies on lectins: XLIII. Isolation and

characterization of the lectin from restharrow boots (*Ononis hircina* Jacq.). *Biochim. Biophys. Acta* **1978**, 539 (3), 287-293.

194. Xue, J.; He, M.; Liu, H.; Niu, Y.; Crawford, A.; Coates, P. D.; Chen, D.; Shi, R.; Zhang, L., Drug loaded homogeneous electrospun PCL/gelatin hybrid nanofibre structures for anti-infective tissue regeneration membranes. *Biomaterials* **2014**, 35 (34), 9395-9405.

195. Heydarkhan-Hagvall, S.; Schenke-Layland, K.; Dhanasopon, A. P.; Rofail, F.; Smith, H.; Wu, B. M.; Shemin, R.; Beygui, R. E.; MacLellan, W. R., Three-dimensional electrospun ECM-based hybrid scaffolds for cardiovascular tissue engineering. *Biomaterials* **2008**, 29 (19), 2907-2914.

196. Duling, R. R.; Dupaix, R. B.; Katsube, N.; Lannutti, J., Mechanical characterization of electrospun polycaprolactone (PCL): a potential scaffold for tissue engineering. *J. Biomech. Eng.* **2008**, 130 (1), 011006-011019.

197. Lam, C. X.; Hutmacher, D. W.; Schantz, J. T.; Woodruff, M. A.; Teoh, S. H., Evaluation of polycaprolactone scaffold degradation for 6 months in vitro and in vivo. *J. Biomed. Mater. Res. A* **2009**, 90 (3), 906-919.

198. Simon, E., Ueber den flüssigen Storax (*Styrax liquidus*). *Ann. Pharm.* **1839**, 31 (3), 265-277.

199. Ruzette, A.-V.; Leibler, L., Block copolymers in tomorrow's plastics. *Nat. Mater.* **2005**, 4 (1), 19-31.

200. Lu, H.; Lu, Q.; Chen, W.; Xu, H.; Yin, J., Cell culturing on nanogrooved polystyrene petri dish induced by ultraviolet laser irradiation. *Mater. Lett.* **2004**, 58 (1-2), 29-32.

201. Chen, Y.; Gao, Q.; Wan, H.; Yi, J.; Wei, Y.; Liu, P., Surface modification and biocompatible improvement of polystyrene film by Ar, O₂ and Ar⁺ O₂ plasma. *Appl.*

Surf. Sci. **2013**, *265*, 452-457.

202. Maul, J.; Frushour, B. G.; Kontoff, J. R.; Eichenauer, H.; Ott, K. H., Polystyrene and styrene copolymers. *Ullmann's encyclopedia of industrial chemistry* **2000**.

203. Wang, L.; Yan, L.; Zhao, P.; Torimoto, Y.; Sadakata, M.; Li, Q., Surface modification of polystyrene with atomic oxygen radical anions-dissolved solution. *Appl. Surf. Sci.* **2008**, *254* (13), 4191-4200.

204. van Kooten, T. G.; Spijker, H. T.; Busscher, H. J., Plasma-treated polystyrene surfaces: model surfaces for studying cell–biomaterial interactions. *Biomaterials* **2004**, *25* (10), 1735-1747.

205. Teare, D.; Emmison, N.; Ton-That, C.; Bradley, R., Cellular attachment to ultraviolet ozone modified polystyrene surfaces. *Langmuir* **2000**, *16* (6), 2818-2824.

206. Murakami, T. N.; Fukushima, Y.; Hirano, Y.; Tokuoka, Y.; Takahashi, M.; Kawashima, N., Surface modification of polystyrene and poly (methyl methacrylate) by active oxygen treatment. *Colloids Surf. B: Biointerfaces* **2003**, *29* (2-3), 171-179.

207. Onyiriuka, E.; Hersh, L.; Hertl, W., Surface modification of polystyrene by gamma-radiation. *Appl. Spectrosc.* **1990**, *44* (5), 808-811.

208. Ladmiral, V.; Melia, E.; Haddleton, D. M., Synthetic glycopolymers: an overview. *Eur. Polym. J.* **2004**, *40* (3), 431-449.

209. Yilmaz, G.; Uzunova, V.; Napier, R. M.; Becer, C. R., Single-Chain Glycopolymer Folding via Host-Guest Interactions and Its Unprecedented Effect on DC-SIGN Binding. *Biomacromolecules* **2018**, 3040–3047.

210. Spain, S. G.; Cameron, N. R., A spoonful of sugar: the application of glycopolymers in therapeutics. *Polym. Chem.* **2011**, *2* (1), 60-68.

211. Yilmaz, G.; Becer, C. R., Precision glycopolymers and their interactions with

- lectins. *Eur. Polym. J.* **2013**, *49* (10), 3046-3051.
212. Geng, J.; Mantovani, G.; Tao, L.; Nicolas, J.; Chen, G.; Wallis, R.; Mitchell, D. A.; Johnson, B. R.; Evans, S. D.; Haddleton, D. M., Site-directed conjugation of “clicked” glycopolymers to form glycoprotein mimics: binding to mammalian lectin and induction of immunological function. *J. Am. Chem. Soc.* **2007**, *129* (49), 15156-15163.
213. Becer, C. R.; Gibson, M. I.; Geng, J.; Ilyas, R.; Wallis, R.; Mitchell, D. A.; Haddleton, D. M., High-affinity glycopolymer binding to human DC-SIGN and disruption of DC-SIGN interactions with HIV envelope glycoprotein. *J. Am. Chem. Soc.* **2010**, *132* (43), 15130-15132.
214. Meng, Q.; Haque, A.; Hexig, B.; Akaike, T., The differentiation and isolation of mouse embryonic stem cells toward hepatocytes using galactose-carrying substrata. *Biomaterials* **2012**, *33* (5), 1414-1427.
215. Zhao, C.; Shi, Q.; Hou, J.; Xin, Z.; Jin, J.; Li, C.; Wong, S.-C.; Yin, J., Capturing red blood cells from the blood by lectin recognition on a glycopolymer-patterned surface. *J. Mater. Chem. B* **2016**, *4* (23), 4130-4137.
216. Quan, J.; Liu, Z.; Branford-White, C.; Nie, H.; Zhu, L., Fabrication of glycopolymer/MWCNTs composite nanofibres and its enzyme immobilization applications. *Colloids Surf. B: Biointerfaces* **2014**, *121*, 417-424.
217. Zelensky, A. N.; Gready, J. E., The C-type lectin-like domain superfamily. *FEBS J.* **2005**, *272* (24), 6179-6217.
218. Lundquist, J. J.; Toone, E. J., The cluster glycoside effect. *Chem. Rev.* **2002**, *102* (2), 555-578.
219. Wong, E. H.; Khin, M. M.; Ravikumar, V.; Si, Z.; Rice, S. A.; Chan-Park, M. B., Modulating antimicrobial activity and mammalian cell biocompatibility with

- glucosamine-functionalized star polymers. *Biomacromolecules* **2016**, *17* (3), 1170-1178.
220. Habibi, Y.; Goffin, A.-L.; Schiltz, N.; Duquesne, E.; Dubois, P.; Dufresne, A., Bionanocomposites based on poly (ϵ -caprolactone)-grafted cellulose nanocrystals by ring-opening polymerization. *J. Mater. Chem.* **2008**, *18* (41), 5002-5010.
221. Perrier, S.; Armes, S. P.; Wang, X.; Malet, F.; Haddleton, D. M., Copper (I)-mediated radical polymerization of methacrylates in aqueous solution. *J. Polym. Sci. A Polym. Chem.* **2001**, *39* (10), 1696-1707.
222. Aksakal, R.; Resmini, M.; Becer, C., Pentablock star shaped polymers in less than 90 minutes via aqueous SET-LRP. *Polym. Chem.* **2016**, *7* (1), 171-175.
223. Wei, H.; Cheng, S.-X.; Zhang, X.-Z.; Zhuo, R.-X., Thermo-sensitive polymeric micelles based on poly (N-isopropylacrylamide) as drug carriers. *Prog. Polym. Sci.* **2009**, *34* (9), 893-910.
224. Chmielarz, P.; Krys, P.; Park, S.; Matyjaszewski, K., PEO-b-PNIPAM copolymers via SARA ATRP and eATRP in aqueous media. *Polymer* **2015**, *71*, 143-147.
225. Chen, J.; Liu, M.; Chen, C.; Gong, H.; Gao, C., Synthesis and characterization of silica nanoparticles with well-defined thermoresponsive PNIPAM via a combination of RAFT and click chemistry. *ACS Appl. Mater. Interfaces* **2011**, *3* (8), 3215-3223.
226. Alsubaie, F.; Anastasaki, A.; Wilson, P.; Haddleton, D. M., Sequence-controlled multi-block copolymerization of acrylamides via aqueous SET-LRP at 0 C. *Polym. Chem.* **2014**, *6* (3), 406-417.
227. Bose, S.; Vahabzadeh, S.; Bandyopadhyay, A., Bone tissue engineering using 3D printing. *Mater. Today* **2013**, *16* (12), 496-504.

228. Gladman, A. S.; Matsumoto, E. A.; Nuzzo, R. G.; Mahadevan, L.; Lewis, J. A., Biomimetic 4D printing. *Nat. Mater.* **2016**, *15* (4), 413-418.
229. Jin, H.; Ding, Y.-H.; Wang, M.; Song, Y.; Liao, Z.; Newcomb, C. J.; Wu, X.; Tang, X.-Q.; Li, Z.; Lin, Y., Designable and dynamic single-walled stiff nanotubes assembled from sequence-defined peptoids. *Nat. Commun.* **2018**, *9* (1), 270-281.
230. Su, N.; Gao, P.-L.; Wang, K.; Wang, J.-Y.; Zhong, Y.; Luo, Y., Fibrous scaffolds potentiate the paracrine function of mesenchymal stem cells: A new dimension in cell-material interaction. *Biomaterials* **2017**, *141*, 74-85.
231. Xu, C.; Inai, R.; Kotaki, M.; Ramakrishna, S., Aligned biodegradable nanofibrous structure: a potential scaffold for blood vessel engineering. *Biomaterials* **2004**, *25* (5), 877-886.
232. Yin, Z.; Chen, X.; Chen, J. L.; Shen, W. L.; Nguyen, T. M. H.; Gao, L.; Ouyang, H. W., The regulation of tendon stem cell differentiation by the alignment of nanofibres. *Biomaterials* **2010**, *31* (8), 2163-2175.
233. Xie, J.; Li, X.; Lipner, J.; Manning, C. N.; Schwartz, A. G.; Thomopoulos, S.; Xia, Y., "Aligned-to-random" nanofibre scaffolds for mimicking the structure of the tendon-to-bone insertion site. *Nanoscale* **2010**, *2* (6), 923-926.
234. Bordes, C.; Fréville, V.; Ruffin, E.; Marote, P.; Gauvrit, J.; Briançon, S.; Lantéri, P., Determination of poly (ϵ -caprolactone) solubility parameters: Application to solvent substitution in a microencapsulation process. *Int. J. Pharm* **2010**, *383* (1-2), 236-243.
235. Godinho, M. S.; Thorpe, C. T.; Greenwald, S. E.; Screen, H. R., Elastin is Localised to the Interfascicular Matrix of Energy Storing Tendons and Becomes Increasingly Disorganised With Ageing. *Sci. Rep.* **2017**, *7* (1), 9713-9724.
236. Schindelin, J.; Arganda-Carreras, I.; Frise, E.; Kaynig, V.; Longair, M.;

Pietzsch, T.; Preibisch, S.; Rueden, C.; Saalfeld, S.; Schmid, B., Fiji: an open-source platform for biological-image analysis. *Nat. Methods* **2012**, *9* (7), 676-682.

237. Liu, Z.-Q., Scale space approach to directional analysis of images. *Appl. Opt.* **1991**, *30* (11), 1369-1373.

238. Si, Y.; Yu, J.; Tang, X.; Ge, J.; Ding, B., Ultralight nanofibre-assembled cellular aerogels with superelasticity and multifunctionality. *Nat. Commun.* **2014**, *5*, 5802-5811.

239. Liang, H. W.; Guan, Q. F.; Chen, L. F.; Zhu, Z.; Zhang, W. J.; Yu, S. H., Macroscopic-Scale Template Synthesis of Robust Carbonaceous Nanofibre Hydrogels and Aerogels and Their Applications. *Angew. Chem. Int. Ed.* **2012**, *51* (21), 5101-5105.

240. Bölgen, N.; Menciloğlu, Y. Z.; Acatay, K.; Vargel, I.; Pişkin, E., In vitro and in vivo degradation of non-woven materials made of poly (ϵ -caprolactone) nanofibres prepared by electrospinning under different conditions. *J. Biomater. Sci. Polym. Ed.* **2005**, *16* (12), 1537-1555.

241. Megelski, S.; Stephens, J. S.; Chase, D. B.; Rabolt, J. F., Micro-and nanostructured surface morphology on electrospun polymer fibres. *Macromolecules* **2002**, *35* (22), 8456-8466.

242. Thompson, C.; Chase, G. G.; Yarin, A.; Reneker, D., Effects of parameters on nanofibre diameter determined from electrospinning model. *Polymer* **2007**, *48* (23), 6913-6922.

243. Lu, D. R.; Park, K., Effect of surface hydrophobicity on the conformational changes of adsorbed fibrinogen. *J. Colloid Interface Sci.* **1991**, *144* (1), 271-281.

244. Ku, S. H.; Ryu, J.; Hong, S. K.; Lee, H.; Park, C. B., General functionalization route for cell adhesion on non-wetting surfaces. *Biomaterials* **2010**, *31* (9), 2535-2541.

245. Baker, S. C.; Atkin, N.; Gunning, P. A.; Granville, N.; Wilson, K.; Wilson, D.;

Southgate, J., Characterisation of electrospun polystyrene scaffolds for three-dimensional in vitro biological studies. *Biomaterials* **2006**, *27* (16), 3136-3146.

246. Parry, A. L.; Clemson, N. A.; Ellis, J.; Bernhard, S. S.; Davis, B. G.; Cameron, N. R., 'Multicopy multivalent' glycopolymer-stabilized gold nanoparticles as potential synthetic cancer vaccines. *J. Am. Chem. Soc.* **2013**, *135* (25), 9362-9365.

247. Ahmed, M.; Narain, R., The effect of polymer architecture, composition, and molecular weight on the properties of glycopolymer-based non-viral gene delivery systems. *Biomaterials* **2011**, *32* (22), 5279-5290.

248. Schmaljohann, D., Thermo- and pH-responsive polymers in drug delivery. *Adv. Drug Deliv. Rev.* **2006**, *58* (15), 1655-1670.

249. Rezwan, K.; Chen, Q.; Blaker, J.; Boccaccini, A. R., Biodegradable and bioactive porous polymer/inorganic composite scaffolds for bone tissue engineering. *Biomaterials* **2006**, *27* (18), 3413-3431.

250. Pranantyo, D.; Xu, L. Q.; Hou, Z.; Kang, E.-T.; Chan-Park, M. B., Increasing bacterial affinity and cytocompatibility with four-arm star glycopolymers and antimicrobial α -polylysine. *Polym. Chem.* **2017**, *8* (21), 3364-3373.

251. Narayanaswamy, V. P.; Giatpaiboon, S. A.; Uhrig, J.; Orwin, P.; Wiesmann, W.; Baker, S. M.; Townsend, S. M., In Vitro activity of novel glycopolymer against clinical isolates of multidrug-resistant *Staphylococcus aureus*. *PloS one* **2018**, *13* (1), 0191522-0191538.

252. Patel, D.; Sharma, S.; Bryant, S. J.; Screen, H. R., Recapitulating the Micromechanical Behavior of Tension and Shear in a Biomimetic Hydrogel for Controlling Tenocyte Response. *Adv. Healthc. Mater.* **2016**, 1601095-1601102.

253. Konradi, R.; Acikgoz, C.; Textor, M., Polyoxazolines for nonfouling surface coatings—a direct comparison to the gold standard PEG. *Macromol. Rapid Commun.*

2012, 33 (19), 1663-1676.

254. Basuki, J. S.; Esser, L.; Duong, H. T.; Zhang, Q.; Wilson, P.; Whittaker, M. R.; Haddleton, D. M.; Boyer, C.; Davis, T. P., Magnetic nanoparticles with diblock glycopolymer shells give lectin concentration-dependent MRI signals and selective cell uptake. *Chem. Sci.* **2014**, 5 (2), 715-726.

255. Ahmed, M.; Narain, R., The effect of molecular weight, compositions and lectin type on the properties of hyperbranched glycopolymers as non-viral gene delivery systems. *Biomaterials* **2012**, 33 (15), 3990-4001.

256. Sato, T.; Shimizu, H.; Beppu, M.; Takagi, M., Effects on bone union and prevention of tendon adhesion by new porous anti-adhesive poly L-lactide-co-ε-caprolactone membrane in a rabbit model. *J. Hand Surg. Br.* **2013**, 18 (01), 1-10.

257. Zhao, X.; Jiang, S.; Liu, S.; Chen, S.; Lin, Z. Y. W.; Pan, G.; He, F.; Li, F.; Fan, C.; Cui, W., Optimization of intrinsic and extrinsic tendon healing through controllable water-soluble mitomycin-C release from electrospun fibres by mediating adhesion-related gene expression. *Biomaterials* **2015**, 61, 61-74.

258. Lu, D. R.; Park, K., Effect of surface hydrophobicity on the conformational changes of adsorbed fibrinogen. *J. Colloid Interface Sci.* **1991**, 144 (1), 271-281.

259. Li, W. J.; Laurencin, C. T.; Caterson, E. J.; Tuan, R. S.; Ko, F. K., Electrospun nanofibrous structure: a novel scaffold for tissue engineering. *J. Biomed. Mater. Res. Part B Appl. Biomater* **2002**, 60 (4), 613-621.

260. Liao, S.; Li, B.; Ma, Z.; Wei, H.; Chan, C.; Ramakrishna, S., Biomimetic electrospun nanofibres for tissue regeneration. *Biomed. Mater.* **2006**, 1 (3), R45-R55.

261. Xu, B.; Cook, W. D.; Zhu, C.; Chen, Q., Aligned core/shell electrospinning of poly (glycerol sebacate)/poly (l-lactic acid) with tuneable structural and mechanical properties. *Polym. Int.* **2016**, 65 (4), 423-429.

262. Chan, B.; Leong, K., Scaffolding in tissue engineering: general approaches and tissue-specific considerations. *Eur. Spine J.* **2008**, *17* (4), 467-479.
263. Johnson, G. A.; Tramaglini, D. M.; Levine, R. E.; Ohno, K.; Choi, N. Y.; L-Y Woo, S., Tensile and viscoelastic properties of human patellar tendon. *J. Orthop. Res.* **1994**, *12* (6), 796-803.
264. Thorpe, C. T.; Udeze, C. P.; Birch, H. L.; Clegg, P. D.; Screen, H. R., Capacity for sliding between tendon fascicles decreases with ageing in injury prone equine tendons: a possible mechanism for age-related tendinopathy. *Eur. Cells Mater* **2013**, *25*, 48-60.
265. Thorpe, C. T.; Udeze, C. P.; Birch, H. L.; Clegg, P. D.; Screen, H. R., Specialization of tendon mechanical properties results from interfascicular differences. *J. Royal Soc. Interface* **2012**, rsif20120362.
266. Quan, S.; Kumar, P.; Narain, R., Cationic Galactose-Conjugated Copolymers for Epidermal Growth Factor (EGFR) Knockdown in Cervical Adenocarcinoma. *ACS Biomater. Sci. Eng.* **2016**, *2* (5), 853-859.
267. Zhao, G.; Zhang, X.; Lu, T. J.; Xu, F., Recent advances in electrospun nanofibrous scaffolds for cardiac tissue engineering. *Adv. Funct. Mater.* **2015**, *25* (36), 5726-5738.
268. Chew, S. Y.; Mi, R.; Hoke, A.; Leong, K. W., Aligned Protein-Polymer Composite Fibres Enhance Nerve Regeneration: A Potential Tissue-Engineering Platform. *Adv. Funct. Mater.* **2007**, *17* (8), 1288-1296.
269. Chen, C.-H.; Chen, S.-H.; Shalumon, K.; Chen, J.-P., Prevention of peritendinous adhesions with electrospun polyethylene glycol/polycaprolactone nanofibrous membranes. *Colloids Surf. B* **2015**, *133*, 221-230.
270. O'brien, M., Structure and metabolism of tendons. *Scand. J. Med. Sci. Sports*

1997, 7 (2), 55-61.

271. Li, M.; Mondrinos, M. J.; Gandhi, M. R.; Ko, F. K.; Weiss, A. S.; Lelkes, P. I., Electrospun protein fibres as matrices for tissue engineering. *Biomaterials* **2005**, 26 (30), 5999-6008.

272. Park, S.-H.; Kim, M. S.; Lee, B.; Park, J. H.; Lee, H. J.; Lee, N. K.; Jeon, N. L.; Suh, K.-Y., Creation of a Hybrid Scaffold with Dual Configuration of Aligned and Random Electrospun Fibres. *ACS Appl. Mater. Interfaces* **2016**, 8 (4), 2826-2832.

273. Chew, S. Y.; Mi, R.; Hoke, A.; Leong, K. W., The effect of the alignment of electrospun fibrous scaffolds on Schwann cell maturation. *Biomaterials* **2008**, 29 (6), 653-661.

274. Juneja, S. C., Cellular distribution and gene expression profile during flexor tendon graft repair: a novel tissue engineering approach. *J. Tissue Eng.* **2013**, 4, 2041731413492741.

275. Maroudas, A.; Stockwell, R.; Nachemson, A.; Urban, J., Factors involved in the nutrition of the human lumbar intervertebral disc: cellularity and diffusion of glucose in vitro. *J. Anat.* **1975**, 120 (Pt 1), 113-131.

276. Grafahrend, D.; Heffels, K.-H.; Beer, M. V.; Gasteier, P.; Möller, M.; Boehm, G.; Dalton, P. D.; Groll, J., Degradable polyester scaffolds with controlled surface chemistry combining minimal protein adsorption with specific bioactivation. *Nat. Mater.* **2011**, 10 (1), 67-73.

277. Yilmaz, G.; Becer, C. R., Glyconanoparticles and their interactions with lectins. *Polym. Chem.* **2015**, 6 (31), 5503-5514.

278. Lavilla, C.; Yilmaz, G.; Uzunova, V.; Napier, R.; Becer, C. R.; Heise, A., Block-Sequence-Specific Glycopolypeptides with Selective Lectin Binding Properties. *Biomacromolecules* **2017**, 18 (6), 1928-1936.

279. Pozzi, D.; Colapicchioni, V.; Caracciolo, G.; Piovesana, S.; Capriotti, A. L.; Palchetti, S.; De Grossi, S.; Riccioli, A.; Amenitsch, H.; Laganà, A., Effect of polyethyleneglycol (PEG) chain length on the bio–nano-interactions between PEGylated lipid nanoparticles and biological fluids: from nanostructure to uptake in cancer cells. *Nanoscale* **2014**, *6* (5), 2782-2792.
280. Becer, C. R., The glycopolymer code: synthesis of glycopolymers and multivalent carbohydrate–lectin interactions. *Macromol. Rapid Commun.* **2012**, *33* (9), 742-752.
281. Kim, S. E.; Heo, D. N.; Lee, J. B.; Kim, J. R.; Park, S. H.; Jeon, S. H.; Kwon, I. K., Electrospun gelatin/polyurethane blended nanofibres for wound healing. *Biomed. Mater.* **2009**, *4* (4), 044106-044118.
282. Wong, J. K.; Lui, Y. H.; Kapacee, Z.; Kadler, K. E.; Ferguson, M. W.; McGrouther, D. A., The cellular biology of flexor tendon adhesion formation: an old problem in a new paradigm. *Am. J. Pathol.* **2009**, *175* (5), 1938-1951.

Appendix

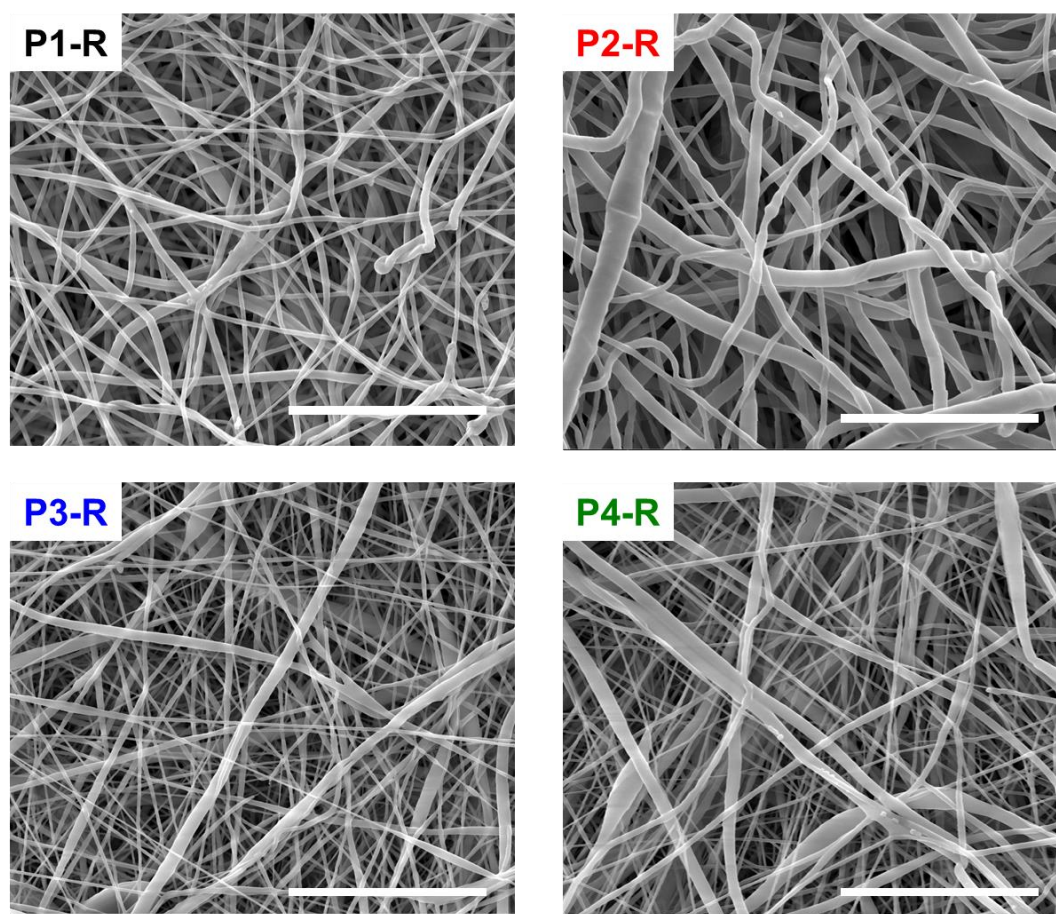


Figure S.1 SEM images of fibres after sterilization. Pictures shows the stable fibrous structure over sterilized treatment. Scale bar represents 10 μm in all images.